
Mixed-symmetry states in high-resolution electron and proton scattering: The cases of ^{92}Zr and ^{94}Mo

Gemischt-symmetrische Zustände in hochauflösender Elektronen- und Protonenstreuung am Beispiel von ^{92}Zr und ^{94}Mo

Project-Proposal von Christopher Walz

September 2010



TECHNISCHE
UNIVERSITÄT
DARMSTADT

Fachbereich Physik
Institut für Kernphysik
AG Pietralla

Mixed-symmetry states in high-resolution electron and proton scattering: The cases of ^{92}Zr and ^{94}Mo
Gemischt-symmetrische Zustände in hochauflösender Elektronen- und Protonenstreuung am Beispiel von ^{92}Zr
und ^{94}Mo

vorgelegtes Project-Proposal von Christopher Walz

1. Gutachten: Prof. Dr. Norbert Pietralla
2. Gutachten: Prof. Dr. Peter von Neumann-Cosel

Tag der Einreichung:

Abstract

In the framework of this master thesis data from proton and electron scattering experiments on the nuclei ^{92}Zr and ^{94}Mo were analyzed. The extracted cross sections and form factors were compared to predictions of the Quasi-Particle Phonon Model (QPM). Due to the different isospin sensitivity of both probes the proton as well as the neutron matrix elements of the QPM wave functions could be tested.

The central result of this work is the observation of a new experimental signature for a one-phonon quadrupole mixed-symmetric state. The new signature is based on a reduction of the matter transition radius of the mixed-symmetry state compared to all other 2^+ states. The matter transition radii of all quadrupole states up to 4 MeV in ^{94}Mo were obtained from the proton scattering cross sections. The matter transition radius of the quadrupole mixed-symmetry state is found to be - by far - the smallest. This property is directly connected to its isovector nature and can therefore be used to identify mixed-symmetry states independently of $B(M1)$ -values used so far. A similar analysis is performed for ^{92}Zr . The difference of the charge transition radii between the symmetric and the mixed-symmetric state is extracted from electron scattering data in ^{92}Zr . Both radii have a very similar size.

A simple model is developed to study the influence of the Giant Quadrupole Resonance on effective forces used in the Interacting Boson Model 2 and on the formation mechanism of mixed-symmetry states in general. Conclusions on the evolution of mixed-symmetry states are drawn for the Mo-chain using this simple model. The $M1$ -strength between the symmetric and mixed-symmetric quadrupole states is found to be inversely proportional to the square of the deformation parameter. This is the opposite to the behaviour known from the scissors mode.

Zusammenfassung

Im Rahmen dieser Masterarbeit wurden Daten von Proton- und Elektronenstreuexperimenten an ^{92}Zr und ^{94}Mo analysiert. Die gemessenen Wirkungsquerschnitte und Formfaktoren wurden mit Vorhersagen des Quasi-Particle Phonon Models (QPM) verglichen. Auf Grund der unterschiedlichen Sensitivität beider Proben in Bezug auf den Isospinfreiheitsgrad konnten sowohl die Protonen- als auch die Neutronenübergangsmatrixelemente der QPM-Wellenfunktionen zum Grundzustand getestet werden.

Das zentrale Ergebnis dieser Arbeit ist neue Signatur für die Identifikation eines gemischt-symmetrischen Zustandes. Dazu wurden die Massenübergangsradien aller 2^+ Zustände in ^{94}Mo bis 4 MeV untersucht. Der Massenübergangsradius des gemischt-symmetrischen Zustands ist mit Abstand am kleinsten. Diese Eigenschaft ist auf seinen isovektoriellen Charakter zurückzuführen und kann in Zukunft als Identifikationsmerkmal für einen gemischt-symmetrischen Zustand verwendet werden. Eine ähnliche Analyse wurde für ^{92}Zr vorgenommen. Der Unterschied der Übergangsladungsradien des symmetrischen und gemischt-symmetrischen Zustandes in ^{92}Zr wurde mit Hilfe von Elektronenstreuexperimenten untersucht. Beide Radien sind im Rahmen experimenteller Fehler gleich groß.

Im Rahmen dieser Arbeit wurde ein einfaches Modell entwickelt um den Einfluß der Quadrupol Riesenresonanz auf effektive Kräfte im Interacting Boson Model 2 zu untersuchen. Das Modell liefert zusätzlich ein einfaches Bild für den Formationsmechanismus von gemischt-symmetrischen Zuständen in Atomkernen. Des Weiteren wurden einige systematische Untersuchungen der Eigenschaften gemischt-symmetrischer Zustände vorgenommen. Die $B(M1)$ -Stärke zwischen dem symmetrischen und dem gemischt-symmetrischen Zustand fällt linear mit dem Quadrat des Deformationsparameters ab. Dies ist das gegenteilige Verhalten, welches von der Scherenmode bekannt ist.

Contents

1	Introduction	1
2	Theoretical descriptions	6
2.1	The Interacting Boson Model	6
2.1.1	The Interacting Boson Model 1	6
2.1.2	The Interacting Boson Model 2	8
2.2	The Quasiparticle Phonon Model	13
2.2.1	General formalism	13
2.2.2	Electromagnetic transition strengths and densities	18
3	The Experiment	20
3.1	Electron scattering at the S-DALINAC	20
3.1.1	The S-DALINAC	20
3.1.2	High-resolution electron scattering facility	21
3.2	Proton scattering at iThemba LABS	22
3.2.1	iThemba LABS	22
3.2.2	K600 spectrometer	22
4	Data analysis and results	24
4.1	Proton scattering	24
4.1.1	Data taking conditions	24
4.1.2	Determination of the cross sections and energy calibration	26
4.1.3	Error estimate	26
4.1.4	DWBA analysis	27
4.1.5	Proton scattering results for ^{92}Zr	28
4.1.6	Proton scattering results for ^{94}Mo	32
4.1.7	Comparison to QPM results	35
4.2	Electron scattering at ^{92}Zr	37
4.2.1	Data taking conditions	37
4.2.2	Determination of the cross sections	37
4.2.3	Error estimate	39
4.2.4	Form factor results	39
5	An alternative view on one-phonon quadrupole mixed-symmetry states	40
5.1	QPM results for ^{92}Zr	40
5.2	One-phonon mixed-symmetry states in electron and proton scattering	42
5.3	Effective forces in quadrupole collective models and the formation mechanism of mixed-symmetry states	48
5.4	The evolution of one-phonon quadrupole mixed-symmetry states	52
6	Summary and outlook	57
	References	57

List of Figures

1.1	Overview about the theoretical strategies to tackle the nuclear many-body problem	1
1.2	Section of the nuclear chart	3
1.3	Transition strength of the scissors mode in dependence of the P-factor	4
1.4	Influence of the Z=40 subshell gap on mixed-symmetry states	4
2.1	F-Spin symmetry in heavy nuclei	10
2.2	The Q-phonon scheme	12
2.3	Single-particle spectra for ^{92}Zr calculated using the QPM	14
2.4	The proton and neutron BCS ground state of ^{92}Zr	15
2.5	Quasiparticle spectrum of ^{92}Zr	15
3.1	Floor plan of the S-DALINAC	20
3.2	The Lintott Spectrometer	21
3.3	Focale plane detectorsystem	22
3.4	Floor plan of the iThemba LABS facility	23
3.5	The K600 Spectrometer	23
4.1	Representative spectra of the $^{92}\text{Zr}(p,p')$ and $^{94}\text{Mo}(p,p')$ reactions	25
4.2	Cross sections of the $^{92}\text{Zr}(p,p')$ -experiment	30
4.3	Cross sections of the $^{92}\text{Zr}(p,p')$ -experiment	31
4.4	Cross sections of the $^{94}\text{Mo}(p,p')$ -experiment	34
4.5	Cross sections of the $^{94}\text{Mo}(p,p')$ -experiment	35
4.6	Isoscalar quadrupole and hexadecapole strengths distributions in ^{92}Zr	36
4.7	Isoscalar quadrupole and hexadecapole strengths distributions in ^{94}Mo	36
4.8	Electron scattering spectra of ^{92}Zr	38
5.1	Comparison of the calculated and measured excitation energies in ^{92}Zr	41
5.2	Proton and neutron transition densities of the symmetric- and mixed-symmetric state	43
5.3	Matter transition densities of the symmetric- and mixed-symmetric state	44
5.4	Electron scattering formfactors compared to QPM calculations	44
5.5	Proton scattering cross sections compared to QPM calculations	45
5.6	Proton scattering data measured at 200 MeV	45
5.7	New signature for identifying a mixed-symmetry state	46
5.8	Running sums of B(E2)- and B(M1)-values for the symmetric and mixed-symmetric states	49
5.9	Various observables calculated in the '3-state model' in dependence of the coupling strength to the GQR	50
5.10	Various observables calculated in the '3-state QRPA model' in dependence of the coupling strength to the GQR	52
5.11	Avoided level crossing in the Mo chain	53
5.12	Deformation dependence of the B(M1) strength of mixed-symmetry states	54

List of Tables

2.1	Parameters of the Woods-Saxon potential used to calculate the properties of ^{92}Zr and ^{94}Mo	13
3.1	Properties of the Lintott Spectrometer	21
4.1	Main parameters of the $^{92}\text{Zr}(p,p')$ - and $^{94}\text{Mo}(p,p')$ -experiments.	24
4.2	Optical potential parameters used for ^{92}Zr	27
4.3	Results of DWBA analysis of the $^{92}\text{Zr}(p,p')$ experiment	28
4.4	Results of the $^{94}\text{Mo}(p,p')$ -experiment	32
4.5	Main parameters of the $^{92}\text{Zr}(e,e')$ reaction	37
4.6	Form factor of the symmetric and mixed-symmetric states of ^{92}Zr	39
5.1	Structure of the lowest 2^+ states in terms of QRPA phonons	40
5.2	Structure of the QRPA-phonons in terms of two-quasiparticle states	41
5.3	Comparison of the calculated and measured transition strengths in ^{92}Zr	42
5.4	Comparison of the calculated and measured g -factors in ^{92}Zr	42
5.5	Proton, neutron and matter transition radii of the symmetric and mixed-symmetric states	43
5.6	Comparison of the full QRPA to the '3-state model' and the '3-state QRPA model' in ^{92}Zr	50
5.7	Comparison of the full QRPA to the '3 state model' and the '3-state QRPA model' in ^{94}Mo	51
5.8	Comparison of the full QRPA to the '3 state model' and the '3-state QRPA model' in ^{96}Mo	51
5.9	$B(M1)$ strengths and g -factors in ^{92}Zr , ^{94}Mo and ^{96}Mo	53
5.10	Summary of experimental properties of mixed-symmetry states	56

1 Introduction

The atomic nucleus is a finite, complex, fermionic many-body system with well-defined proton and neutron numbers. Although its size is negligible - the radii of the whole atom and its nucleus differ by four to five orders of magnitude - the atomic nucleus is responsible for 99% of the visible matter in the universe. Obtaining a description of its properties and understanding the forces between its constituents - starting from the fundamental theory of the strong interaction: Quantum Chromodynamics (QCD) - is the key point of nuclear structure research.

To reach this target one has to face several complicated challenges. It would be favourable to achieve a description of nuclei in terms of the fundamental degrees of freedom in QCD: Quarks and Gluons. Unfortunately nuclear structure phenomena take place in the low energy sector of QCD, therefore perturbative methods are ruled out. Lattice-QCD exhibits the only way to perform calculations in this energy regime. Since these calculations require enormous computational resources they just start to become feasible and predictive for mesons and baryons. Describing a complex many-body system like the nucleus is - even for the deuteron - illusory. One has to apply a different strategy in order to link nuclei with QCD. The most consistent way is given by Chiral Effective Field Theory (EFT) [Wei79, Leu94].

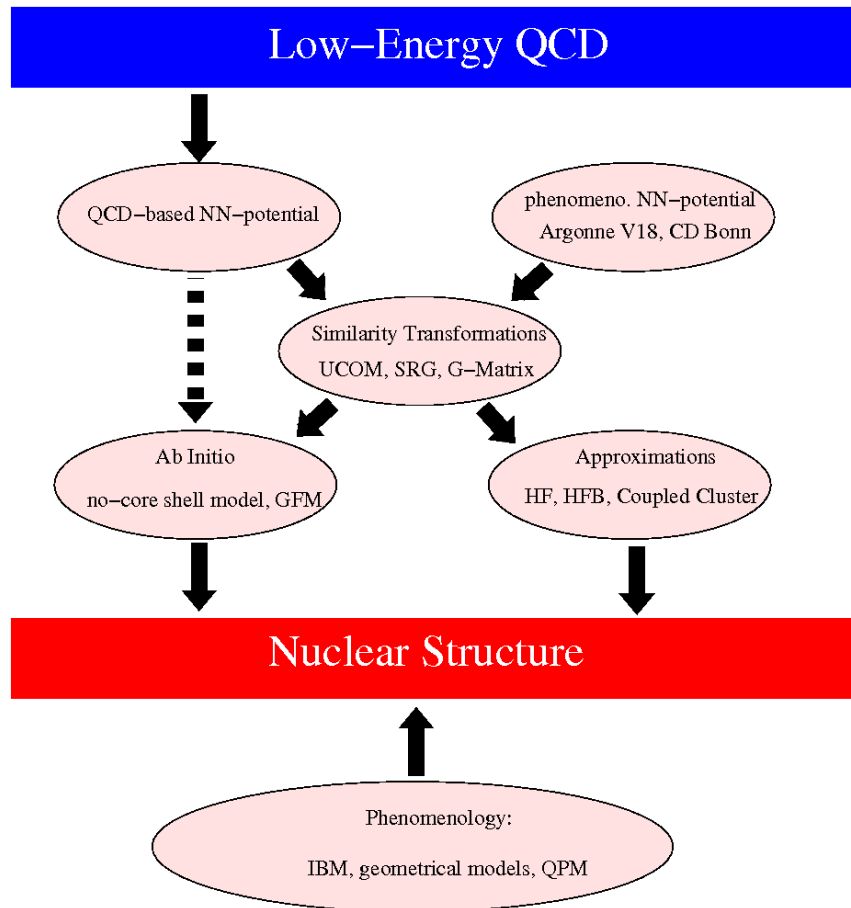


Figure 1.1: Shown is an overview about the theoretical strategies how to tackle the nuclear many body-problem. The upper part describes how to build the bridge between QCD and nuclear structure and the lower part discusses phenomenological approaches.

In this approach protons, neutrons and pions form the effective degrees of freedom and it is possible to construct a nucleon-nucleon potential whose properties are directly related to QCD. From the points made before it becomes clear that the nuclear force is only an effective one very similar to the van der Waals interaction between neutral atoms. In the last years large progress has been achieved in this field and nowadays such potentials are available fitting the scattering phase shifts until the cut off parameter used in the EFT [Epl09]. Very often more phenomenological potentials are used like the Argonne V18 [Wir98] and CD-Bonn potentials [Mac01].

Even given a suitable nucleon-nucleon potential calculating the properties of nuclei is not straight forward. One aims to stay as close as possible to an *ab initio* treatment of the nuclear many-body problem - *i.e.* solving the non-relativistic Schrödinger or the relativistic Dirac equation without approximations. The most common *ab initio* approaches are the Greens Function Monte Carlo technique (GFM) [Piep03] and the no-core shell model [Nav03]. Both methods are in principle able to start with a bare nucleon-nucleon potential and achieve a successful description of many properties of light nuclei. Since their computational demand increases exponentially with increasing nucleon numbers these programs can be carried out only for the lightest nuclei ($A \lesssim 12$). Therefore it is necessary to truncate the model space in order to tackle heavier nuclei *i.e.* the Schrödinger equation is solved only approximately. These simplified model spaces are not capable to describe short range correlations induced by the nuclear force namely central and tensor correlations. Hence the bare nucleon-nucleon interaction has to be renormalized for transforming the eigenvalue problem in the full space to an equivalent one in the much smaller model space. This can be done by the Brueckner G-matrix [Day67] or similarity transformations like V_{low-k} (SRG) [Bog03] or UCOM [Fel98, Nef03]. Many approximate methods have been developed in the past. Well known examples are Hartree-Fock (HF), Hartree-Fock-Bogoliubov (HFB) or the conventional shell model with a core. At the moment more refined methods are under development approximating the Schrödinger equation on a much more *controlled* way than the three examples mentioned before. Promising examples are the coupled cluster method [Kow04] and the no-core shell model with an importance truncation [Rot07] developed by R. Roth and co-workers.

The previous sections describe the way how the nuclear many-body problem should be tackled to stay on a fundamental level. However there exist a large number of phenomenological models which has proven to be successful in interpreting nuclear spectra, transition strengths and in classifying excitation modes. Famous examples are algebraic approaches like the Interacting Boson Model [Ari75, Ari78, Ari77] which uses different degrees of freedom namely bosons and geometrical models which treat the nucleus as a geometric entity [Boh75]. Both models are assumed to account for simple, collective excitations like vibrations in spherical nuclei or rotations in deformed nuclei. In addition many microscopic approaches use a purely phenomenological interaction *e.g.* the Quasi-Particle Phonon Model (QPM) [Sol92, Ber99] or the shell-model with a simple δ - function as interaction. With increasing computational capabilities and the advances in constructing effective interactions, phenomenological approaches become more and more replaced by microscopic treatments starting from a realistic nucleon-nucleon potential. Figure 1.1 summarizes the different theoretical strategies how to improve our understanding of nuclear structure.

For testing and improving nuclear models a large amount of experimental data is essential. Especially experiments and observables are needed which give new insights in the nature of the effective nuclear force. In general a very promising way to investigate the properties of a quantum system is bringing it to extreme conditions [NuP04] be it- in the case of nuclei- the proton to neutron ratio, isospin or binding energy. This will amplify or suppress certain parts of the nuclear interaction allowing to investigate these specific parts in detail. Radioactive beam physics constitutes an excellent way to achieve this for nuclei. Although radioactive beams are not available since two decades, this modern and experimentally very demanding branch of nuclear physics caused the discovery of many new structural phenomena like halo nuclei [Tan85], neutron skins or proton-neutron pairing. Describing and understanding these is a very challenging task for theory and indeed many models - accounting for the properties of stable nuclei successfully - have serious problems when extrapolated to exotic nuclei. An example which nicely illustrates the points mentioned above is the monopole tensor force whose important role in the evolution of shells has been stressed by Otsuka *et al.* [Ots01] recently. In stable nuclei its influence is somehow covered, however in exotic nuclei this part of the nuclear hamiltonian changes and causes new magic numbers very different from those found in stable nuclei. In the next years one can expect great improvements in nuclear structure physics induced by radioactive beam facilities like FAIR, RIKEN, TRIUMPF and REX-ISOLDE.

Shell effects and single-particle degrees of freedom dominate the structure of low-lying states in magic or semi-magic nuclei. If just a few valence nucleons are added so that both types - protons and neutrons - are present, one observes the fascinating structural evolution of nuclei. First - in nearly spherical nuclei - a vibrator structure develops, forming multiplets of collective states which can be reasonably approximated by the harmonic oscillator. Adding more and more valence nucleons the nucleus starts to deform. Finally, when the critical point is reached, it undergoes a shape phase transition - a highly interesting and extensively studied phenomena in nuclei [Iac00, Iac98]. The proton-neutron interaction - being responsible for configuration mixing [Sha53] - is the driving force behind this key point of nuclear structure research. Its importance has been first recognized by Shalit and Goldhaber [Sha53] in 1953 and repeatedly stressed by many others like Talmi [Tal62], Federman and Pittel [Fed78] or very recently Otsuka *et al.* [Ots01]. Phenomenologically, the strength of the proton-neutron interaction has been codified in the $N_\pi N_\nu$ -scheme by Casten [Cas85].

Clearly, experimental observables which are sensitive to this key ingredient of nuclear structure physics are extremely valuable for understanding and investigating the nuclear-many body problem. In 1984 Iachello [Iac84] predicted a new class of low-lying isovector collective states in the framework of the interacting-boson model 2 (IBM-2) [Ari77]. These so called 'mixed-symmetry states' (MSS) exhibit the intriguing property of being non-symmetric with respect to the proton-neutron degree of freedom. This feature makes them very different from other low-lying collective states being symmetric. The first known example - and maybe the most famous one - was the 1^+ scissors mode discovered by Richter and his group in the heavy deformed nucleus ^{156}Gd [Boh84]. This pioneering key experiment of mixed-symmetry research has been performed at the S-DALINAC in electron scattering. So far a large amount of data on this mode has been accumulated. Even in weakly collective nuclei a 1^+ mixed-symmetry state is known [Pie99, Pie20]. It is important to note that only valence nucleons contribute to this excitation in sharp contrast to the

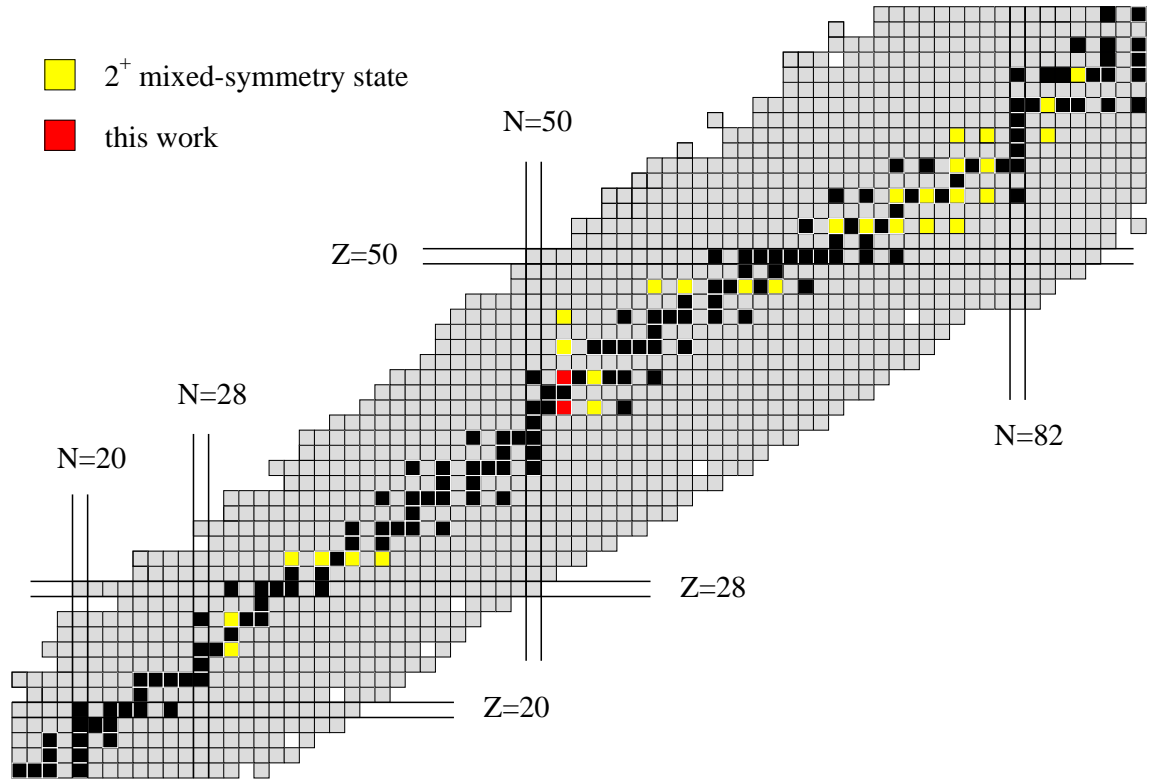


Figure 1.2: Section of the nuclei chart. Marked are the nuclei where a 2^+ mixed-symmetry state has been identified on the basis of absolute transition strength. No examples are known in the $A \approx 200$ region.

properties of an other isovector mode: The Giant Dipole Resonance (GDR). The GDR is mainly formed by $1\hbar\omega$ excitation [Wou87] *i.e.* nucleons are excited above closed shells resulting in a much higher excitation energy than the scissors mode.

The focus of this thesis is on an other kind of mixed-symmetry states. In 1984 Hamilton [Ham84] suggested the first example of a weakly collective 2^+ mixed-symmetry state in vibrational nuclei based on the analysis of E2/M1 multipole mixing ratios. Its main experimental signature is a strong B(M1)-strength to the 2_1^+ and a weakly collective B(E2)-strength to the ground state [Pie08]. In general detecting a transition between two excited states exhibits a challenging task and requires the combination of complementary experimental techniques. Hence the knowledge about this mode stayed sparse in the 1980s and 1990s. There were only a few examples based on absolute transition strength reported in Refs. [Lie88, Ver88, Van95, Gar96, Wie97, Faz92]. In the late 1990s the situation changed with the improvement of several experimental techniques which allows to determine the decay pattern of states far off the yrast band [Pie98a, Pie99]. The prime example of 2^+ mixed-symmetry states was identified by Pietralla *et al.* in ^{94}Mo [Pie99]. Not only the B(M1)-strength is very large in this nucleus - indicating a very 'clean' mixed-symmetry state - but also a multiphonon structure has been observed [Pie99, Pie20] which is formed by the symmetric and the mixed-symmetric 2^+ phonons. This observation proves that both phonons can be considered as building blocks of collective nuclear structure in nearly spherical nuclei. Nowadays a large amount of data about this excitation mode is available [Pie08] as shown in Fig. 1.2. All of them are located near closed shells. Unfortunately no example in radioactive nuclei has been identified so far. This can be traced back to the difficulties in measuring the B(M1)-strength in radioactive nuclei.

As stressed by Heyde and Sau [Hey86] the properties of 2^+ mixed-symmetry states are directly sensitive to the effective proton-neutron interaction. Near closed shells one observes a highly exciting phenomenon: The structure of both 2^+ phonons contains - besides a collective part - large single particle contributions [Iac06, Iud08]. This opens up the opportunity to study in detail the interplay between collective and single particle degrees of freedom when going from spherical to more collective nuclei driven by the proton-neutron interaction. Since usually only two large single particle components - one proton and one neutron - are present, one can draw conclusions about shell structure and the strength of the proton-neutron interaction investigating the configuration mixing between these large components. The B(M1)-strength between the MSS and 2_1^+ state and the g-factors of both states are excellent experimental observables for measuring the degree of mixing. This is highlighted by comparing the 2_1^+ state and MSS structures in ^{92}Zr and ^{94}Mo . Since ^{92}Zr lies at a proton subshell gap (Fig. 1.4) the proton two-quasiparticle state is located at much higher energy causing a drastically larger energy difference between the lowest proton and neutron two-quasiparticle configurations than in ^{94}Mo . As a result the proton-neutron interaction mediates in ^{92}Zr a smaller configuration mixing than in ^{94}Mo resulting in a smaller B(M1)-strength and a negative g-factor of the 2_1^+ state [Fra03, Fra05]. Clearly, 2^+ mixed-symmetry states constitute a very fine probe for exploring nuclear structure, sensitive to tiny shell effects and the detailed strength of the proton-neutron interaction.

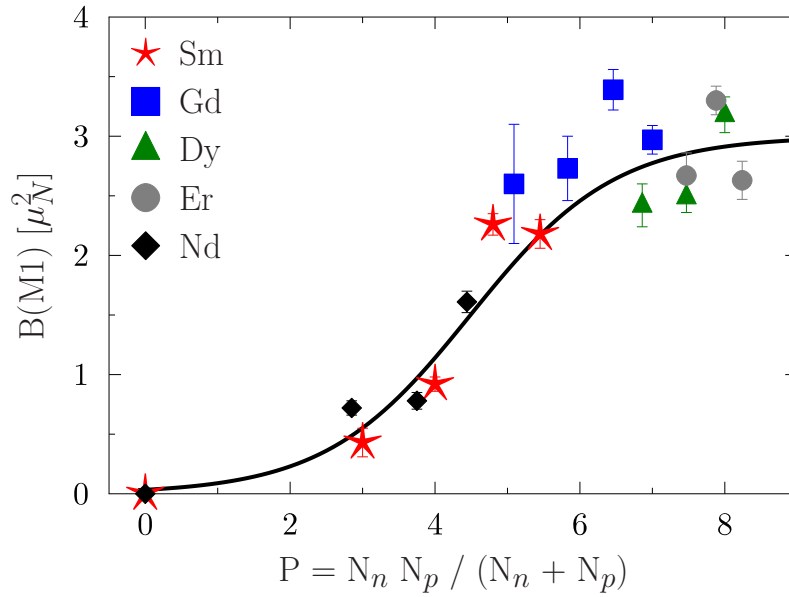


Figure 1.3: The B(M1)-strength of the scissors mode in the rare-earth region exhibits a smooth dependence on the P-factor indicating that the properties of the scissors mode are mainly determined by an interplay between the integrated pairing and proton-neutron force in the valence space.

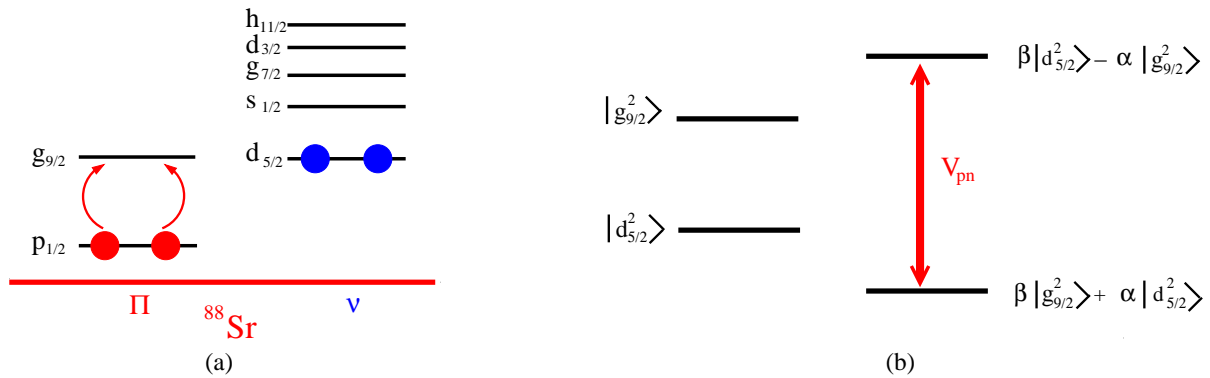


Figure 1.4: Shown is the shell structure for ^{92}Zr (a). Since $Z = 40$ is a subshell gap the lowest proton two-quasiparticle state is at much higher energy than the lowest neutron two-quasiparticle state resulting in weak configuration mixing with $\alpha \gg \beta$ (b).

In heavy-mass, deformed nuclei - the regime of the scissors mode - the situation is different. Configuration mixing and the proton-neutron interaction become so pronounced that many thousand quasiparticle states contribute to collective excitations washing out completely shell effects and influences of specific quasiparticle states. Investigations as in ^{92}Zr and ^{94}Mo are therefore prohibited. Figure 1.3 displays the summed B(M1)-strength of the scissors mode in the rare earth region over $P = (N_\pi N_\nu)/(N_\pi + N_\nu)$ with N_π (N_ν) being the number of valence protons (neutrons). The P-factor [Cas87] is believed to reveal qualitatively the competition between the *integrated* pairing force ($\sim N_\pi + N_\nu$) and the *integrated* proton-neutron interaction ($\sim N_\pi N_\nu$) in the *valence space*. The B(M1)-strength depends smoothly on this quantity indicating that the properties of the scissor mode are mainly determined by an interplay between these two integral quantities. One can take the 2^+ mixed-symmetry state as very fine probe of nuclear structure being sensitive to the details while the scissors mode is a crude probe being sensitive to overall properties of nuclei.

The typical strategy how to learn more about the nucleus and its constituents is to make use of external fields and to analyse the response. In order to obtain complementary experimental informations about the nature of an excitation mode it is important to use different probes interacting strongly, electromagnetically or weakly. So far gamma spectroscopy has been the main experimental technique for investigating the properties of 2^+ mixed-symmetry states. This method gives access to absolute electromagnetic transition strengths *i.e.* only the structure of the proton wavefunction is tested. This work investigates the 2^+ mixed-symmetry states in ^{92}Zr and ^{94}Mo in electron - and proton scattering. Since protons interact at medium energies isoscalarly [Fra85] with the nucleus a detailed test of the neutron wavefunction is possible. In addition energy and momentum transfers are decoupled in proton - and

electron scattering experiments allowing to explore nuclear structure at different momentum transfers which is impossible in gamma spectroscopy.

Collective vibrations are not limited to the atomic nucleus alone. They constitute a general feature of other quantum systems. The two fluid character of nuclei is the basic necessity for forming mixed-symmetry states. Thus it is not surprising to find mixed-symmetry states in other two fluid quantum systems as well. For example analogue scissors-mode states have been found in trapped Bose-Einstein Condensates [Gue99, Mar00] and metallic clusters [Nes99]. Since the investigated features of nuclei - collective vibrations and mixed-symmetry states - are widespread phenomena in physics this work should be of rather broad interest.

This thesis is organized as follows. The next chapter gives a brief summary of the nuclear structure models used in this work: the IBM and the QPM. The experimental setup and data taking conditions are described in Chapter 3. The next chapter discusses data analysing methods and presents measured cross sections for proton and electron scattering at ^{92}Zr and ^{94}Mo . Spin and parity quantum numbers of the various states are assigned using the collective model. The extracted isoscalar $B(E2)$ - and $B(E4)$ -strengths distributions are compared to QPM calculations. Chapter 5 presents a new signature for identifying a mixed-symmetry state independently of $M1$ -matrixelements. Moreover a simple picture is discussed about the microscopic origin of the effective proton-neutron interaction used the IBM-2. The simple picture allows to introduce a '3-state model' which explains the properties of MSS in the $N=50$ region. The results of this thesis are summarized in Chapter 6 and an outlook for future applications is given.

2 Theoretical descriptions

This chapter gives an outline about the nuclear structure models used in this thesis. The first one is the Interacting Boson Model 2 (IBM-2) introduced by Arima and Iachello in 1984. It starts from a purely phenomenological ansatz using bosons as effective degrees of freedom. Typically, this approach is the first choice when mixed-symmetry states are discussed in literature. In heavy deformed nuclei - the region of the scissors mode - the IBM-2 works very well achieving an excellent description of a large number of nuclear properties. However near closed shells - *e.g.* in ^{92}Zr and ^{94}Mo - where shell effects become important and only a few bosons are present, the IBM-2 - obscuring any shell structure - is not the best choice. Therefore in this thesis it is used for classifying nuclear excitations and defining the experimental signatures of mixed-symmetry states. This will be done in the first part of this chapter.

In the second part the focus is on the Quasi-Particle-Phonon Model (QPM) - the main theoretical tool in this work. Like the IBM-2 the QPM is phenomenological though microscopic, making it possible to describe nuclei near closed shells. Since the QPM is a QRPA based model it uses a huge single particle basis including in principle all relevant shells for the description of Giant Resonances as well as low-lying states, *i.e.* no effective charges are necessary.

2.1 The Interacting Boson Model

Several years the shell-model and the geometrical model of Bohr and Mottelson had been the only theoretical approaches to nuclear structure. In 1974 the situation changed with the development of the Interacting Boson Model (IBM) by Arima and Iachello [Iac87]. The outstanding feature of this model is the application of group theoretical methods to nuclear structure physics allowing in many cases a very intuitive and simple interpretation of nuclear structure phenomena. In the following the IBM-1 and its extension the IBM-2 are discussed with a special focus on mixed-symmetry states and the related F-Spin symmetry.

2.1.1 The Interacting Boson Model 1

The IBM-1 [Iac87] is a purely phenomenological model. Its basic assumption is that collective low-lying states in even-even nuclei can be described by a fixed number of bosons having angular momentum and parity $J=0^+$ (s-boson) and $J=2^+$ (d-boson). The restriction to s- and d-boson stems from the observation that the residual interaction between like nucleons is strongest in the $J=0$ and $J=2$ channels. So the microscopic counterparts of s- and d-boson are correlated fermion pairs in the shell model. It is possible to enlarge the model space and take into account *e.g.* g-bosons. Fixing the boson number is the fundamental difference to the geometrical model causing several predictions where both approaches differ seriously. In the IBM-1 - the simplest version of the interacting boson model - no distinction is made between protons and neutrons - the nucleus is considered as a one component system. This restriction is lifted in the IBM-2 which explicitly distinguishes between proton and neutron bosons as described in the next section. The IBM considers only single boson energies for s-boson as well as for d-bosons, so clearly it cannot account for any shell effects. Therefore the model space of the IBM-1 is six dimensional, spanned by the single substate of the s-boson and the five magnetic substates of the d-boson. To construct a suitable hamiltonian the following points have to be taken into account:

- The hamiltonian must fulfill rotational symmetry, hermicity and the pauli-principle,
- the interaction between bosons is assumed to be of two-body character,
- since the hamiltonian must conserve the boson number every creation-operator must be combined with a destruction-operator.

Using the tensorproduct, it is possible to couple two spherical tensors to a new one with defined angular momentum

$$[\mathbf{T}^{(l_1)} \times \mathbf{T}^{(l_2)}]_m^{(l)} = \sum_{m_1, m_2} \langle l_1 m_1 l_2 m_2 | l m \rangle \mathbf{T}_{m_1}^{(l_1)} \mathbf{T}_{m_2}^{(l_2)}. \quad (2.1)$$

A scalar ($l=0$) spherical tensor is trivially invariant under rotations. Therefore the most general, rotational invariant hamiltonian describing the bosonic system can be written as a weighted sum of all possible scalars which can be formed considering points two and three

$$\mathbf{H} = E_0 + \epsilon_s(\mathbf{s}^\dagger \mathbf{s}) + \epsilon_d(\mathbf{d}^\dagger \mathbf{d}) + \sum_{l_1 l_2 l'_1 l'_2 L} v_{l_1 l_2 l'_1 l'_2}^L [[\mathbf{b}_{l_1}^\dagger \times \mathbf{b}_{l_2}^\dagger]^{(L)} \times [\tilde{\mathbf{b}}_{l'_1} \times \tilde{\mathbf{b}}_{l'_2}]^{(L)}]_0^{(0)}, \quad (2.2)$$

where $\tilde{\mathbf{b}}_{lm} = (-1)^{l+m} \mathbf{b}_{l-m}$. The number of terms can be reduced when the requirement of symmetry under the pauli-principle and hermicity is taken into account. If in addition terms which contribute to the binding energy are neglected the hamiltonian can be written as

$$\mathbf{H} = \epsilon'' \mathbf{n}_d + a_0 \mathbf{P}^\dagger \cdot \mathbf{P} + a_1 \mathbf{L}^\dagger \cdot \mathbf{L} + a_2 \mathbf{Q}^\dagger \cdot \mathbf{Q} + a_3 \mathbf{T}_3^\dagger \cdot \mathbf{T}_3 + a_4 \mathbf{T}_4^\dagger \cdot \mathbf{T}_4, \quad (2.3)$$

where $\mathbf{T}^{(l_1)} \cdot \mathbf{T}^{(l_2)} := [\mathbf{T}^{(l_1)} \times \mathbf{T}^{(l_2)}]_0^{(0)}$ is a short-hand notation for the scalar product. The operators stand for

$$\begin{aligned} \mathbf{P} &= \frac{1}{2}(\mathbf{d}^\dagger \cdot \tilde{\mathbf{d}} - \mathbf{s}^\dagger \cdot \mathbf{s}) \\ \mathbf{T}_l &= [\mathbf{d}^\dagger \times \tilde{\mathbf{d}}]^{(l)} \quad ; l = 0, 1, 2, 3, 4 \\ \mathbf{Q}^\chi &= (\mathbf{d}^\dagger \cdot \mathbf{s} + \mathbf{s}^\dagger \cdot \tilde{\mathbf{d}}) - \chi \mathbf{T}_2 \\ \mathbf{n}_d &= \sqrt{5} \mathbf{T}_0 \\ \mathbf{L} &= \sqrt{10} \mathbf{T}_1. \end{aligned} \quad (2.4)$$

In this form the appearing terms contain at least superficially a more intuitive interpretation: \mathbf{L} is the angular momentum operator, \mathbf{P} the so called pairing operator and \mathbf{Q}^χ , \mathbf{T}_3 and \mathbf{T}_4 represent quadrupole, octupole and hexadecapole operators. However one should always keep in mind that these operators act on boson states, therefore no direct connection to fermionic counterparts can be drawn. The weighting factor are adjusted to the experimental data reflecting the phenomenological treatment of the IBM. Depending on the mass region different terms of the hamiltonian are dominating concerning their influence on nuclear structure properties.

The IBM offers the possibility to apply easily group theoretical concepts and symmetries to nuclear physics. In nearly all fields of physics symmetries play a fundamental role causing conservation laws like momentum, energy and parity conservation. A hamiltonian is said to have the symmetry G , if the corresponding generators \mathbf{g}_i of the group G - forming a Lie-Algebra - fulfill the condition

$$\forall \mathbf{g}_i \in G : [\mathbf{H}, \mathbf{g}_i] = 0. \quad (2.5)$$

An important consequence of a symmetry is the degeneracy of eigenstates. Suppose $|\gamma\rangle$ is an eigenstate of the hamiltonian \mathbf{H} with energy E , then follows with Eq.2.5 that all states $\mathbf{g}_i|\gamma\rangle$ have the same energy

$$\mathbf{H} \mathbf{g}_i |\gamma\rangle = \mathbf{g}_i \mathbf{H} |\gamma\rangle = E \mathbf{g}_i |\gamma\rangle. \quad (2.6)$$

To label an eigenstate of \mathbf{H} distinct, one needs at least two quantum numbers $|\Gamma\gamma\rangle$. Γ labels states with different energy and γ distinguishes between degenerated states. Casimir-operators \mathbf{C}_m are an other important concept. They commute with every generator of the group G :

$$\forall \mathbf{g}_i \in G : [\mathbf{C}_m, \mathbf{g}_i] = 0. \quad (2.7)$$

The hamiltonian contains automatically the Symmetry G , if it can be written as a sum of Casimir-operators of the group G :

$$\mathbf{H} |\Gamma\gamma\rangle = \sum_m k_m \mathbf{C}_m [G] |\Gamma\gamma\rangle = \sum_m k_m E_m |\Gamma\gamma\rangle \quad (2.8)$$

For the IBM the concept of the so called *dynamical symmetry* is of fundamental importance. Suppose a Lie-Algebra G_2 fulfilling the condition $G_1 \supset G_2$. Obviously G_2 is also a symmetry of the hamiltonian with the eigenstates $|\Gamma_2\gamma_2\rangle$. The combination of both properties leads to the eigenvalue problem:

$$\mathbf{H} |\Gamma_1\gamma_1\Gamma_2\gamma_2\rangle = E(\Gamma_1) |\Gamma_1\gamma_1\Gamma_2\gamma_2\rangle. \quad (2.9)$$

The energies solely depend on Γ_1 . Typically the requirement of G_1 being the symmetry is too strong and the hamiltonian can be written as

$$\mathbf{H}' = \sum_{m_1} k_{m_1} \mathbf{C}_{m_1} [G_1] + \sum_{m_2} k_{m_2} \mathbf{C}_{m_2} [G_2]. \quad (2.10)$$

Since \mathbf{H}' contains the Casimir-operators of G_2 not all generators of G_1 will commute. G_1 is no longer a symmetry of \mathbf{H}' but G_2 . However, because \mathbf{H}' is a combination of Casimir-Operators of G_1 and G_2 its eigenvalues can be obtained analytically

$$\mathbf{H}' |\Gamma_1\gamma_1\Gamma_2\gamma_2\rangle = \left(\sum_{m_1} k_{m_1} E_{m_1}(\Gamma_1) + \sum_{m_2} k_{m_2} E_{m_2}(\Gamma_2) \right) |\Gamma_1\gamma_1\Gamma_2\gamma_2\rangle. \quad (2.11)$$

The essential point is that the eigenstates of \mathbf{H} and \mathbf{H}' are the same but split in energy. One says that the hamiltonian \mathbf{H}' contains G_1 as a *dynamical symmetry*. The generalisation is straightforward and can be applied to chains of algebras

$$G_1 \supset G_2 \supset G_3 \supset \dots \supset G_\Omega. \quad (2.12)$$

G_1 until $G_{\Omega-1}$ are the dynamical symmetries of the system while G_Ω is the true symmetry of \mathbf{H}' in the sense of Eq.2.5.

How can this formalism be applied to the IBM? The d-boson with its 5 magnetic substates and the s-boson span a six-dimensional vectorspace. The most general, particle number conserving transformations are given by the 36 bilinear combinations of the type $\mathbf{b}_{l,m}^\dagger \mathbf{b}_{l',m'}$ whose explicit expressions are given in Ref. [Iac87]. They form a unitary, six dimensional Lie-Algebra named $U(6)$. Similarly to Eq. 2.12 it is possible to divide the $U(6)$ in subalgebras which must contain the $O(3)$ for being physically relevant. Clearly, the underlying reason is that angular momentum must be a good quantum number. There are exactly three chains which fulfill this condition

$$U(6) \left\{ \begin{array}{l} \supset U(5) \supset O(5) \\ \supset SU(3) \\ \supset O(6) \supset O(5) \end{array} \right\} \supset O(3), \quad (2.13)$$

named after the highest dimensional subalgebra of $U(6)$: $U(5)$, $SU(3)$ and $O(6)$, respectively. The IBM-1 hamiltonian of Eq.2.3 can be expressed as a sum of Casimir-operators

$$\begin{aligned} \mathbf{H} = & e_0 + e_1 \mathbf{C}_1(U(6)) + e_2 \mathbf{C}_2(U(6)) + \eta \mathbf{C}_2(O(6)) + \tilde{\epsilon} \mathbf{C}_1(U(5)) \\ & + \alpha \mathbf{C}_2(U(5)) + \beta \mathbf{C}_2(O(5)) + \delta \mathbf{C}_2(SU(3)) + \gamma \mathbf{C}_2(O(3)) \end{aligned} \quad (2.14)$$

where \mathbf{C}_n is the Casimir-Operator of the n-th order of the corresponding group. If an appropriate set of parameters is chosen, the resulting hamiltonian contains only Casimir-Operators of one of the three chains given in Eq.2.13. Then the condition of Eq.2.12 holds and the solution of the eigenvalue problem can be obtained analytically. The three cases of the IBM-1 where this is possible - $U(5)$, $SU(3)$ and $O(6)$ - are usually referred to as 'limits'. They are the dynamical symmetries of the corresponding hamiltonian. Since the hamiltonian consists of commuting operators, the quantum number associated with each of the Casimir-operators are conserved and can be used to label the states. Moreover, the wavefunctions of the three limits are independent of the actual parameters providing distinct transition rates.

The existence of these limits is maybe the reason why the IBM became so successful. They provide an understanding of the range of collective nuclear structure which can be obtained within the IBM. Typically these dynamical symmetries are broken and the full IBM hamiltonian of Eq.2.3 has to be diagonalized numerically, however one can compare the properties of the nucleus of interest to the limiting cases - *e.g.* to the distinct transition rates - and make statements to which symmetry the nucleus is closest. Therefore the limits act as benchmarks bringing order in the diversity of nuclear spectra.

2.1.2 The Interacting Boson Model 2

The IBM-2 [Iac87] is the natural extension of the IBM-1 considering explicitly the neutron-proton degree of freedom. In contrast to the IBM-1 which is purely phenomenological, the IBM-2 has at least qualitatively a microscopic justification and in principle it is possible to derive the parameters of the IBM-2 from microscopic considerations. However, until today this connection is not quantitative, *i.e.* the derived parameter using the OAI-mapping [Ots78] differ from the one required to fit the data. This is a serious caveat of the IBM-2. The microscopic counterparts of s- and d-bosons are correlated nucleon pairs of the same type. The main problem of shell model calculations is the drastically increasing size of the model space when going from magic nuclei to open-shell systems. Typically, it would be necessary to diagonalize matrices of the dimension of $\sim 10^{20}$, a number where one could not even think of diagonalizing it. The IBM-2 can be seen essentially as a very vast and rough truncation of this huge shell model space reducing the problem even at midshell to matrices of $\sim 10^2$ which can be handled by conventional diagonalization techniques easily.

The most general IBM-2 hamiltonian has the form

$$\mathbf{H} = \mathbf{H}_\pi + \mathbf{H}_\nu + \mathbf{V}_{\pi\nu}. \quad (2.15)$$

\mathbf{H}_π and \mathbf{H}_ν have exactly the same form as the IBM-1 hamiltonian of Eq.2.3. The third term codifies the interaction between proton and neutron bosons and can be expressed in a multipole form

$$\begin{aligned} \mathbf{V}_{\pi\mu} = & c_0(\mathbf{n}_{d_\pi} \cdot \mathbf{n}_{d_\mu}) + c_1(\mathbf{L}_\pi \cdot \mathbf{L}_\mu) + c_2(\mathbf{Q}_\pi^\chi \cdot \mathbf{Q}_\mu^\chi) \\ & + c_3(\mathbf{Q}_\pi^\chi \cdot \mathbf{Q}'_\mu) + c_4(\mathbf{Q}'_\pi \cdot \mathbf{Q}_\mu^\chi) + c_5(\mathbf{Q}'_\pi \cdot \mathbf{Q}'_\mu) \\ & + c_6(\mathbf{Q}''_\pi \cdot \mathbf{Q}''_\mu) + c_7(\mathbf{U}_\pi \cdot \mathbf{U}_\mu) + c_8(\mathbf{V}_\pi \cdot \mathbf{V}_\mu). \end{aligned} \quad (2.16)$$

The multipole operators are given by

$$\begin{aligned}
\mathbf{n}_{d\rho} &= \mathbf{d}_\rho^\dagger \cdot \tilde{\mathbf{d}}_\rho \\
\mathbf{P}_\rho &= \frac{1}{2}(\mathbf{d}_\rho^\dagger \cdot \tilde{\mathbf{d}}_\rho) - \frac{1}{2}(\mathbf{s}_\rho^\dagger \cdot \mathbf{s}_\rho) \\
\mathbf{L}_\rho &= \sqrt{10}[\mathbf{d}_\rho^\dagger \cdot \tilde{\mathbf{d}}_\rho]^{(1)} \\
\mathbf{Q}_\rho^\chi &= [\mathbf{d}_\rho^\dagger \times \mathbf{s}_\rho + \mathbf{s}_\rho^\dagger \times \tilde{\mathbf{d}}_\rho]^{(2)} - \chi[\mathbf{d}_\rho^\dagger \times \tilde{\mathbf{d}}_\rho]^{(2)} \\
\mathbf{Q}'_\rho &= [\mathbf{d}_\rho^\dagger \times \tilde{\mathbf{d}}_\rho]^{(2)} \\
\mathbf{Q}''_\rho &= [\mathbf{d}_\rho^\dagger \times \mathbf{s}_\rho + \mathbf{s}_\rho^\dagger \times \tilde{\mathbf{d}}_\rho]^{(2)} \\
\mathbf{U}_\rho &= [\mathbf{d}_\rho^\dagger \times \tilde{\mathbf{d}}_\rho]^{(3)} \\
\mathbf{V}_\rho &= [\mathbf{d}_\rho^\dagger \times \tilde{\mathbf{d}}_\rho]^{(4)},
\end{aligned} \tag{2.17}$$

where ρ is either π or ν . Equation 2.15 is literally swarming with parameters and contains 21 free parameters - usually more than data points are available to fit them. In order to perform a meaningful calculation one has to reduce their number. The key idea is to orientate on the microscopic shell-model hamiltonian to decide which parts of the hamiltonian in Eq.2.15 are actually important. This way is not unique causing the existence of several IBM-2 Hamiltonians. The maybe most common and successful one is

$$\mathbf{H} = \epsilon_\pi \mathbf{n}_{d_\pi} + \epsilon_\nu \mathbf{n}_{d_\nu} + 2\kappa \mathbf{Q}_\pi \cdot \mathbf{Q}_\nu + \lambda \mathbf{M}_{\pi\nu}. \tag{2.18}$$

Equation 2.18 has a sound microscopic justification and mimics the common fermionic pairing-quadrupole hamiltonian. The fermionic analogon of the d-boson energies ϵ_π and ϵ_ν is the monopole pairing part, while the analogon of $2\kappa \mathbf{Q}_\pi \cdot \mathbf{Q}_\nu$ is the proton-neutron quadrupole interaction. $\mathbf{M}_{\pi\nu}$ is the so called Majorana-Operator which has no direct microscopic counterpart. Its most general form is

$$\begin{aligned}
\mathbf{M}_{\pi\nu} &= [\mathbf{s}_\nu^\dagger \times \mathbf{d}_\pi^\dagger - \mathbf{s}_\pi^\dagger \times \mathbf{d}_\nu^\dagger]^{(2)} \cdot [\mathbf{s}_\nu \times \tilde{\mathbf{d}}_\pi - \mathbf{s}_\pi \times \tilde{\mathbf{d}}_\nu]^{(2)} \\
&\quad - 2 \sum_{k=1}^3 [\mathbf{d}_\nu^\dagger \times \mathbf{d}_\pi^\dagger]^{(k)} \cdot [\tilde{\mathbf{d}}_\nu \times \tilde{\mathbf{d}}_\pi]^{(k)}
\end{aligned} \tag{2.19}$$

The underlying algebra of the IBM-2 is $U_\pi(6) \times U_\nu(6)$. The three dynamical symmetries $SU(3)$, $O(6)$ and $U(5)$ are still contained when proton and neutron parts are coupled on the $U(6)$ level and can be used for interpreting nuclear structure phenomena. The focus of this thesis is on an other symmetry of the IBM-2 Hamiltonian, the so called F-Spin.

On the nucleonic level isospin is approximately a good quantum number and a useful symmetry to describe nuclear systems and to simplify calculations. Protons and neutrons are treated as different states of one particle: the nucleon. On the bosonic level the F-Spin quantum number was introduced in Ref. [Ari77] as an analogue for bosons to the isospin concept for nucleons. The F-Spin quantum numbers for proton and neutron bosons are given by

$$\begin{aligned}
\mathbf{b}_\pi^\dagger |0\rangle &= \begin{cases} F = 1/2 \\ F_z = +1/2 \end{cases} \\
\mathbf{b}_\nu^\dagger |0\rangle &= \begin{cases} F = 1/2 \\ F_z = -1/2. \end{cases}
\end{aligned} \tag{2.20}$$

The treatment of proton and neutron bosons as an F-Spin doublet imposes an $SU(2)$ group structure, therefore isospin and F-Spin are mathematically identical. The generators of the $SU(2)$ group can be written as

$$\begin{aligned}
\mathbf{F}_+ &= \mathbf{d}_\pi^+ \tilde{\mathbf{d}}_\nu + \mathbf{s}_\pi^+ \mathbf{s}_\nu \\
\mathbf{F}_- &= \mathbf{d}_\nu^+ \tilde{\mathbf{d}}_\pi + \mathbf{s}_\nu^+ \mathbf{s}_\pi \\
\mathbf{F}_z &= \frac{1}{2} \left[\mathbf{d}_\pi^+ \tilde{\mathbf{d}}_\pi + \mathbf{s}_\pi^+ \mathbf{s}_\pi - \mathbf{d}_\nu^+ \tilde{\mathbf{d}}_\nu - \mathbf{s}_\nu^+ \mathbf{s}_\nu \right] \\
&= \frac{1}{2} (N_\pi - N_\nu).
\end{aligned} \tag{2.21}$$

\mathbf{F}_+ and \mathbf{F}_- enhance or lower F_z - being one half of the difference between proton and neutron boson numbers - by one unit. Since \mathbf{F}_+ , \mathbf{F}_- and \mathbf{F}_z form a Lie-Algebra they are close under commutation. As introduced in Eq.2.7 it is possible to define a Casimir-Operator for this algebra commuting with every generator

$$\mathbf{F}^2 = \mathbf{F}_- \mathbf{F}_+ + \mathbf{F}_z (\mathbf{F}_z + 1). \tag{2.22}$$

Conveniently F_z is chosen to label the states together with the corresponding eigenvalue of F^2 : $F(F+1)$. For a given number of proton and neutron bosons the F-Spin can take values between $F_{\min} = |N_\pi - N_\nu|/2$ and $F_{\max} = (N_\pi + N_\nu)/2$. F-Spin is a useful quantum number to classify the boson states with respect to their symmetry under pairwise proton and neutron exchange. Basis states that are characterized by a maximum F-Spin quantum number $F = F_{\max}$ can be transformed by successive action of the F-Spin raising operator F_+ into a state that consists of proton bosons only. Obviously, such a state is unchanged under pairwise exchange of proton and neutron labels since it does not contain any neutron bosons. Therefore, IBM-2 states with maximum F-spin quantum number are called *Fully-Symmetric States* (FSSs). All states with $F < F_{\max}$ contain at least one pair of proton and neutron bosons which behave antisymmetric under the exchange of proton and neutron labels. This class of states is investigated in this thesis and are referred to as *Mixed-Symmetry States* (MSSs).

The F-Spin is an exact symmetry if all generators of Eq.2.21 commute with the IBM-2 hamiltonian. F_z is per construction diagonal in a F-Spin basis, the remaining strong condition is $[F_\pm, \mathbf{H}] = 0$. The weaker condition for F-Spin being at least a good quantum number is given by $[F^2, \mathbf{H}] = 0$. However, the IBM-2 of Eq.2.18 is far from being a F-Spin scalar nor is it commuting with F^2 . So in principle one can expect F-Spin mixing between mixed-symmetric and fully-symmetric states preventing F-Spin of being a useful concept. The reason why F-Spin is nonetheless approximately a good quantum number is caused by the Majorana-term of Eq.2.19. This operator gives an overall energy-shift to states with $F < F_{\max}$ separating fully-symmetric and mixed-symmetric states. Since the degree of F-Spin mixing depends on the energy splitting between states of different F-Spin, the presence of the Majorana-term reduces this effect drastically. However, F-Spin mixing is not completely negligible, e.g. the A=100 region is known for strong F-Spin mixing effects [Kim96] signaled by M1-transition between low-lying states.

How would F-Spin symmetry show up in nuclear spectra? Suppose the chosen IBM-2 hamiltonian is a F-Spin scalar, then the excitation spectra of a set of nuclei with the same, fixed total boson number $N = N_\pi + N_\nu$ would be identical for all states with $F = F_{\max}$. Of course, the hamiltonian must be the same for all nuclei demanding an identical set of IBM-2 parameters. The various nuclei with different F_z would form degenerated F-Spin multiplets. In case of F-Spin being a good quantum number the multiplets are not necessarily degenerated. However, if the energy variation with F_z is small, one can hope to identify them. Figure 2.1 displays the low-lying states of a selected set of heavy nuclei. All have a total boson number of 13 and therefore form a F-Spin multiplet [Bre85] of $F_{\max} = 13/2$ ranging from $F_z = -7/2$ to $F_z = 3/2$. Since the levels are nearly degenerated, F-Spin is not only a good quantum

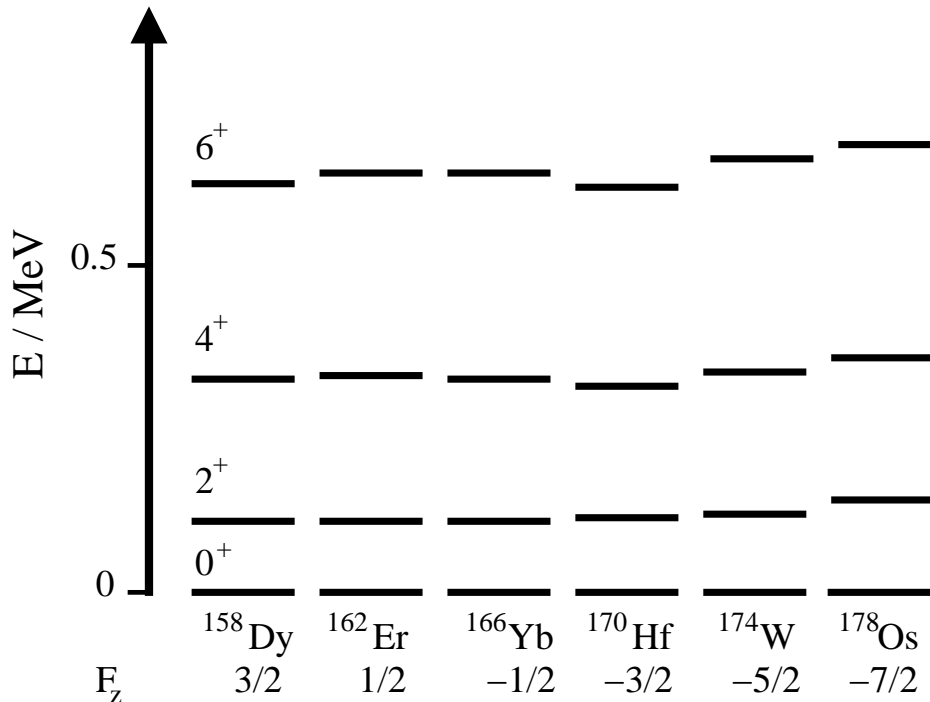


Figure 2.1: The experimental energy levels for selected nuclei belonging to an $F_{\max}=13/2$ multiplet. The levels are nearly degenerated proving that F-Spin symmetry is approximately fulfilled.

number but also the symmetry condition seems to be fulfilled to a large extent. It should be noted that no other reason exist to look at this set of nuclei expect F-Spin. One can consider F-Spin as a reasonable - unfortunately rarely known - symmetry in nuclei. In addition, the goodness of F-Spin is confirmed by the sheer fact that the IBM-1 - considering only states with $F = F_{\max}$ - works so well for low-lying states in general. Investigating the properties of MSS allows to test the validity of F-Spin symmetry for the states with $F < F_{\max}$.

The IBM-2 transition operators have a simple form using the multipole operators of Eq.2.17. The M1-transition operator is given by

$$\begin{aligned} \mathbf{T}(M1) &= \sqrt{\frac{3}{4\pi}} [g_\pi \mathbf{L}_\pi + g_\nu \mathbf{L}_\nu] \mu_N \\ &= \sqrt{\frac{3}{4\pi}} \left[\frac{N_\pi g_\pi + N_\nu g_\nu}{N} \mathbf{L}_{tot} + (g_\pi - g_\nu) \frac{N_\pi N_\nu}{N} (\mathbf{L}_\pi / N_\pi - \mathbf{L}_\nu / N_\nu) \right] \mu_N, \end{aligned} \quad (2.23)$$

g_π and g_ν denote the proton and neutron boson g-factors. Typically, $g_\pi=1$ and $g_\nu=0$ are chosen in calculations. \mathbf{L}_{tot} denotes the total angular momentum which is per construction a good quantum number and can not connect different states. Hence, transitions are solely induced through the second term of Eq. 2.23. This term can only induce M1-transitions between states which *differ by one unit of F-Spin* [Pie08]. Therefore M1-transitions are exactly forbidden between two fully-symmetric states. Since, no other M1-transitions are allowed, expect the one between a fully-symmetric state and a mixed-symmetric state, it can be used as a unique experimental signature for identifying mixed-symmetric states. The difference between the boson g-factor amounts to $\sim 1\mu_N$, consequently one can expect a M1-transition matrix element of the order of $\langle \text{FSS} || \mathbf{T}(M1) || \text{MSS} \rangle \approx 1\mu_N$. The E2-transition operator is given by

$$\mathbf{T}(E2) = e_\pi \mathbf{Q}_\pi^{Z_\pi} + e_\nu \mathbf{Q}_\nu^{Z_\nu}, \quad (2.24)$$

where the quadrupole operators $\mathbf{Q}_\pi^{Z_\pi}$, $\mathbf{Q}_\nu^{Z_\nu}$ can be found in Eq.2.17 and e_π , e_ν are boson effective charges accounting for states which contribute to the transition of interest but are not included in the small IBM-2 model space. Assuming that F-Spin symmetry is fulfilled, the M1- and E2- transition matrix elements are in general proportional to the following factors

$$\begin{aligned} \langle \text{FSS} || \mathbf{T}(M1) || \text{MSS} \rangle &\sim (g_\pi - g_\nu) \sqrt{N_\pi N_\nu} \\ \langle \text{FSS} || \mathbf{T}(E2) || \text{FSS} \rangle &\sim e_\pi N_\pi + e_\nu N_\nu \\ \langle \text{FSS} || \mathbf{T}(E2) || \text{MSS} \rangle &\sim (e_\pi - e_\nu) \sqrt{N_\pi N_\nu}. \end{aligned} \quad (2.25)$$

Note that also the ground state is a fully-symmetric state. Since $e_\pi \approx e_\nu$, the B(E2)-value between the 2_{ms}^+ and the ground state is reduced in contrast to the B(E2)-value connecting the 2_1^+ and the ground state. Typically the values amount to several W.u. for the 2_1^+ state and a weakly collective ~ 1 W.u. transition for the 2_{ms}^+ state.

It is always very pleasant to have simple schemes and pictures in order to understand and interpret complex nuclear structure calculations. The so called Q-phonon scheme is such a tool helping to understand the sometimes complicated results in the framework of the IBM. In case of the IBM-1 it is assumed that the IBM wavefunctions for low-lying states can be approximated by applying the quadrupole operator Q of Eq.2.4 on the strongly correlated ground state:

$$|2_1^+\rangle = N_Q \mathbf{Q} |0_1^+\rangle, \quad (2.26)$$

with N_Q being a proper normalization constant. Following the Q-Phonon scheme higher-lying states can be understood as multi-Q-Phonon excitation e.g. the two-phonon triplet

$$|J^+\rangle = N_{QQ}^{(J)} (\mathbf{Q}\mathbf{Q})^{(J)} |0_1^+\rangle \quad \text{with } J = 0, 2, 4. \quad (2.27)$$

Indeed, this scheme works very well and it has been shown in Ref. [Pie94] that the deviations between the full IBM-1 wavefunctions and the Q-phonon wavefunctions are always smaller than 7% for the 2_1^+ and the 4_1^+ .

In general one has to consider proton and neutron quadrupole operators as defined in Eq.2.17. Both operators can couple in a symmetric and in an antisymmetric way. The symmetric coupling is identical to the Q-phonon operator of Eq.2.26

$$\mathbf{Q}_s = \mathbf{Q}_\pi + \mathbf{Q}_\nu, \quad (2.28)$$

while the antisymmetric coupling

$$\mathbf{Q}_{ms} = \mathbf{Q}_\pi - c \mathbf{Q}_\nu, \quad (2.29)$$

offers the possibility to describe mixed-symmetry states in the Q-Phonon scheme [Pie98b]. The constant c ensures orthogonality to the symmetric state. The one-phonon 2_{ms}^+ occurs naturally by acting \mathbf{Q}_{ms} on the ground state

$$|2_{ms}^+\rangle = N_{ms} \mathbf{Q}_{ms} |0_1^+\rangle. \quad (2.30)$$

Besides the symmetric multi-phonon states of Eq.2.27 there exists an additional class of multi-phonon states caused by a coupling of the symmetric and the mixed-symmetric one-phonon states

$$|J^+\rangle = N_{ms}^{(J)} (\mathbf{Q}_{ms} \mathbf{Q}_s)^{(J)} |0_1^+\rangle \quad \text{with } J = 0, 1, 2, 3, 4. \quad (2.31)$$

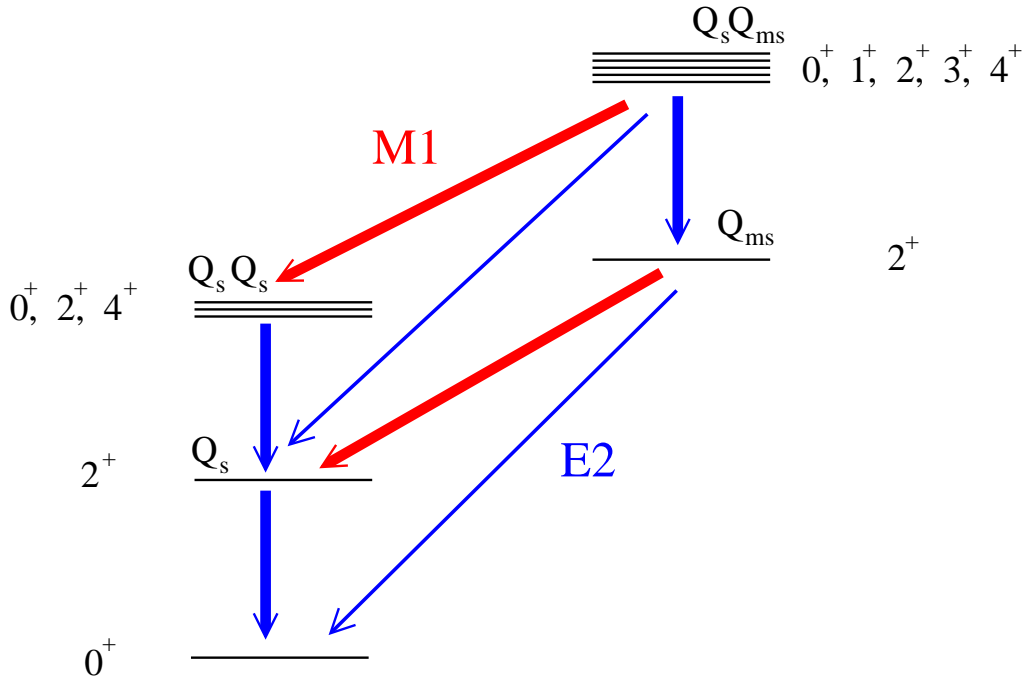


Figure 2.2: The symmetric and the mixed-symmetric one phonon states act as building blocks of collective nuclear structure. Shown are the experimental signatures for mixed symmetry states.

Since the phonons Q_s and Q_{ms} are distinguishable from each other, two-phonon states with quantum numbers 1^+ and 3^+ are allowed. As in the case of the IBM-1, it has been shown that also for the IBM-2 the Q-Phonon scheme gives a good approximation for the IBM-2 wavefunctions assuming good F-Spin. The Q-Phonon scheme makes the importance of the 2_1^+ and 2_{ms}^+ states apparent, they act as building blocks of collective nuclear structure. Figure 2.2 displays the multiphonon structures in vibrational nuclei in the Q-phonon scheme. Also shown are the expected decay properties concerning M1- and E2-transitions.

In summary the experimental signatures for a one-phonon quadrupole mixed-symmetric state are

- enhanced M1-matrixelement to the 2_1^+ of the order of $\sim 1\mu_N$
- weakly collective E2-transition to the ground state.

In the following the IBM-2 is not used for interpreting the MSS in ^{92}Zr and ^{94}Mo . The calculations are done in the QPM which is outlined in the next section. It is not easy to setup a quantitative connection between the MSS defined in the IBM-2 and the corresponding state of the QPM which shares the aforementioned properties. Hence, in this thesis the identification of the MSS in the framework of the QPM is simply done by searching for a state which exhibits the two crucial properties.

2.2 The Quasiparticle Phonon Model

The Quasiparticle Phonon Model (QPM) is a phenomenological, microscopic model. It uses a separable force¹ in the particle-hole channel making it possible to include all relevant single-particle states for describing collective excitation *i.e.* no effective charges are necessary to reproduce electromagnetic transition strengths. The golden horse of the QPM is the coupling of one-phonon states to two- and three-phonon states - a feature which is unique to the QPM. The next section describes technical aspects how the QPM tackles the nuclear many-body problem followed by a section about transition operators with a special focus on M1-transitions being important for MSS.

2.2.1 General formalism

The phenomenological hamiltonian used in QPM calculations contains four parts

$$\mathbf{H}_{\text{qpm}} = \mathbf{H}_{\text{sp}} + \mathbf{H}_{\text{pair}} + \mathbf{H}_{\text{m}} + \mathbf{H}_{\text{sm}}, \quad (2.32)$$

where:

- \mathbf{H}_{sp} is the single-particle hamiltonian usually taken as a Wood-Saxon potential,
- \mathbf{H}_{pair} absorbs the short range pairing correlations in the particle-particle channel,
- \mathbf{H}_{m} represents a separable multipole interaction in the particle-hole channel,
- \mathbf{H}_{sm} is a separable spin-multipole interaction in the particle-hole channel.

The QPM equations are obtained by a step-by-step diagonalization of the hamiltonian. In the following each of these steps is examined in detail and realistic examples are provided for the case of ⁹²Zr. The discussion is limited to even-even nuclei and natural parity states, therefore the last term \mathbf{H}_{sm} - being only important for unnatural parity states - is not considered here. Additional information can be found in Ref. [Sol92].

First an appropriate mean-field potential is chosen - separately for protons and neutrons - to account for parts of the long-range interaction. The common choice in case of the QPM is a Wood-Saxon potential of the form

$$U^\tau(r) = \frac{V_0^\tau}{1 + e^{(r-R_0^\tau)/a_0^\tau}} - \frac{\hbar^2}{\mu^2 c^2} \frac{1}{r} \frac{d}{dr} \left(\frac{V_{ls}^\tau}{1 + e^{(r-R_{ls}^\tau)/a_{ls}^\tau}} \mathbf{l} \cdot \mathbf{s} \right) + V_c(r). \quad (2.33)$$

V_c represents the coulomb potential and μ the reduced mass. All parameters are fitted to obtain a suitable description of the properties of nuclei in a given mass region with the restrictions $R_{ls}^\tau = R_0^\tau$, $a_{ls}^\tau = a_0^\tau$, and $R_c = R_0^p$. Of course this treatment reflects the phenomenology of the QPM approach, however in principle it would be possible to use a mean-field potential obtained in a self-consistent way using Hatree-Fock and Skyrme Forces [Sol92]. This thesis considers the nuclei ⁹²Zr and ⁹⁴Mo. The Wood-Saxon parameters used to calculate the properties of these nuclei are shown in Tab.2.1. In Fig. 2.3 is presented the resulting single particle

	V_0 (MeV)	R_0 (fm)	a_0 (fm)	V_{ls} (MeV)
neutrons	-44.70	5.802	0.6200	-9.231
protons	-56.70	5.577	0.6301	-9.609

Table 2.1: Parameters of the Woods-Saxon potential used to calculate the properties of ⁹²Zr and ⁹⁴Mo.

spectra for neutrons (a) and protons (b). To obtain the ground state configuration one simply fills in the available number of nucleons from the bottom to the top accounting for the pauli principle. At this stage the model is called independent shell model and can describe only some properties of magic nuclei. For giving a realistic description of nuclei the residual interaction codified in the last three terms of Eq. 2.32 has to be taken into account.

Monopole pairing is known to be by far the strongest residual interaction. This property of the nuclear force manifests in several fundamental experimental signatures like the 0^+ ground state in even-even nuclei, the odd-even mass staggering or the different level densities of even-even and even-odd (odd-odd) nuclei. The pairing force tends to couple like nucleons to spin-zero pairs causing nuclear superfluidity conceptually very similar to the superfluidity found in solid state physics. The main theoretical tool to account

¹ A separable force is defined as $\mathbf{V}(r_1, r_2) = \mathbf{V}(r_1)\mathbf{V}(r_2)$.

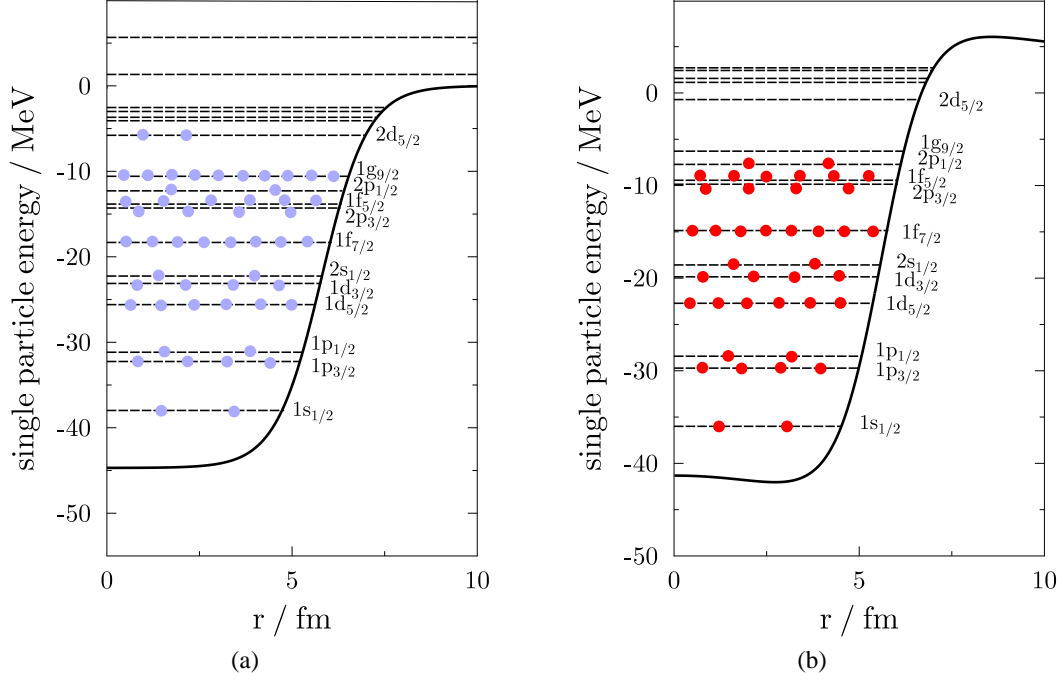


Figure 2.3: The single particle spectra for neutrons (a) and protons (b) calculated with the Woods-Saxon parameters in Tab. 2.1. The single particle energies are counted relative to the depth of the potential in Eq. 2.33 neglecting the second term.

for this effect is the BCS theory developed by Bardeen, Cooper and Schrieffer in 1957. As an ansatz for the nuclear ground state a wavefunction is chosen, which reflects the superfluid-character of nuclei

$$|BCS\rangle = \prod_{k>0} (u_k + v_k \mathbf{a}_k^+ \bar{\mathbf{a}}_k^+) |0\rangle, \quad (2.34)$$

where k runs over the whole single particle basis, $|0\rangle$ is the vacuum state and \bar{k} represents the time-reversed state of k , *i.e.* in a spherical basis $k = (n, j, l, m)$ and $\bar{k} = (n, j, l, -m)$. The square of the coefficients u_k and v_k can be interpreted as the probability that the state k is either empty or occupied by a nucleon pair. In QPM calculations pairing correlations are absorbed in the *second* term \mathbf{H}_{pair} of Eq.2.32

$$\mathbf{H}_{\text{pair}} = - \sum_{\tau}^{n,p} G_{\tau}^{(0)} \sum_{j,j'} \sqrt{(2j+1)(2j'+1)} [\mathbf{a}_{jm}^+ \mathbf{a}_{j-m}^+]_{00} [\mathbf{a}_{j'-m'}^+ \mathbf{a}_{j'm'}^+]_{00}, \quad (2.35)$$

where

$$[\mathbf{a}_j^+ \mathbf{a}_{j'}^+]_{\lambda\mu} = \sum_{m,m'} C_{jmj'm'}^{\lambda\mu} \mathbf{a}_{jm}^+ \mathbf{a}_{j'm'}^+. \quad (2.36)$$

$C_{jmj'm'}^{\lambda\mu}$ is the common Clebsch-Gordan coefficient. The structure of the pairing hamiltonian is very simple and assumes that monopole pairing is of zero-range and state-independent as indicated by the constant matrix element $G_{\tau}^{(0)}$. In principle the latter assumption is not fully justified and more refined treatments are recommended like using a density dependent pairing force [Sev08]. However the QPM is able to account for the main properties of spherical nuclei and therefore this treatment seems to be acceptable.

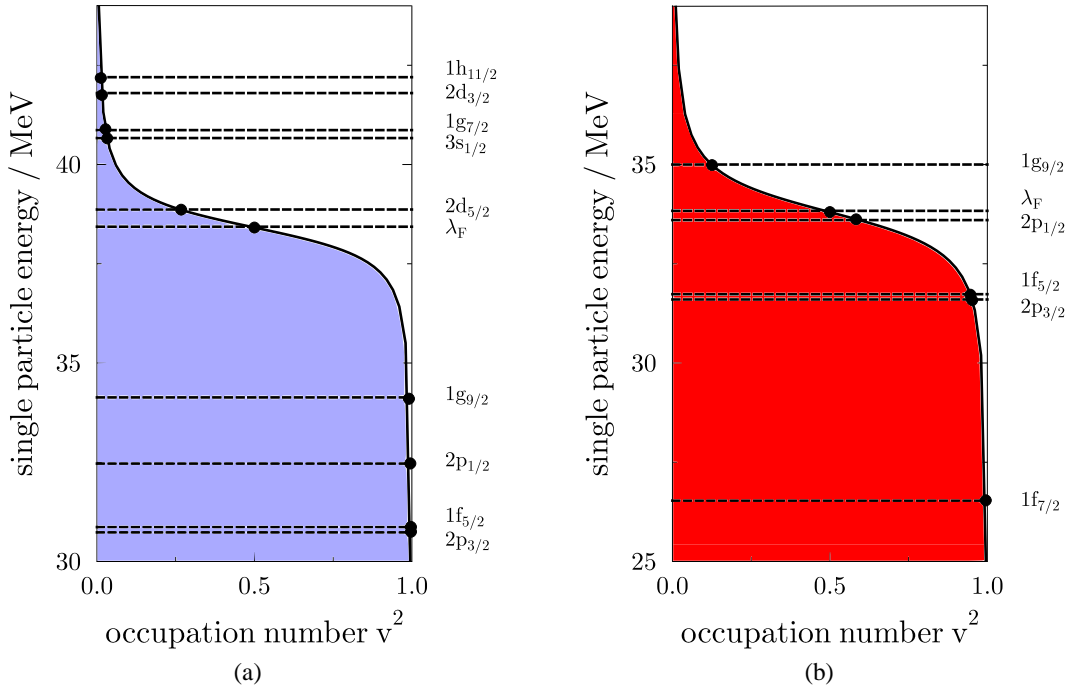


Figure 2.4: The BCS ground state for neutrons (a) and protons (b) calculated within the QPM for ^{92}Zr . The pairing force ensures a non-zero occupation probability of single-particle states above the fermi surface λ_F .

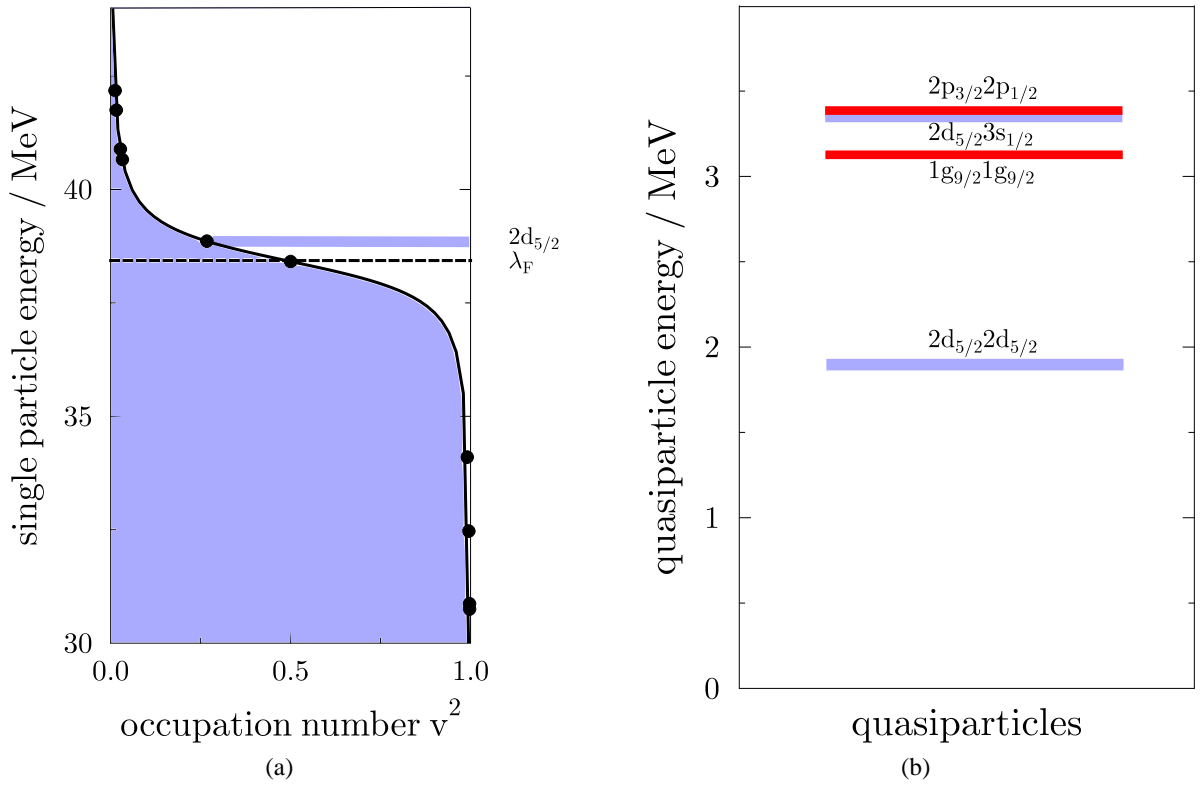


Figure 2.5: The probability density for a $(2d_{5/2} \otimes 2d_{5/2})$ two-quasiparticle state (a) and the four lowest two-quasiparticle states relative to the BCS ground state in ^{92}Zr (b) (blue for neutron and red for protons).

The ansatz for the BCS ground state exhibits the important caveat of having no distinct particle number. Of course this is a bad assumption for calculating the properties of finite nuclei. Therefore the variational principle - the common method to determine the coefficients u_k and v_k - has to be applied under the constraint that

$$\langle BCS | \mathbf{N} | BCS \rangle = N. \quad (2.37)$$

This can be easily implemented by using Lagrange multipliers. The corresponding equation for calculating the BCS-ground state reads

$$\delta \left\{ \langle BCS | \mathbf{H}_{sp} + \mathbf{H}_{pair} | BCS \rangle - \lambda \langle BCS | \mathbf{N} | BCS \rangle \right\} = 0, \quad (2.38)$$

λ is the chemical potential or fermi level *i.e.* the energy which is on average necessary to add an additional particle. The result of this minimization procedure are the well-known BCS equations which allow to determine the coefficients u_k and v_k . It is very useful to introduce so called quasiparticles via the Bogoliubov transformation

$$\begin{aligned} \alpha_k^+ &:= u_k \mathbf{a}_k^+ - v_k \mathbf{a}_{\bar{k}} \\ \alpha_{\bar{k}}^+ &:= u_k \mathbf{a}_{\bar{k}}^+ - v_k \mathbf{a}_k. \end{aligned} \quad (2.39)$$

This definition allows to rewrite the BCS ground state as

$$|BCS\rangle \sim \prod_{k>0} (\alpha_{\bar{k}} \alpha_k) |0\rangle. \quad (2.40)$$

On the one hand the BCS formalism allows to interpret pairwise interacting particles as *non-interacting quasiparticles* which is a highly efficient way to account for pairing correlations on the other hand the price one has to pay is the loss of the distinct particle number. In Fig. 2.4 is presented the BCS ground state of ^{92}Zr - neutrons (a) and protons (b) - calculated within the QPM. The non-zero occupation probabilities for single-particle levels above the fermi-surface λ highlights the important feature of the pairing force being able to scatter pairs of nucleons over different j-shells. Therefore the fermi-surface is dissolved in dependence of the pairing matrix element $G_\tau^{(0)}$. The pairing constants $G_n^{(0)}$ and $G_p^{(0)}$ are fitted to odd-even mass differences in the neighbouring nuclei.

Examining Eq.2.40 makes clear that the BCS ground state can be considered as the quasiparticle vacuum

$$\alpha_k |BCS\rangle = 0, \quad (2.41)$$

analogously as $|0\rangle$ is the vacuum of particles. Hence, in even-even nuclei two-quasiparticle excitations can be written as

$$|\phi\rangle = \alpha_{k_1}^+ \alpha_{k_2}^+ |BCS\rangle. \quad (2.42)$$

Similarly to the particle-hole excitation spectrum in the independent shell model one can introduce a quasiparticle excitation spectrum relative to the BCS-ground state with the pleasant feature that pairing correlations are already included. On the left-hand-side of Fig. 2.5 is shown the occupation probability for the $(2d_{5/2} \otimes 2d_{5/2})$ two-quasiparticle states and on the right-hand-side the four lowest two-quasiparticle excitations in ^{92}Zr . The quasiparticle energies can be calculated from the coefficients u_k and v_k with the equation

$$\epsilon_j = \sqrt{\Delta_\tau^2 + (E_j - \lambda_\tau)^2} \quad (2.43)$$

where E_j is the single-particle energy from the Wood-Saxon potential and Δ_τ is the so called pairing gap

$$\Delta_\tau = G_\tau^{(0)} \sum_j u_j v_j. \quad (2.44)$$

In the *third step* of the diagonalization procedure \mathbf{H}_m is included being responsible for the mixing of quasiparticle states. In the quasiparticle representation the hamiltonian of Eq. 2.32 can be written as

$$\mathbf{H}_{\text{qpm}} = \sum_{\tau} \sum_{\tau\rho} \sum_{j,m}^{\pm 1} \epsilon_j \alpha_{jm}^+ \alpha_{jm} + \sum_{\lambda\mu} \sum_{\tau\rho}^{\pm 1} (\kappa_0^{(\lambda)} + \rho \kappa_1^{(\lambda)}) \mathbf{M}_{\lambda\mu}^+(\tau) \mathbf{M}_{\lambda\mu}^+(\rho\tau), \quad (2.45)$$

where the multipole operator is given by

$$\mathbf{M}_{\lambda\mu}^+ = \sum_{jj'}^{\tau} \frac{f_{jj'}^{(\lambda)}}{\sqrt{2\lambda+1}} \left\{ \frac{u_{jj'}^{(+)}}{2} ([\alpha_j^+ \alpha_{j'}^+]_{\lambda\mu} + (-1)^{\lambda-\mu} [\alpha_j^+ \alpha_{j'}^+]_{\lambda-\mu}) - v_{jj'}^{(-)} \mathbf{B}_\tau(jj'; \lambda\mu) \right\}, \quad (2.46)$$

$$\mathbf{B}_\tau(jj'; \lambda\mu) = \sum_{mm'} (-1)^{j'-m'} C_{jm' m'}^{\lambda\mu} \alpha_{jm'}^+ \alpha_{j'm'}^+. \quad (2.47)$$

The reduced matrix element $f_{jj'}^\lambda = \langle j || i^\lambda f_\lambda^\tau(r) Y_\lambda(\Omega) || j' \rangle$ contains the radial dependence $f_\lambda^\tau(r)$ of the residual interaction. The following combination of Bogoliubov's coefficients are introduced $u_{jj'}^{(\pm)} = u_j v_{j'} \pm u_{j'} v_j$ and $v_{jj'}^{(\mp)} = u_j u_{j'} \mp v_j v_{j'}$. The QPM uses a separable interaction in the particle-hole channel. This assumption is an oversimplification of the nuclear force, but not as bad as it seems, *e.g.* in Ref. [Knu76] it was shown that more realistic matrix elements can be approximated to a reasonable extent with a separable force. The advantage in using a separable force is an enormous simplification concerning technical and numerical aspects when diagonalizing the hamiltonian of Eq. 2.45. Of course, the aim is to diagonalize the hamiltonian exact, because of the infinite dimension of the eigenvalue problem this is prohibited. In order to find a suitable truncation scheme, one can write the ground state or any other state in the following way

$$|\psi^v\rangle = C_0^v |BCS\rangle + \sum_{m,i} C_{mi}^v \alpha_m^+ \alpha_i^+ |BCS\rangle + \sum_{m,i,n,j} C_{mn,ij}^v \alpha_m^+ \alpha_n^+ \alpha_i^+ \alpha_j^+ |BCS\rangle + \dots \quad (2.48)$$

The first and the second term should contribute with the largest amplitudes from a perturbation theory viewpoint motivating the ansatz for a set of operators which project the groundstate on the excited states

$$\mathbf{Q}_{\lambda\mu i}^+ = \frac{1}{2} \sum_{\tau} \sum_{jj'}^{n,p} \{ \psi_{jj'}^{\lambda i} [\alpha_j^+ \alpha_{j'}^+]_{\lambda\mu} - (-1)^{\lambda-\mu} \phi_{jj'}^{\lambda\mu} [\alpha_j \alpha_{j'}']_{\lambda-\mu} \}. \quad (2.49)$$

This approach is called Quasiparticle Random-Phase Approximation (QRPA). From Eq. 2.49 one sees immediately that $\mathbf{Q}|BCS\rangle \neq 0$, so the simple BCS-vacuum is not equivalent to the QRPA-vacuum. Instead, four, eight, twelve etc. quasiparticle configurations are expected to appear in the QRPA-vacuum causing a so called 'correlated ground state'.

The QRPA equations for determining the coefficients $\psi_{jj'}^{\lambda i}$ (forward amplitude) and $\phi_{jj'}^{\lambda\mu}$ (backward amplitude) can be obtained in many ways. The most elegant one is the Equation of Motion method discussed in Ref. [Shu07]. An other one is to apply again the variation procedure

$$\delta \left\{ \langle \text{QRPA} | \mathbf{H}_{qpm} | \text{QRPA} \rangle - (\omega_{\lambda i} / 2) \left[\sum_{jj'} \{ (\psi_{jj'}^{\lambda i})^2 - (\phi_{jj'}^{\lambda\mu})^2 \} - 2 \right] \right\} = 0, \quad (2.50)$$

where $|\text{QRPA}\rangle$ is the QRPA-vacuum and $\omega_{\lambda i}$ the energy of the i -th phonon with multipolarity λ . The explicit equations can be found in most nuclear structure textbooks (*e.g.* Ref. [Shu07]). The forward and backward amplitudes fulfill the normalisation condition

$$\sum_{jj'} [\psi_{jj'}^{\lambda i} \psi_{jj'}^{\lambda i'} - \phi_{jj'}^{\lambda i} \phi_{jj'}^{\lambda i'}] = 2\delta_{ii'} \delta_{\lambda\lambda'}. \quad (2.51)$$

The amplitudes are normalised for some historical reasons to two. It is worth pointing out that the QRPA solutions contain collective - *e.g.* the $[2_1^+]_{RPA}$ and the $[3_1^-]_{RPA}$ - as well as non-collective solutions namely nearly pure two-quasiparticle excitations which are not included in the space of the IBM. To avoid misunderstandings it should be mentioned that in the QPM language every solution of the QRPA equations is called a phonon, in contrast to the geometrical model of Bohr-Mottelson or the IBM, where only collective excitations are referred to as phonons.

Diagonalizing the hamiltonian of Eq. 2.45 in the space of one-phonon states, given by the solutions of Eq. 2.50, yields

$$\mathbf{H} = \sum_{\lambda\mu i} \omega_{\lambda i} \mathbf{Q}_{\lambda\mu i}^+ \mathbf{Q}_{\lambda\mu i} + \mathbf{H}_{int}. \quad (2.52)$$

As indicated by the presence of \mathbf{H}_{int} , the QPM-hamiltonian is not completely diagonal in the space of the one-phonon states. The off-diagonal term \mathbf{H}_{int} is responsible for the crucial mixing between the different phonons. Its origin can be traced back to the presence of $\mathbf{B}_\tau(jj'; \lambda\mu)$ in Eq. 2.45. Therefore the most general wavefunction can be written as a mixture of one-, two-, three- etc. phonon states

$$\begin{aligned} \psi^i(J) = & \left\{ \sum_{\alpha_1} S_{\alpha_1}^i(J) \mathbf{Q}_{\alpha_1}^+ + \sum_{\alpha_2 \leq \beta_2} \frac{D_{\alpha_2 \beta_2}(J)}{\sqrt{1 + \delta_{\alpha_2 \beta_2}}} [\mathbf{Q}_{\alpha_2}^+, \mathbf{Q}_{\beta_2}^+]_J + \right. \\ & \left. + \sum_{\alpha_3 \leq \beta_3 \leq \gamma_3} \frac{\mathbf{T}_{\alpha_3 \beta_3 \gamma_3}^i(J)}{\sqrt{1 + \delta_{\alpha_3 \beta_3 \gamma_3}}} [\mathbf{Q}_{\alpha_3}^+, \mathbf{Q}_{\beta_3}^+, \mathbf{Q}_{\gamma_3}^+]_J + \dots \right\} |\text{QRPA}\rangle, \end{aligned} \quad (2.53)$$

where

$$\delta_{\alpha_3 \beta_3 \gamma_3} = \delta_{\alpha_3 \beta_3} + \delta_{\alpha_3 \gamma_3} + \delta_{\beta_3 \gamma_3} + 2\delta_{\alpha_3 \beta_3} \delta_{\alpha_3 \gamma_3}. \quad (2.54)$$

Most of the RPA and QRPA calculations include only one-phonon states since a coupling to two- and three-phonon states complicate the whole calculation drastically concerning numerical as well as technical aspects. However two- and three-phonon states are known

to have a pronounced influence on the properties of low-lying states. For example the 2_1^+ state in even-even nuclei is without two- and three-phonons states too high in energy, only after a coupling to more complex configurations it is pushed down in energy. Therefore in many calculations - which stay on the one-phonon level - a direct comparison to experiment is difficult. For the QPM the situation is different. Since it uses a separable force - which allows an enormous simplification of the calculation procedure - an inclusion of up to three-phonon states is possible and one can compare the results directly to experiment. In order to determine the coefficients S, D and T in Eq. 2.53 the resulting equations of the following minimization procedure are solved

$$\delta \left\{ \langle \psi^i(J) | \mathbf{H} | \psi^i(J) \rangle - E_i \langle \psi^i(J) | \psi^i(J) \rangle \right\} = 0. \quad (2.55)$$

Their explicit form is given in Ref. [Ber99]. It is worth pointing out that no additional parameters have been introduced to account for the phonon coupling. In the following two different types of calculations are presented which stop at different stages in the diagonalization procedure. The 'QPM results' contain all four steps, while the 'QRPA results' stop after the third step, *i.e.* the coupling to multiphonon states is not included.

2.2.2 Electromagnetic transition strengths and densities

Besides excitation energies electromagnetic decay properties are an excellent observable for testing model predictions and to deepen our understanding of nuclear structure, *e.g.* they can give important informations about collective phenomena signaled by large transition strengths. In the following the expressions for transitions being important for MSS are discussed. In the quasiparticle and phonon representation the electric transition operator transforms into

$$\begin{aligned} \mathcal{M}(E\lambda\mu) = \sum_{\tau}^{n,p} e_{\tau}^{(\lambda)} \sum_{jj'} \frac{\langle j || E\lambda || j' \rangle}{\sqrt{2\lambda+1}} \left\{ \frac{u_{jj'}^{(+)}}{2} \sum_i (\psi_{jj'}^{\lambda i} + \varphi_{jj'}^{\lambda i}) (\mathbf{Q}_{\lambda\mu}^+ + (-)^{\lambda-\mu} \mathbf{Q}_{\lambda-\mu}) \right. \\ \left. + v_{jj'}^{(-)} \sum_{mm'} C_{jmj'm'}^{\lambda\mu} (-)^{j'-m'} \alpha_{j'm'}^+ \alpha_{j'-m'} \right\} \end{aligned} \quad (2.56)$$

where the single-particle transition matrix element $\langle j || E\lambda || j' \rangle = \langle j || i^{\lambda} Y_{\lambda} r^{\lambda} || j' \rangle$. The first term corresponds to a one-phonon exchange term between the initial and final state, while the second one is a so called boson-forbidden transition, *i.e.* in a pure boson picture - neglecting the inner fermion structure of the Q-operators - this transition would be forbidden. The e_{τ} represents effective charges to account for states outside the chosen model space. In the shell model typical values are $e_n = 0.5$ and $e_p = 1.5$. Since the QPM uses a drastically larger model space containing all necessary states contributing to the transition of interest, it is possible to take the bare values $e_n = 0$ and $e_p = 1$. The explicit reduced matrix element for a ground state transition of a one-phonon state is

$$\langle Q_{\lambda i} || \mathcal{M}(E\lambda) || 0_{g.s.}^+ \rangle = \sum_{\tau}^{n,p} e_{\tau}^{(\lambda)} \sum_{jj'} \frac{u_{jj'}^{(+)}}{2} \langle j || E\lambda || j' \rangle (\psi_{jj'}^{\lambda i} + \varphi_{jj'}^{\lambda i}). \quad (2.57)$$

For the discussion of mixed-symmetry states magnetic transitions are of outmost importance. The M1-transition operator has a similar structure as Eq. 2.56 and contains a boson-forbidden part [Sol92]. This part allows M1-transition which are forbidden in the IBM-2. The expression for magnetic transitions with multipolarity λ_1 between two RPA-one-phonon states with multiplicities λ_3 and λ_2 is given by

$$\begin{aligned} \langle Q_{\lambda_3 i} || \mathcal{M}(E\lambda_1) || Q_{\lambda_2 i'} \rangle = \sum_{\tau}^{p,n} \sum_{j_1 j_2 j_3} v_{jj'}^{(+)} \cdot \langle j_1 || M\lambda_1 || j_2 \rangle \\ \cdot \begin{Bmatrix} \lambda_3 & \lambda_2 & \lambda_1 \\ j_1 & j_2 & j_3 \end{Bmatrix} (\psi_{j_2 j_3}^{\lambda_3} \psi_{j_3 j_1}^{\lambda_2} + \phi_{j_2 j_3}^{\lambda_3} \phi_{j_3 j_1}^{\lambda_2}). \end{aligned} \quad (2.58)$$

In addition to absolute electromagnetic transition strengths, transition densities constitute an excellent observable to give detailed information about the nature of nuclear wavefunctions. If one restricts to the one-phonon part of the wavefunction the transition density can be written as

$$\rho_v(r) = \sum_i S_i^v(J) \rho_i^J(r) \quad (2.59)$$

with

$$\rho_i^J(r) = \sum_{jj'}^{N,Z} \frac{u_{jj'}^{(+)}}{2} \rho_{jj'}^J(r) \cdot (\psi_{jj'}^{Ji} + \varphi_{jj'}^{Ji}). \quad (2.60)$$

The two-quasiparticle transition densities $\rho_{jj'}^J$ can be written as

$$\rho_{jj'}^J(r) = (-1)^{j-\frac{1}{2}} i^{l'-l-J} \frac{\hat{j}\hat{j}'}{4\hat{J}\sqrt{\pi}} (1 + (-1)^{l+l'+J}) \left\langle j \frac{1}{2} j' \frac{-1}{2} \middle| J 0 \right\rangle p_j^*(r) p_{j'}(r), \quad (2.61)$$

p_j stands for the radial part of the single-particle wavefunction obtained from the Woods-Saxon potential of Eq. 2.33. Each two-quasiparticle transition density has its own specific radial dependence. The different radial behaviour is the basic requirement for the new signature for MSS presented in section 5.2.

3 The Experiment

The electron and proton scattering experiments were performed at the linear accelerator S-DALINAC in Darmstadt and at the iThemba LABS cyclotron located in Somerset West, South Africa, respectively. The experimental setups and data taking conditions are described in this chapter.

3.1 Electron scattering at the S-DALINAC

This section gives an outline of the S-DALINAC, the electron scattering setup at the spectrometer and the detector system on the focal plane.

3.1.1 The S-DALINAC

The first European superconducting electron linear accelerator S-DALINAC delivers high-quality electron beams since 1991. It covers the low-energy range between 2.5 and 130 MeV with currents up to $40 \mu\text{A}$ used in a variety of experiments. A schematic layout of the S-DALINAC is shown in Fig. 3.1. The electrons are emitted by a thermionic gun and accelerated electrostatically

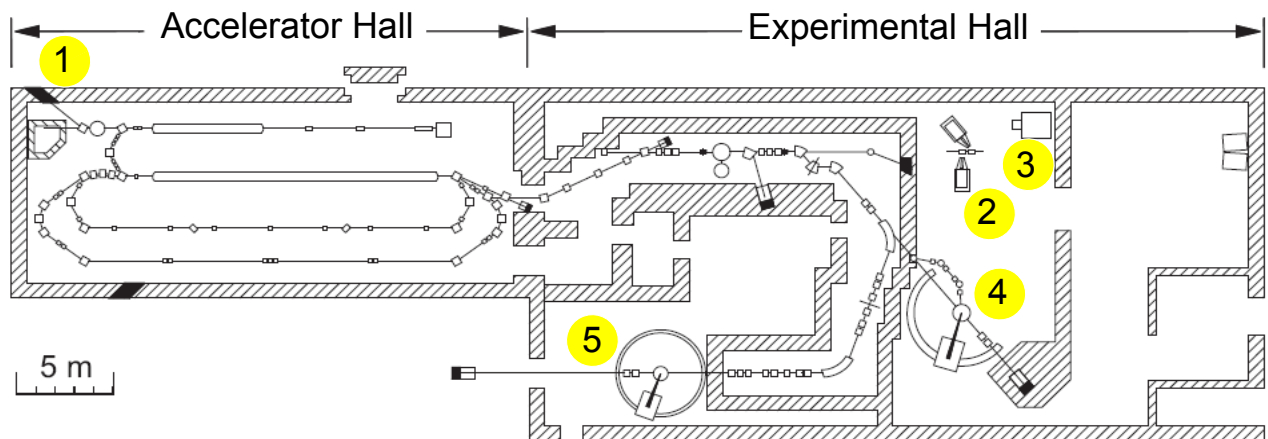


Figure 3.1: Floor plan of the S-DALINAC with its experimental setups: HIPS ①, polarizability of the nucleon ②, low energy tagger NEPTUN ③, QCLAM spectrometer ④ and Lintott spectrometer ⑤.

to an energy of 250 keV. A chopper/prebuncher system operating at room temperature generates electron bunches. Afterwards the bunches enter the superconducting injector linac consisting of several niobium cavities cooled to 2 K. The electrons are accelerated in the injector up to 10 MeV at maximum and can be directly used at the High Intensity Photon Setup (HIPS) [Moh99] for nuclear resonance fluorescence or photoactivation experiments ①. Alternatively, the beam can be injected in the main superconducting linear accelerator which provides an energy gain of up to 40 MeV. Either the electrons are extracted right away to the various experiments or - if a higher energy is needed - they can be recirculated once or twice providing a maximum energy of 130 MeV.

In the experimental hall on the right hand side of Fig. 3.1, a wide range of nuclear physics questions can be addressed by various experimental setups. The electron beam can be converted into bremsstrahlung photons and used for studying the polarizability of the nucleon ② [Yev10] or for (γ, γ') experiments at the low-energy photon tagger NEPTUN ③ [Sav10]. Two spectrometers are available for electron scattering experiments. The QCLAM spectrometer ④ [Lüt95] offers the possibility to investigate nuclear current distributions at a scattering angle of 180° . For the electron scattering experiments performed in this thesis, the Lintott spectrometer ⑤ [Wal78] was used. In contrast to the QCLAM the Lintott offers the possibility to work in the energy-loss mode resulting in a high energy resolution.

3.1.2 High-resolution electron scattering facility

The Lintott spectrometer is used for high-resolution electron scattering experiments. Figure 3.2 presents a schematic picture. The electron beam enters from the left and hits the target placed at the Pivot point ① of the spectrometer. The scattered electrons enter the dipole magnet of the spectrometer ② where they are momentum analyzed and finally hit the focal plane ③ with a position sensitive detector system. The electrons at the central trajectory are deflected by 169.7° - the so called magic angle - which

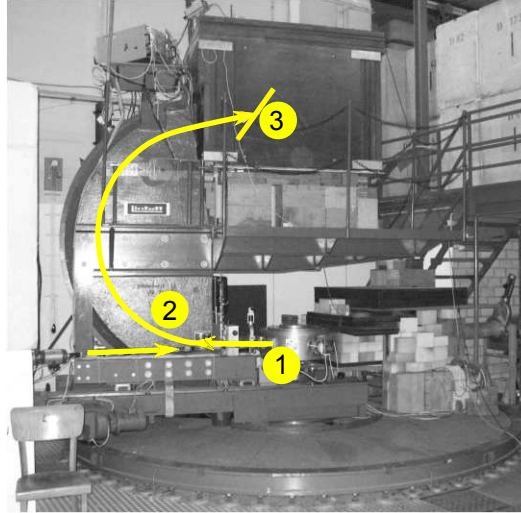


Figure 3.2: The Lintott spectrometer at the S-DALINAC. The yellow lines mark the incoming and scattered electrons. The target is placed at the pivot point ① of the spectrometer. The scattered electrons are momentum analyzed in the spectrometer magnet ②. At the focal plane ③ is placed a position sensitive detector system.

was chosen to improve the ion-optical properties of the spectrometer. The solid angle acceptance is relatively small with 6 msr. The Lintott provides a high energy resolution up to $\Delta E/E = 1.5 \cdot 10^{-4}$. Some important parameters of the Lintott spectrometer are summarized in Tab. 3.1.

Electron energy range	20 - 120 MeV
Momentum acceptance	$\pm 2.1\%$
Energy resolution	$1.5 \cdot 10^{-4}$
Angular range	$33^\circ - 165^\circ$
Angle step	12°
solid angle acceptance	6 msr

Table 3.1: Main parameters of the Lintott spectrometer.

The energy resolution in experiments with charged particles is limited by the beam energy spread which amounts typically to $\Delta E/E = 10^{-3}$, *i.e.* for the Lintott spectrometer this factor is one order of magnitude larger than the intrinsic energy resolution. The so called energy loss mode allows to perform scattering experiments independently of the beam energy spread. The elements of the beam line are used to project the beam as an extended spot on the target with a size corresponding to the beam energy spread ΔE . The electrons leaving the target enter the spectrometer at slightly different positions and under slightly different angles causing a variation of trajectories inside spectrometer magnet. If the properties of the beam line elements are matched with the ion optical properties of the spectrometer, all electrons exciting the target nuclei in the same energy state can be focused at the same point on the focal plane making the energy resolution independent of the beam energy spread.

A picture of the focal plane detector system is shown in Fig. 3.3. It is based on a modern silicon micro strip detector unit and fast readout electronics allowing a high spatial resolution and high count rates [Len06]. The focal plane - having a length of 24 cm - is too large for one single micro strip detector. Therefore four micro strip detectors are mounted together covering the full focal plane. Each consists of 96 strips with a thickness of $500 \mu\text{m}$ and a pitch of $650 \mu\text{m}$. The gaps between them are responsible for the blind regions seen in the electron scattering spectra (see section 5.2). If necessary the gaps can be filled by changing slightly the magnetic field strength of the spectrometer magnet.

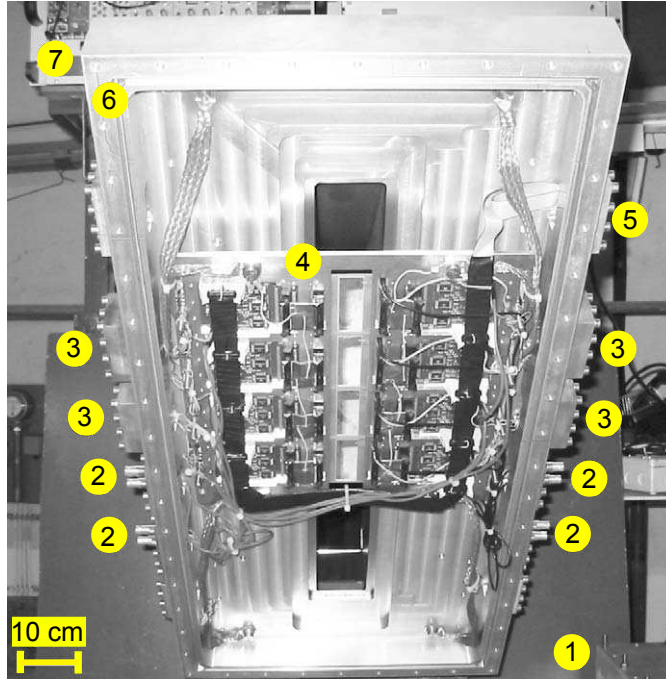


Figure 3.3: The detector system on the focal plane of the Lintott spectrometer consists of the following elements: Magnetic spectrometer iron yoke ①, vacuum connections of bias signals to the preamplifiers ②, vacuum connections of the preamplifiers analog signals ③, detector unit ④, vacuum connections of supply voltages and control signals of preamplifiers ⑤, detector case ⑥ and readout electronics and HV main adaptor ⑦ (slightly modified from Ref. [Len06]).

3.2 Proton scattering at iThemba LABS

The proton scattering experiments were carried out at the cyclotron of iThemba LABS in South Africa. The facility and the experimental setup are outlined in this section.

3.2.1 iThemba LABS

A floorplan of the iThemba LABS is presented in Fig. 3.4. The facility covers a wide range of applications like proton ⑥ and neutron therapy ⑦, radioactive isotope production ⑤, γ - spectroscopy ⑩ and the high-resolution K600 spectrometer ⑪ which was used for the proton scattering experiments described in this thesis. The particles are initially accelerated using one of the two solid-pole injector cyclotrons (SPC). The first one ② is used for the acceleration of light-ions, while the second one ③ is mainly used for heavy ions and polarized protons. The heart of the facility is a separated-sector cyclotron ④ which consists of four sectors, each with an angle of 34° where the particles from the injectors are further accelerated up to the required energy. The maximum energy achievable for protons is 200 MeV.

3.2.2 K600 spectrometer

A schematic picture of the light-ion spectrometer K600 used in the proton scattering experiments is shown Fig. 3.5. The protons from the separated sector cyclotron enter the scattering chamber and hit the target at ①. The beam is stopped in a corresponding Faraday cup. A set of collimators ③ define the solid angle which amounts to 6 msr at maximum. The scattered protons pass a sextupole magnet ④ and a quadrupole magnet ⑤ used for focusing the beam vertically. Afterwards the protons enter the first ⑥ and the second dipole magnet ⑦ where they are momentum analyzed and finally focused on the focal plane. The detector system on the focal plane consists of two horizontal and one vertical multiwire drift chamber ⑧ for event reconstruction. Additional plastic scintillators ⑨ located behind the focal plane are used as a trigger and for particle identification. The energy resolution achieved for protons amounts to $\Delta E/E \approx 1 \cdot 10^{-4}$. As in the case of electron scattering the energy resolution is independent of the beam energy spread due to the energy-loss mode.

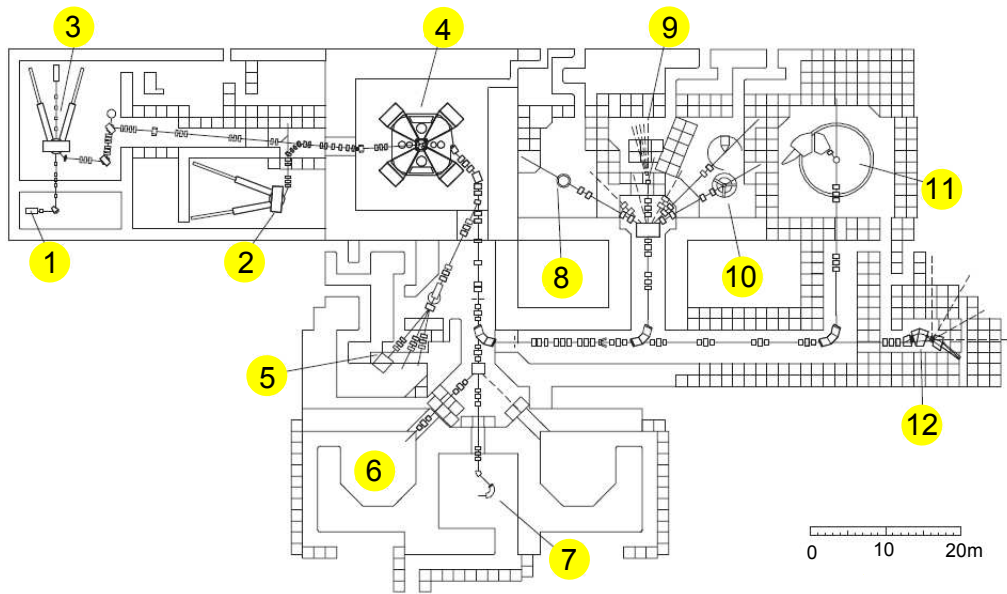


Figure 3.4: Floor plan of the iThemba LABS facility in South Africa with its main experimental setups: Ion source ①, SPC1 injector cyclotron ②, SPC2 injector cyclotron ③, separated-sector cyclotron ④, radioactive isotope production ⑤, proton therapy ⑥, neutron therapy ⑦, experiments with charged particles ⑧, experiments with neutron beams ⑨, γ -spectroscopy ⑩, K600 spectrometer ⑪ and beam swinger magnet ⑫ (slightly modified from Ref. [New96]).

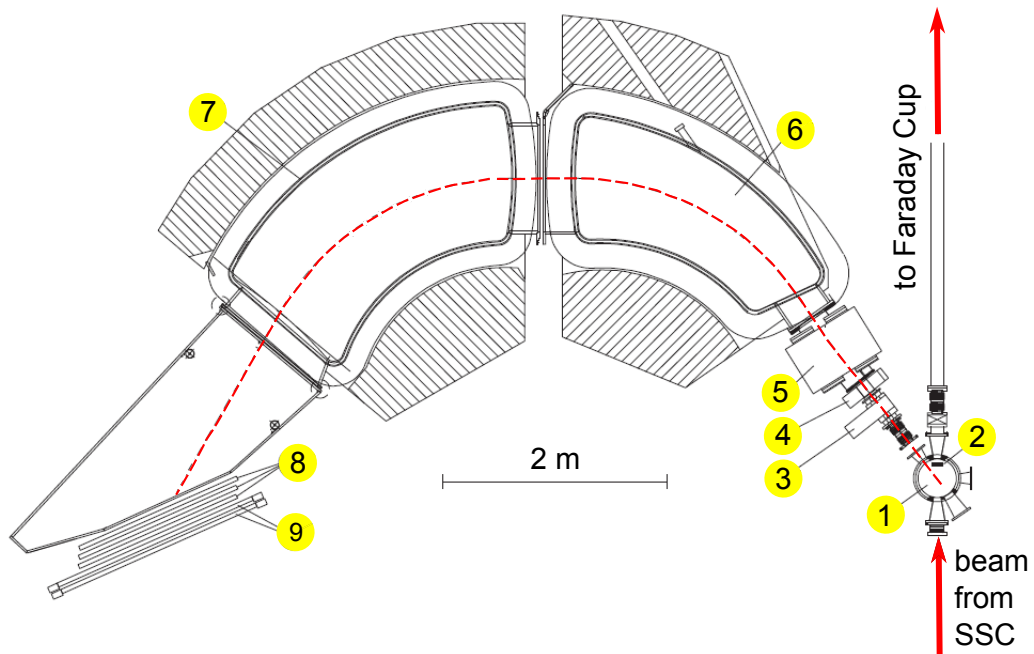


Figure 3.5: The K600 spectrometer at iThemba LABS: Scattering chamber ①, internal Faraday cup for small-angle scattering experiments ②, set of collimators ③, sextupole magnet ④, quadrupole magnet ⑤, first dipole magnet ⑥, second dipole magnet ⑦, two horizontal and one vertical drift chamber ⑧ and two plastic scintillators ⑨ (slightly modified from Ref. [New96]).

4 Data analysis and results

This chapter describes the data analysis and results for the proton and electron scattering experiments discussed in this master thesis. The first part examines the proton scattering experiments at ^{92}Zr and ^{94}Mo . Both experiments were carried out at the iThemba LABS facility located in South Africa using the high-resolution K600 spectrometer. The second part describes the electron scattering experiment at ^{92}Zr which was performed at the S-DALINAC using the Lintott Spectrometer. The investigations and conclusions of the following chapters are based on the results obtained in this chapter. In addition electron scattering data on ^{94}Mo described in Ref. [Kuh05] are reanalyzed.

4.1 Proton scattering

This section is organized as follows. First the data taking conditions are described concerning target properties, scattering angles, achieved energy resolutions and measured spectra. Next the procedure how to extract the cross sections and error estimates are discussed. Subsequently the DWBA analysis performed to assign spin and parity quantum numbers to excited states is outlined. Finally, the results for the proton scattering experiments at ^{92}Zr and ^{94}Mo are presented and compared to the results of Refs. [Sin09, Fra05]. The properties of important transitions are discussed and the isoscalar B(E2)- and B(E4)-strengths distributions are compared to QPM predictions.

4.1.1 Data taking conditions

The experiments were carried out at the cyclotron of iThemba LABS using the K600 spectrometer. Both measurements were performed during the same beam time in 2005 under identical kinematical conditions, *i.e.* the maximum available beam energy of $E_p = 200$ was chosen and the spectrometer angles were varied between 4° and 26° . In total 14 spectra were measured for ^{94}Mo and 12 for ^{92}Zr . Due to the energy loss mode - which is available at the K600 spectrometer - the energy resolution amounts to $\Delta E \approx 35$ keV. Typically the beam currents varied between 1 and $30 \mu\text{A}$ depending on the scattering angle. For the ^{94}Mo experiment a self-supporting foil enriched to 93.9% and 1.2 mg/cm^2 areal density have been used. The ^{92}Zr target was also self-supporting with an enrichment of 93.4 % and an areal density of 1.3 mg/cm^2 . In both nuclei the maximum excitation energy in the analysis was ~ 4 MeV. At energies above 4 MeV the level density is too high to resolve the excited states unambiguously. Table 4.1 summarizes the main experimental parameters of both reactions.

	^{92}Zr	^{94}Mo
areal density of the target	1.3 mg/cm^2	1.2 mg/cm^2
enrichment of the target	93.4 %	93.9%
energy resolution	$\sim 35 \text{ keV}$	$\sim 35 \text{ keV}$
beam energy	200 MeV	200 MeV
beam currents	1 - $30 \mu\text{A}$	1 - $30 \mu\text{A}$
measured spectra	14	12
evaluated energy range	0 - 4 MeV	0 - 4 MeV

Table 4.1: The main parameters of the $^{92}\text{Zr}(p,p')$ - and the $^{94}\text{Mo}(p,p')$ -experiments.

Figure 4.1 displays four representative spectra for the $^{92}\text{Zr}(p,p')$ - (upper part) and $^{94}\text{Mo}(p,p')$ -reactions (lower part). Important transition are marked with an arrow. The elastic lines are scaled down with the corresponding factors given in the figures for illustration purposes.

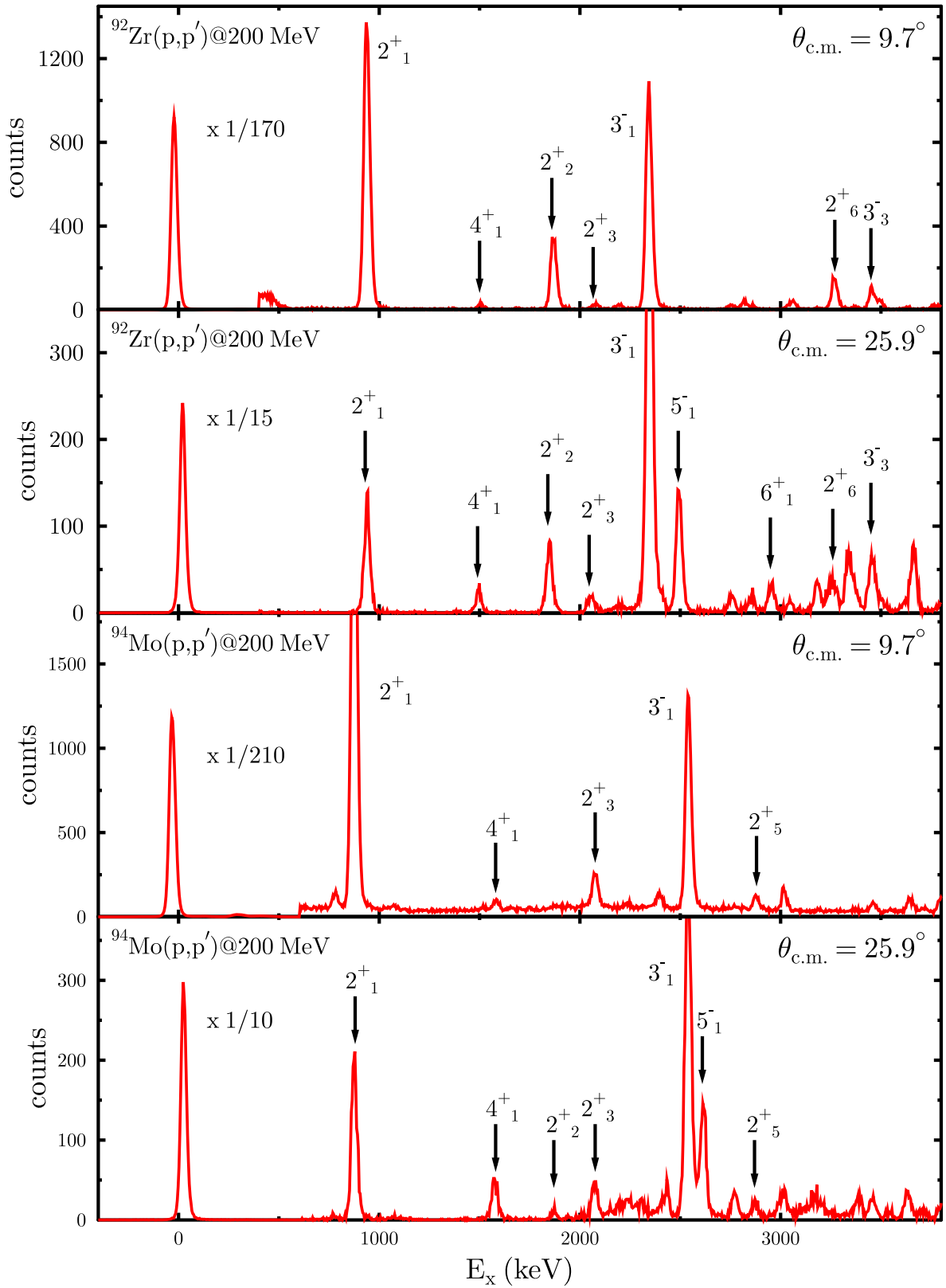


Figure 4.1: Representative spectra of the $^{92}\text{Zr}(p,p')$ and $^{94}\text{Mo}(p,p')$ reactions measured at 200 MeV. Prominent transitions are labeled with their spin and parity quantum numbers. The elastic transitions are scaled with the corresponding factors given in the figures.

4.1.2 Determination of the cross sections and energy calibration

The absolute center-of-mass (c.m.) differential cross section of the state of interest was calculated using the formula

$$\frac{d\sigma}{d\Omega}(\theta_{c.m.}) = \frac{J \cdot A_{exp} \cdot \cos(\theta/2)}{N_p \cdot \Delta\Omega \cdot n_t \cdot \epsilon}, \quad (4.1)$$

where

- J is the Jacobian to transform the differential cross sections from the laboratory to the center-of-mass system,
- A_{exp} is the peak area of the state of interest,
- n_t is the number of ^{92}Zr or ^{94}Mo target nuclei per unit volume,
- $\cos(\theta/2)$ is a factor to correct the target thickness to an effective one, where θ is the angle relative to the beam
- N_p is the total number of protons incident on the target,
- ϵ is the efficiency of the drift chambers (see Fig. 3.5),
- $\Delta\Omega$ is the solid angle covered by the entrance collimator to the spectrometer.

In the following some remarks are made to the various quantities. The peak areas A_{exp} are obtained by fitting the spectra with the peak fitting software SFit [Fuji]. The physical background from hydrogen contaminations in the target was estimated by an empirical smooth function. The line shape was taken to be identical to the elastic peak shapes in each spectrum. For each peak only the height and the position of the centroid were treated as free parameters.

The number of target nuclei was calculated using the equation

$$n_t = \frac{t \cdot \rho \cdot N_A \cdot \epsilon_d}{M}, \quad (4.2)$$

where t is the thickness of the target, ρ is the bulk density of the target, N_A is Avogadro's constant, ϵ_d the isotopic enrichment and M is the atomic mass of the target nuclei of interest. In the present experiment the target was placed in the so-called transition geometry, *i.e.* the protons pass always the same effective path length t_{eff} in the target which is given by

$$t_{eff} = t / \cos(\theta/2). \quad (4.3)$$

The cross section were corrected for the detection efficiencies ϵ of the multiwire drift chambers and for the dead time of the electronics. Typically, the total detection efficiency amounts to 85%. The solid angle covered by the collimator was determined to be 1.166 msr.

Since no reference measurements are available for energy calibration in both nuclei, prominent and well known transitions were used to calibrate the spectra. Due to the results of the $(n,n'\gamma)$ -reaction states with well known energy, spin and parity quantum numbers are available which can be used for the calibration up to 3.5 MeV. Hence, the missing reference measurements are not a serious caveat and a meaningful energy calibration can be performed up to ~ 4 MeV.

4.1.3 Error estimate

The measured (p,p') cross sections contain statistical as well as systematical errors. The total uncertainty of measured cross sections includes:

- statistical uncertainties in the peak area determination 3-10%
- uncertainties in the determination of the solid angle $\sim 1\%$
- statistical uncertainties in the determination of the accumulated charge in the Faraday cup $\sim 1\%$
- error in dead-time corrections $\sim 1\%$

The errors were treated as independent from each other and taken to be the square root of the sum of the squared systematic and statistical errors.

4.1.4 DWBA analysis

In order to assign spin and parity quantum numbers to the excited states, a DWBA analysis was performed in the framework of this thesis using the coupled-channel program CHUCK3 [Kunz]. The distorted waves in the entrance and exit channels were generated by solving the Schrödinger equation with the optical potential

$$U(r) = V_c(r) - Vf_v(r, R_v, a_v) + V_{ls} \left(\frac{\hbar}{m_\pi c} \right)^2 (\mathbf{I} \cdot \mathbf{s}) \frac{1}{r} \frac{d}{dr} f_{ls}(r, R_{ls}, a_{ls}) + i \left(Vf_v(r, R_v, a_v) - V_{ls} \left(\frac{\hbar}{m_\pi c} \right)^2 (\mathbf{I} \cdot \mathbf{s}) \frac{1}{r} \frac{d}{dr} f_{ls}(r, R_{ls}, a_{ls}) \right), \quad (4.4)$$

considering Coulomb, central volume, imaginary volume, spin-orbit and imaginary spin-orbit potentials. The nuclear potential form factors are chosen to have a Wood-Saxon type given by

$$f_k = \left(1 + \exp\left(\frac{r - R_k}{a_k}\right) \right)^{-1}, \quad (4.5)$$

with radius $R_k = r_k A^{1/3}$ and diffuseness a_k . The Coulomb potential was taken to be of standard form

$$V_c(r) = \begin{cases} \frac{Z_p Z_t (3 - (r/R_c)^2)}{2R_c} & , \quad r < R_c \\ \frac{Z_p Z_t}{r} & , \quad r > R_c \end{cases} \quad (4.6)$$

where Z_p is the charge of the projectile, Z_t is the charge of the target and R_c is the Coulomb radius. The optical potential parameters are displayed in Tab. 4.2 for ^{92}Zr . For ^{94}Mo a slight modification of the parameters was necessary. The parameters were fitted to the elastic cross sections starting from the set of Ref. [Sch82]. The transition potential was taken to be the derivative of the optical

	Woods-Saxon potential			LS potential		
	V (MeV)	r (fm)	a (fm)	V (MeV)	r (fm)	a (fm)
Re	17.520	1.257	0.750	-2.484	1.021	0.787
Im	-10.980	1.253	0.822	1.853	1.020	0.592

Table 4.2: The parameters of the optical potential used for ^{92}Zr .

potential weighted with a spin dependent factor r^{J+2} , *i.e.* for a given spin the calculated angular distributions have the same shapes regardless of the microscopic structures of the considered states.

The angular distributions of the cross sections are used to assign spin and parity quantum numbers to the excited states. The requirement for an unambiguous spin-parity assignment in the present work were: Agreement between theory and experiment over the complete measured angular range. The requirement for a tentative spin-parity assignment was: The position of the first maxima between theory and experiment are in agreement. Otherwise no quantum numbers are assigned. At 200 MeV the protons interact mainly isoscalar [Fra85] with the target nuclei and excite natural-parity states ¹, *i.e.* from the spin quantum number follows directly the parity quantum number. It would be possible to extract an isoscalar transition strength for each state from the quantity

$$\beta_L^2 = \left(\frac{d\sigma}{d\Omega} \right)_L^{exp} / \left(\frac{d\sigma}{d\Omega} \right)_L^{DWBA} \quad (4.7)$$

and compare it to predictions of the QPM. In this thesis a more fundamental way was chosen to compare QPM results to the data which is described in section 4.1.7.

For most of the states the one-step cross section of the collective model is sufficient and the experimental cross sections are reasonably well described. The comparison between theory and the experimental data is shown in Fig. 4.2 and Fig. 4.3 for ^{92}Zr and in Fig. 4.4 and Fig. 4.5 for ^{94}Mo .

However, there are two exceptions. For the symmetric quadrupole two-phonon states in ^{92}Zr and ^{94}Mo the description by a pure one-step excitation fails, due to large two-phonon components in the wave functions. For all other states two-step processes can be neglected. This is especially the case for the 2_5^+ in ^{94}Mo which is claimed to have a cross section shape pointing to a two-phonon nature in Ref. [Bur07]. However, the deviations from a one-step cross section shape at higher scattering angles are due to the excitation of the 6_2^+ (2872.4 keV) which is close in energy to the 2_5^+ (2870.0 keV). The 6^+ cross section has its first

¹ Natural-parity states are defined as states its spin and parity are connected by the relation $\pi = (-1)^J$.

maximum approximately at the first minimum of the 2^+ cross section. Therefore, the enhancement of the 2_5^+ cross section seen at larger scattering angles can not be attributed to the two-phonon nature of this state. Indeed at smaller scattering angles - where the 6_2^+ should contribute only weakly to the total cross section - a pure one-step cross section achieves a good description. This is in agreement with the results of Ref. [Bur75]. Two-step processes will play only a role for nearly pure two-phonon states like for the 2_2^+ in ^{94}Mo and the 2_3^+ in ^{92}Zr .

The second exception is the mixed-symmetry state in ^{94}Mo (and to a smaller extend the MSS in ^{92}Zr). Due to its isovector character the cross section shape differs significantly from collective model predictions. In order to describe these states, a microscopic treatment is needed. This is the main topics of this master thesis and will be discussed in chapter 5.

In the following sections the results of the coupled-channels analysis is discussed for ^{92}Zr and ^{94}Mo . In total 19 unambiguously and 2 tentative spin-parity assignments could be made for ^{92}Zr . For 3 states no spin could be assigned. For ^{94}Mo 17 angular distributions of cross sections could be measured with 13 unambiguously and 2 tentative assignments. Each of the angular distributions is shown and all transitions are discussed. It should be mentioned that - expect for some states in ^{94}Mo - no new spectroscopic information could be obtained from the present proton scattering experiments. Both nuclei are already measured in other hadron and $(n,n'\gamma)$ reactions with better energy resolutions. The aim of this work is not to obtain new spectroscopic informations but to use the data for new insights in the properties of mixed-symmetry states. This will be discussed in the following chapters.

Tables 4.3 and 4.4 display the observed excited states and the assigned quantum numbers for ^{92}Zr and ^{94}Mo , respectively. In Figs. 4.2-4.5 the experimental cross sections are compared to collective model predictions. Each transition is discussed in detail.

4.1.5 Proton scattering results for ^{92}Zr

No	E_x (keV) ¹	E_x (keV) ²	E_x (keV) ³	J^π	J^π	J^π	$(d\sigma/d\Omega)_{max}$ (mb/sr) ¹	$B(EL)_{IS}$ (s.p.u.) ²
1	937(1)	935	934.5(1)	2 ⁺	2 ⁺	2 ⁺	7.59	15.5
2	1496(3)	1495	1495.5(1)	4 ⁺	4 ⁺	4 ⁺	0.48	6.6
3	1849(1)	1847	1847.3(1)	2 ⁺	2 ⁺	2 ⁺	1.91	2.4
4	2062(2)	2053	2066.6(1)	2 ⁺	2 ⁺	2 ⁺		1.0
5	2187(3)	2182	2186.3(1)	2 ⁺	(2 ⁺)	2 ⁺		
6	2339(1)	2334	2339.6(1)	3 ⁻	3 ⁻	3 ⁻	9.41	35.2
7	2394(4)	2393	2398.4(1)	4 ⁺	4 ⁺	4 ⁺	0.47	1.7
8	2490(3)	2482	2485.9(2)	5 ⁻	5 ⁻	5 ⁻	0.42	10.0
9	2749(2)	2757	2747.9(2)	3 ⁻	3 ⁻	3 ⁻		
10	2814(4)	2823	2819.6(1)	2 ⁺	2 ⁺	2 ⁺	0.23	0.5
11	2859(3)	2869	2864.7(2)	4 ⁺	4 ⁺	4 ⁺	0.32	4.3
12	2948(5)	2963	2957.7(5)	6 ⁺	(6 ⁺)	6 ⁺	0.07	4.0
13	3047(3)	3055	3057.5(3)	2 ⁺	2 ⁺	2 ⁺	0.24	0.7
14	3181(2)	3187	3178.3(2)	(4 ⁺)	4 ⁺	4 ⁺	0.20	2.3
15	3236(4)	3248	3236.9(6)	(4 ⁺)	4 ⁺	4 ⁺	0.16	1.9
16	3264(2)	3273	3262.9(4)	2 ⁺	2 ⁺	2 ⁺	0.85	0.8
17	3329(3)	3345		5 ⁻	5 ⁻		0.21	4.0
18	3366(5)	3382			3 ⁻			
19	3450(1)	3452	3452.2(1)	3 ⁻	3 ⁻	(2 ⁺)	1.08	5.0
20	3494(3)	3491	3500.1(3)	2 ⁺	(3 ⁻)	2 ⁺	0.23	
21	3603(4)	3587						
22	3643(3)	3634						
23	4184(3)	4181		3 ⁻	3 ⁻		0.28	0.9
24	4410(5)	4397		2 ⁺	2 ⁺		0.38	0.3

¹ this work

² Ref. [Sin09]

³ Ref. [Fra05] and NNDC

Table 4.3: Results of the DWBA analysis $^{92}\text{Zr}(p,p')$ experiment. The energy, spin and parity quantum numbers are compared to the results of Ref. [Sin09] and Ref. [Fra05]. The excitation energies of Ref. [Sin09] are accurate within 10 keV at ~ 2 MeV and 20 keV at ~ 4 MeV. The quantity $(d\sigma/d\Omega)_{max}$ is the cross section at the first maximum of the corresponding state. The states at 2187 keV and 2749 keV belong to ^{90}Zr .

The 2⁺ states at 935, 1853, 2814 and 3264 keV

The cross sections are described well by the collective model predictions assuming a spin of 2 and a positive parity. This is in agreement with the results of Refs. [Sin09, Fra05].

The 2⁺ state at 2062 keV

Due to the two-phonon character of this state, its cross section can not be described by one-step processes alone.

The 2⁺ state at 2187 keV

Due to a remaining abundance of ⁹⁰Zr in the target, this is the first excited 2⁺ in ⁹⁰Zr located at 2196.3 keV. Only collective states like the first 2⁺ and first 3⁻ can be seen in the spectra. Contributions from other Zr isotopes than ⁹⁰Zr can be neglected.

The 2⁺/3⁻ doublet at 3047 keV

The observed transition is a doublet of the 2⁺ state at 3057.5 keV and the 3⁻ state at 3039.8 keV which cannot be resolved. This explains the deviations in the excitation energy compared to Ref. [Fra05] and the deviations of theory and experiment at larger scattering angles. The cross section is described best by assuming a spin of 2 and a positive parity. Therefore the 3⁻ state is much weaker excited.

The 2⁺ state at 3494 keV

The angular distribution is described best by assuming 2⁺ as quantum numbers. The state can be identified with the 2⁺ state of Ref. [Fra05] at 3500.1 keV. In contrast to this result Ref. [Sin09] made a tentative assignment of (3⁻).

The 2⁺ state at 4410 keV

The angular distribution for a 2⁺ states fits best in agreement with Ref. [Sin09]. The excitation energy is out-of-range of the (n,n' γ) data.

The 3⁻ states at 2339, 3450 and 4184 keV

Assuming quantum numbers 3⁻ gives the best fit to all three states. This is in agreement with [Sin09]. The (n,n' γ)-reaction of Ref. [Fra05] assigns 3⁻ for the state at 2339 keV, a tentative assignment of (2⁺) for the state seen at 3452.2 keV. The third state is out-of-range of this experiment.

The 3⁻ state at 2749 keV

Like the 2⁺ state at 2187 keV this 3⁻ state belongs to ⁹⁰Zr being located at 2747.9 keV.

The 4⁺ states at 1496, 2394 and 2859 keV

The cross sections are described well assuming spin and parity 4⁺ which is in agreement with Refs. [Sin09, Fra05]. The state at 2394 keV forms a doublet with the 3⁻ state at 2339 keV which could be resolved.

The tentative 4⁺ states at 3180 and 3236 keV

Only the position of the maxima correspond to the theoretical predictions for the angular distribution of a 4⁺ state. Serious deviations can be found at larger scattering angles which are not understood. Theoretical angular distributions of other multipolarities do not improve the description. However, in Ref. [Sin09] and NNDC both states have been clearly assigned as 4⁺ states.

The 5⁻ states at 2490 and 3329 keV

Both states can be described with the angular distribution of a 5⁻ state. It would be desirable to measure a larger angular range in order to make these conclusions more reliable. The results are in agreement with Ref. [Sin09]. Only the state at 2490 keV is seen in Ref. [Fra05].

The 6⁺ state at 2948 keV

The cross section shape points to a 6⁺ state. In agreement with the results of Refs. [Fra05, Sin09].

The states at 3366 and 3643 keV

No quantum numbers could be assigned for the cross section of the states at 3366 and 3643 keV. In Ref. [Sin09] a 3⁻ at 3382 keV is seen which may correspond to the state at 3366 keV.

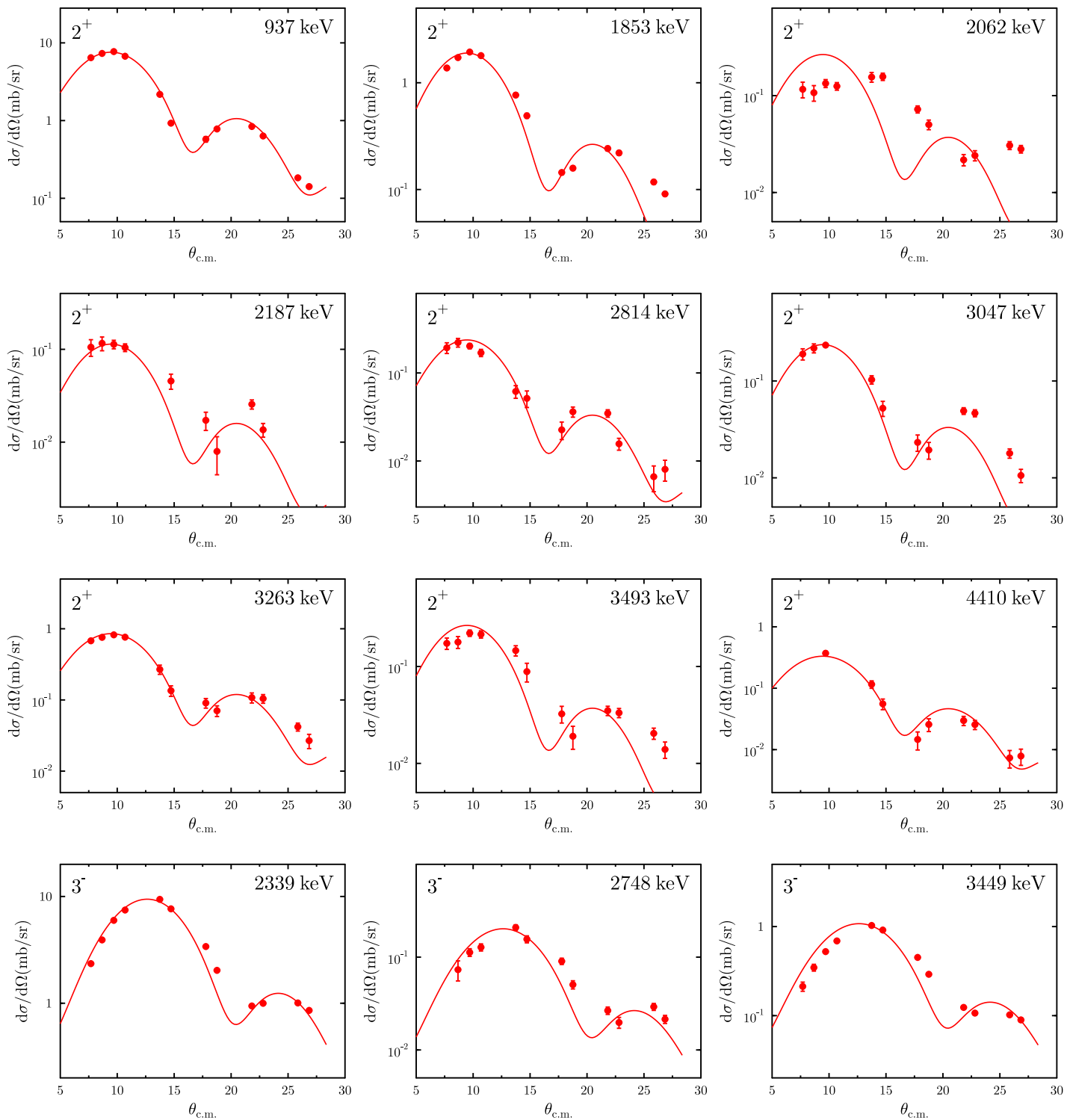


Figure 4.2: Comparison between angular distributions of the collective model to experimental data of the $^{92}\text{Zr}(p,p')$ -reaction.

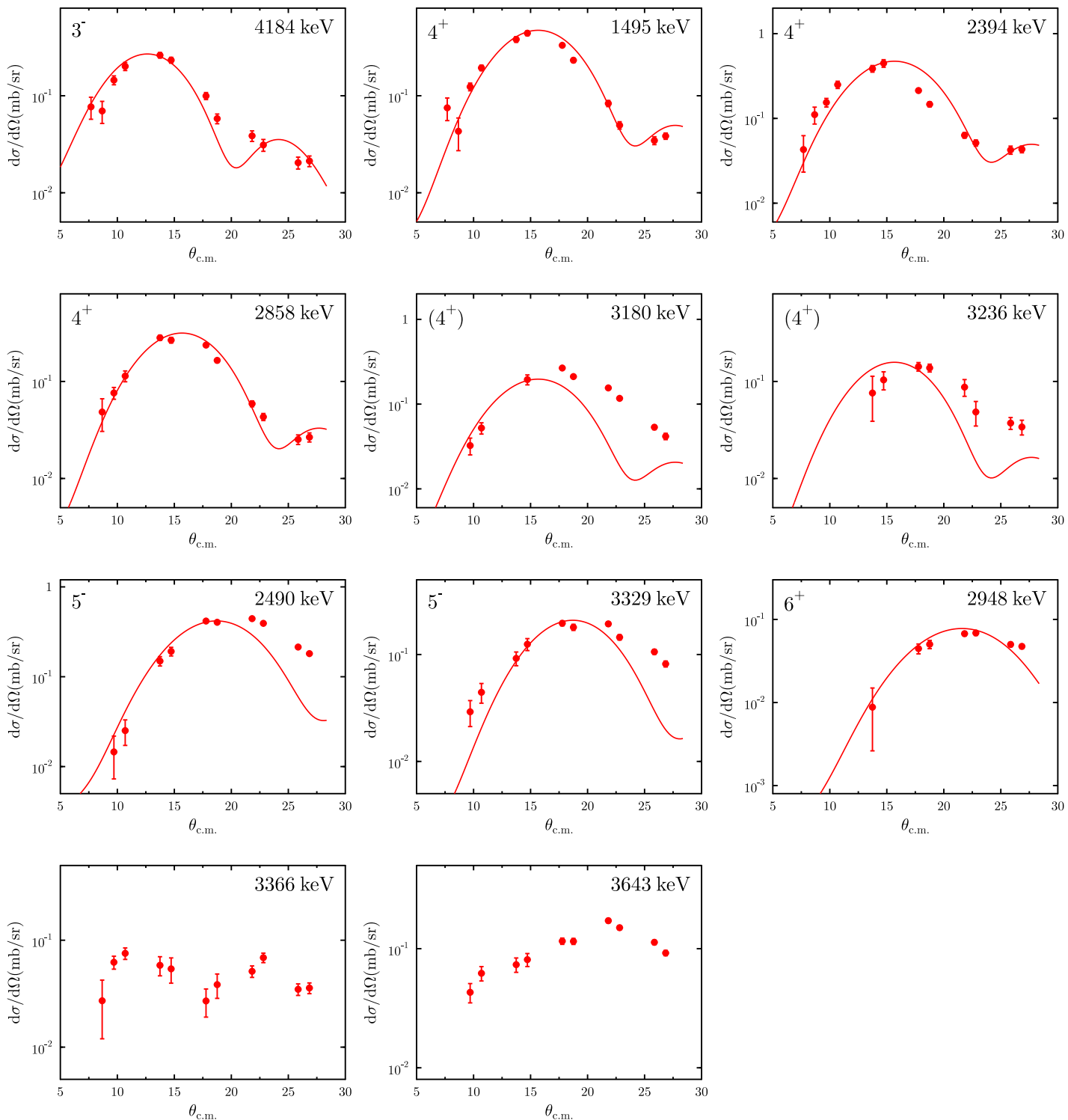


Figure 4.3: Comparison between angular distributions of the collective model to experimental data of the $^{92}\text{Zr}(p,p')$ -reaction.

4.1.6 Proton scattering results for ^{94}Mo

No	E_x (keV) ¹	E_x (keV) ²	E_x (keV) ³	J^π	J^π	J^π	$(d\sigma/d\Omega)_{max}$ (mb/sr) ¹
1	871(1)	871	871.09(1)	2 ⁺	2 ⁺	2 ⁺	10.02
2	1573(2)	1573	1573.72(1)	4 ⁺	4 ⁺	4 ⁺	1.03
3	1861(4)	1864	1864.3(1)	2 ⁺	2 ⁺	2 ⁺	
4	2062(4)	2068	2067.4(1)	2 ⁺	2 ⁺	2 ⁺	0.76
5	2394(4)	2393	2393.1(1)	2 ⁺	2 ⁺	2 ⁺	0.28
6	2534(1)	2534	2533.8(3)	3 ⁻	3 ⁻	3 ⁻	7.59
7	2608(2)	2611	2610.5(3)	5 ⁻	5 ⁻	5 ⁻	0.47
8	2769(2)	2770	2768.2(2)	4 ⁺	4 ⁺	4 ⁺	0.52
9	2865(2)		2870.0(2)	2 ⁺		2 ⁺	0.23
10	3008(2)	3014	3011.5(2)	3 ⁻	3 ⁻	3 ⁻	0.37
11	3382(2)	3396	3389.5(7)		5 ⁻	5 ⁽⁻⁾	
12	3452(2)			(4 ⁺)			0.32
13	3531(9)		3534.3(2)			2 ⁺	
14	3633(2)			(2 ⁺)			0.20
15	3798(3)	3802	3792.8(3)	2 ⁺	2 ⁺	2 ⁺	0.31
16	3996(3)	3995		2 ⁺	2 ⁺		0.22
17	4146(4)	4139		2 ⁺	2 ⁺		0.23

¹ this work

² Ref. [Pig92]

³ Ref. [Fra03] and NNDC

Table 4.4: Results of the $^{94}\text{Mo}(p,p')$ experiment evaluated in this thesis. The energy, spin and parity quantum numbers are compared to the results of Ref. [Pig92] and Ref. [Fra03]. The excitation energies of Ref. [Pig92] are accurate within 2 keV at ~ 2 MeV and 5 keV at ~ 4 MeV. The quantity $(d\sigma/d\Omega)_{max}$ is the cross section at the first maximum of the corresponding state.

The 2⁺ states at 871, 3798, 3996 and 4146 keV

Assuming a spin of 2 and a positive parity give a best fit to the data. This is in agreement with the results of Ref. [Pig92]. In Ref. [Fra03] the states at 871 and 3798 keV are also identified as 2⁺ states, while the states at 3996 and 4146 keV are out-of-range of this experiment.

The 2⁺ at 1861 keV

Like the 2₃⁺ state in ^{92}Zr two-step processes contribute to the shape of the cross section indicating large two-phonon components in the wave function. Ref. [Pig92] as well as Ref. [Fra03] make a 2⁺ assignment for this state.

The 2⁺ at 2062 keV

The angular distribution of the cross section deviates seriously from the one for a 2⁺ state. However, in Refs. [Pig92, Fra03] the state was unambiguously identified as a 2⁺ state. Indeed the deviations can be explained by considering the microscopic structure of this state and are due to its isovector nature. This will be the topic of chapter 5..

The 2⁺ at 2394 keV

The state is close to the 6⁺ state at 2423 keV. This doublet can not be resolved. Therefore, at larger scattering angles - where the contributions of the 6⁺ state become important - data points are not available. At smaller scattering angles the angular distribution points to a 2⁺ state which is in agreement with Refs. [Pig92, Fra03].

The 2⁺ at 2865 keV

Like the state at 2394 keV this state is close to a 6⁺ state at an energy of 2872 keV. The 2⁺ state is located at 2870 keV according to Ref. [Fra03]. Of course, this doublet can not be resolved. Hence, at larger scattering angles the contributions of the 6⁺ state become important and enhance the absolute cross section. At smaller scattering angles a pure one-step 2⁺ cross section describes the data best. This result is in sharp contrast to Ref. [Bur07] which identified this state as a two-phonon state. Considering the contributions of the 6⁺ there is no sign, in the present data, for a two-phonon state.

The tentative 2⁺ state at 3633 keV

The angular distribution can not be described by any theoretical cross section. However, the location of the first maximum being at small scattering angles indicates a 2⁺ state. This state is not seen in Refs. [Pig92, Fra03].

The 3⁻ state at 2534 keV

The angular distribution indicates a 3⁻ state in agreement with Refs. [Pig92, Fra03].

The $2^+/3^-$ doublet at 3008 keV

The state is a doublet formed by a 2^+ state at 2993 keV and a 3^- state at 3011 keV. This doublet can not be resolved. The angular distribution is described best by assuming a spin of 3 and negative parity. This points to a collective 3^- state.

The 4^+ states at 1573 and 2768 keV

In agreement with Refs. [Pig92, Fra03] the angular distributions indicate a 4^+ assignment for both states.

The tentative 4^+ state 3452 keV

The cross section shape is described best assuming a 4^+ state. Due to the deviations at smaller scattering angles only a tentative assignment is possible. The state was not seen in Refs. [Pig92, Fra03].

The 5^- state at 2608 keV

In agreement with Refs. [Pig92, Fra03] the angular distribution indicates a 5^- state.

The states at 3382 and 3531 keV

No spin and parity assignments could be made for these states. In Ref. [Fra03] the first one is identified as a 5^- state and the second one as a 2^+ state.

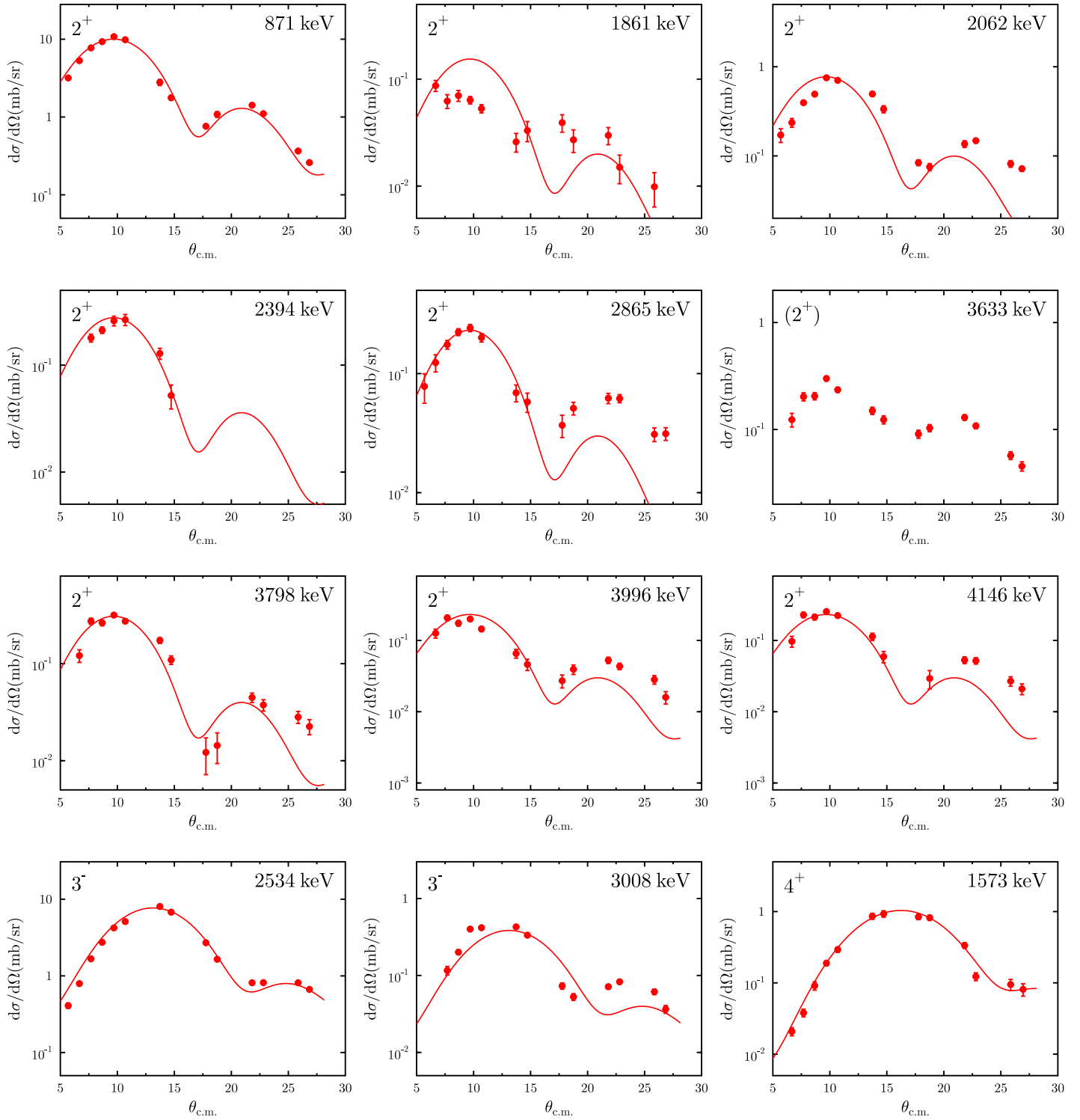


Figure 4.4: Comparison between angular distributions of the collective model to experimental data of the $^{94}\text{Mo}(p,p')$ -reaction.

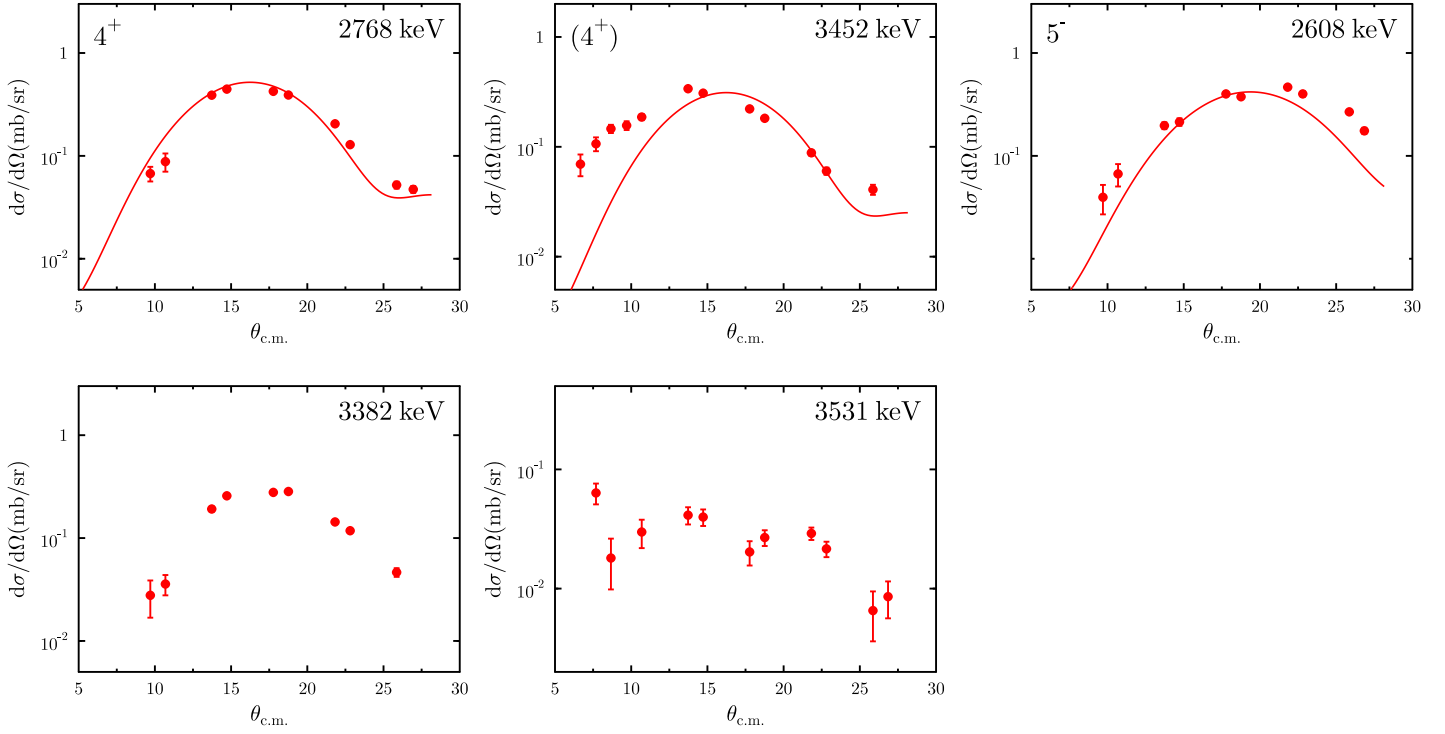


Figure 4.5: Comparison between angular distributions of the collective model to experimental data of the $^{94}\text{Mo}(p,p')$ -reaction.

4.1.7 Comparison to QPM results

All angular distributions of a given spin presented in the last sections have very similar shapes (except for the two important states mentioned before). Hence, the main experimental observable accessible is the magnitude of the cross sections, *i.e.* information about the isoscalar transition strengths. In principle it would be possible to obtain from the β_L^2 coefficients defined in Eq. 4.7 the isoscalar transition strengths. However, this quantity is highly sensitive to the chosen set of optical model parameters and assumes the validity of the collective model form factors which is not fully justified. The final aim is to compare the extracted isoscalar strengths distributions to results of the QPM. This can be done on a more fundamental way. The theoretical cross sections can be calculated by using directly the nuclear structure results of the QPM and a microscopic effective projectile-nucleus interaction. Four ingredients are necessary to obtain a theoretical cross section using the program DWBA07 [Ray07]:

- (i) the transition form factors provided by the QPM,
- (ii) the transition amplitude for inelastic proton scattering is provided by the free nucleon-nucleon t-matrix of Franey-Love, [Fra85] which can be written in coordinate space as

$$\begin{aligned}
 t(r) = & t_0(r) + t_\sigma(r)\vec{\sigma}_1 \cdot \vec{\sigma}_2 \\
 & + t_\tau(r)\vec{\tau}_1 \cdot \vec{\tau}_2 + t_{\sigma\tau}(r)(\vec{\sigma}_1 \cdot \vec{\sigma}_2)(\vec{\tau}_1 \cdot \vec{\tau}_2) \\
 & + t_{LS}(r)\vec{L} \cdot \vec{S} + t_{LS\tau}(r)(\vec{L} \cdot \vec{S})(\vec{\tau}_1 \cdot \vec{\tau}_2) \\
 & + t_T(r)S_{12}(\vec{r}) + t_{T\tau}(r)S_{12}(\vec{r})(\vec{\tau}_1 \cdot \vec{\tau}_2)
 \end{aligned} \tag{4.8}$$

- (iii) an optical potential calculated from this interaction,
- (iv) single particle wave functions obtained as solutions of a Wood-Saxon potential (see Tab. 2.1).

The values of first maxima of the calculated and measured proton scattering cross section are compared with each other in the following figures. This procedure is carried out for the quadrupole and hexadecapole states in ^{92}Zr (see Fig. 4.6) and for the hexadecapole states in ^{94}Mo (see Fig. 4.7). In addition the distributions of the quadrupole transition strengths in ^{92}Zr and ^{94}Mo are compared to each other in Fig. 4.7. In general the QPM achieves a satisfying description of the cross section maxima and therefore of the isoscalar transition strengths.

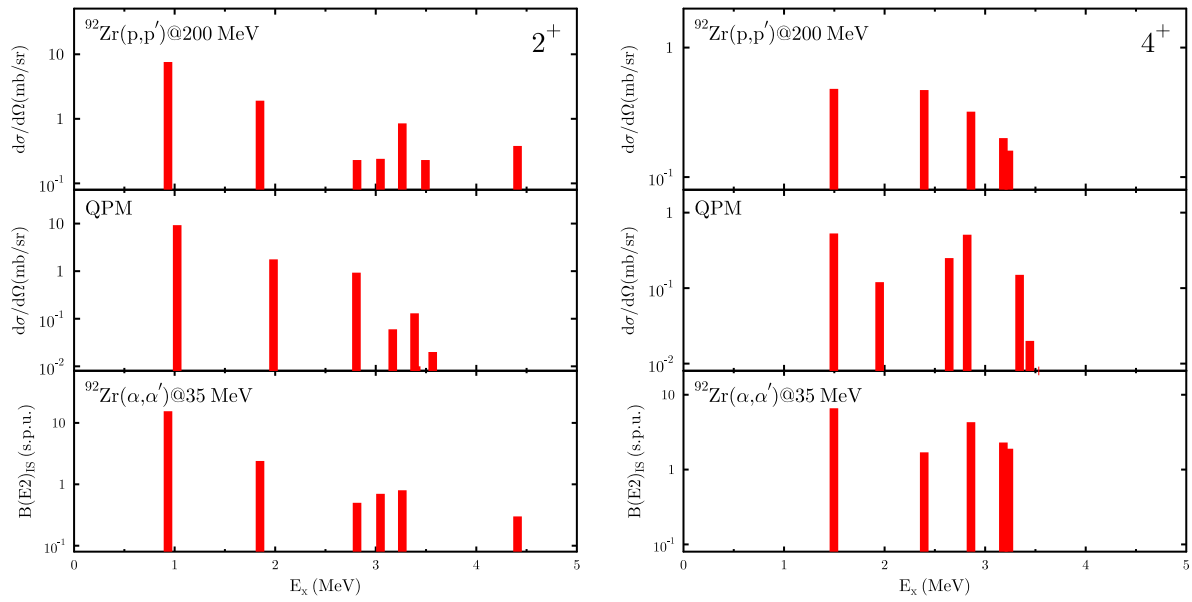


Figure 4.6: Comparison between measured cross section maxima of quadrupole (lhs) and hexadecapole (rhs) states in ^{92}Zr to QPM predictions and the isoscalar transition strengths deduced in Ref. [Sin09].

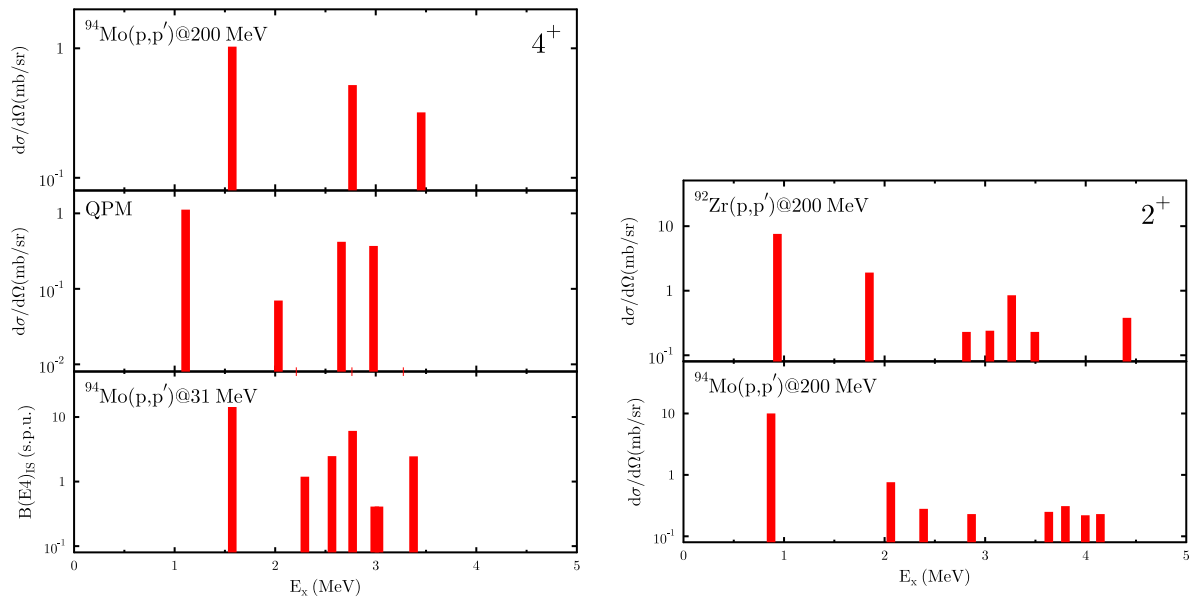


Figure 4.7: Comparison between measured cross section maxima of hexadecapole states in ^{94}Mo to QPM predictions and to the isoscalar transition strengths deduced in Ref. [Pig92] (lhs). The right-hand-side compares the isoscalar strengths distributions of ^{92}Zr and ^{94}Mo .

4.2 Electron scattering at ^{92}Zr

This section is organised as follows. First the data taking conditions are discussed concerning target properties, beam energy and scattering angles. The measured spectra are shown. Next the decomposition of the spectra and the procedure how to obtain the absolute cross sections are outlined. Finally, the statistical and systematic uncertainties are discussed and the results are presented.

4.2.1 Data taking conditions

The experiment was performed at the S-DALINAC using the Lintott spectrometer during a beam time in 2007. The beam energy was chosen to cover the first maximum of the quadrupole formfactors and amounts to 63.5 MeV. In total four spectra were taken under scattering angles of $\theta = 69^\circ, 81^\circ, 93^\circ$ and 117° . For the measurements a self-supporting target of 1.3 mg/cm^2 areal density and an enrichment of 93.4 % was used. In the energy-loss mode the achieved energy resolution amounts to $\Delta E \approx 30 \text{ keV}$ (full width at half maximum). Typically, the beam currents were about $1 \mu\text{A}$. The main parameters of the $^{92}\text{Zr}(e,e')$ experiment are summarized in Tab. 4.5. The measured spectra are shown in Fig. 4.8. The blind spots in the spectra are due to the limited size of the micro strip detectors (see Fig. 3.3).

areal density of the target	1.3 mg/cm^2
enrichment of the target	93.4 %
energy resolution	$\sim 30 \text{ keV}$
beam energy	63.5 MeV
beam currents	$1 \mu\text{A}$
evaluated energy range	0 - 2.4 MeV
scattering angles	$69^\circ, 81^\circ, 93^\circ, 117^\circ$

Table 4.5: The main parameters of the $^{92}\text{Zr}(e,e')$ -reaction.

4.2.2 Determination of the cross sections

The decomposition of the spectra was performed with the program FIT. In the most general case the fitting function consists of a polynomial $B(x)$ which describes the instrumental background and a function $y_i(x)$ which is assumed to describe the i -th individual peak. Here, the parameter x labels the excitation energy. The whole spectrum can be fitted with the function $F(x)$

$$F(x) = B(x) + \sum_i y_i(x). \quad (4.9)$$

An instrumental background is absent in the measured spectra. The shape of the function $y(x)$ - which must take into account the Gaussian form of the peak itself as well as the radiative tail due to electron energy losses in the target - was assumed to be given by

$$y(x) = y_0 \cdot \begin{cases} \exp(-\ln 2 \cdot (x - x_0)^2 / \Delta x_1^2) & x < x_0 \\ \exp(-\ln 2 \cdot (x - x_0)^2 / \Delta x_2^2) & x_0 \leq x \leq x_0 + \eta \Delta x_2 \\ D_1 / (D_2 + x - x_0)^\gamma & x > x_0 + \eta \Delta x_2 \end{cases} \quad (4.10)$$

with

- x_0 the position of the peak maximum,
 - y_0 the counting rate at the peak maximum
 - $\Delta x_{1,2}$ the half widths at half maximum for $E_x < x_0$ and $E_x \geq x_0$, respectively,
 - η the starting point of the radiative tail in units of Δx_2 ,
 - γ the exponent of the hyperbolic function of the radiative tail,
 - D_1 and D_2 determined from the condition of a smoothly differentiable connection of the second Gaussian function and the hyperbolic function at the intersection point $x_0 + \eta \Delta x_2$.
-

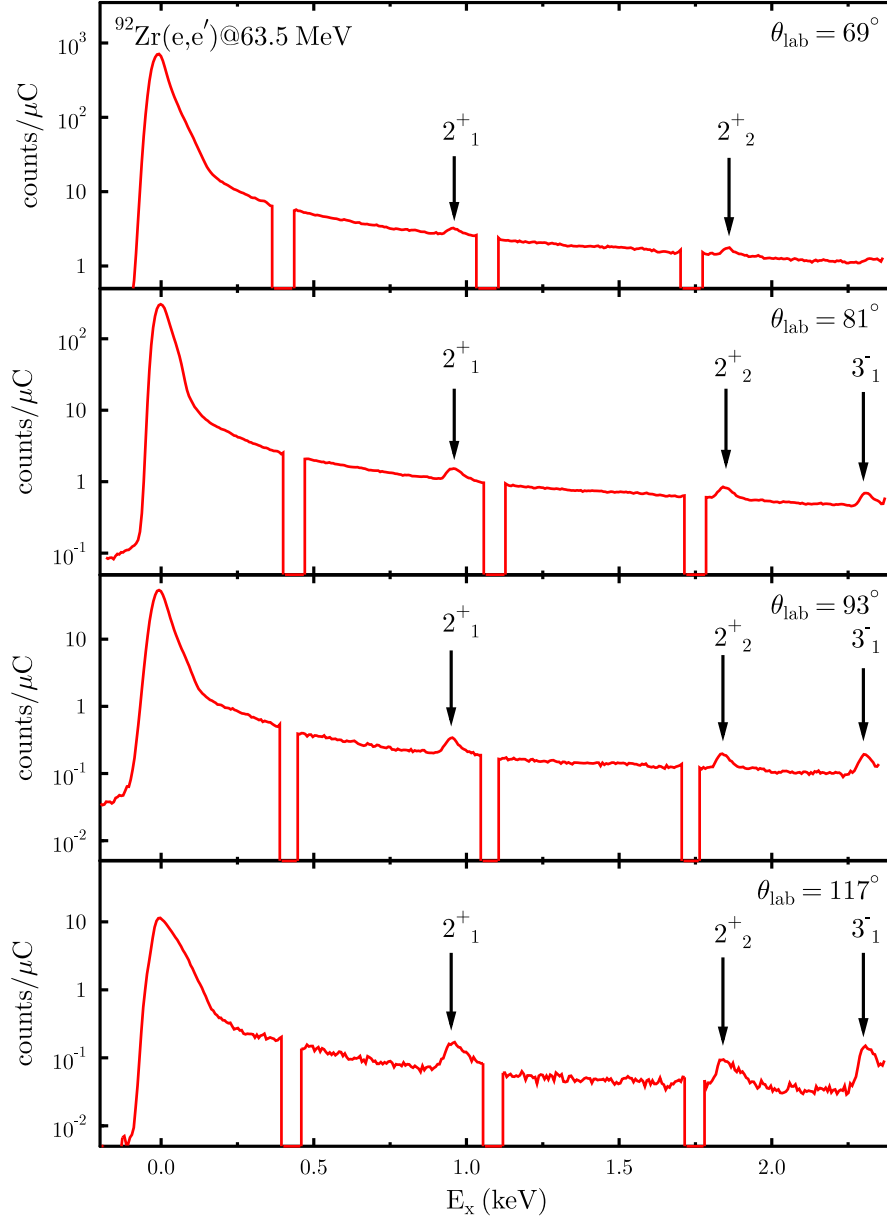


Figure 4.8: The measured spectra of the $^{92}\text{Zr}(e,e')$ reaction. Prominent transitions are labeled with their spin and parity quantum numbers.

The peak areas are determined by an integration of the model functions up to a cutoff limit of $E_{\text{cutoff}} = x_0 + 5\Delta x_1$. The missing peak areas are estimated by applying corrections called Schwinger δ_S , bremsstrahlung δ_B and ionization corrections δ_I . The Schwinger correction accounts for the emission of real photons and the emission and absorption of virtual photons. The bremsstrahlung correction is due to effects which cause an asymmetric distortion of the peak. These are caused by small angle scattering from electrons and nuclei other than the nucleus of interest. The ionization correction describes the energy loss of the electrons in the target due to atomic excitations and ionizations.

The final peak area is given by

$$A = A_{\text{int}} \cdot e^{\delta_S + \delta_B + \delta_I}, \quad (4.11)$$

where A_{int} is the peak area obtained from the integration of the model function y_i up to the cutoff limit. In the present analysis all parameters were fixed to the properties of the elastic peak. Only the counting rate y_0 and the peak position x_0 were treated as free parameters for each peak.

In principle it is possible to calculate the cross section of an excited state using Eq. 4.1. In contrast to proton scattering the electron scattering process is dominantly electromagnetic and the elastic scattering cross section can be calculated with a high accuracy in

the framework of Quantum Electrodynamics. Hence, it is preferred to determine the inelastic cross section $\left(\frac{d\sigma}{d\Omega}\right)_{in}$ relative to the elastic cross section $\left(\frac{d\sigma}{d\Omega}\right)_{el}$

$$\left(\frac{d\sigma}{d\Omega}\right)_{in} = \frac{A_{in}}{A_{el}} \cdot \frac{100}{\epsilon} \cdot \left(\frac{d\sigma}{d\Omega}\right)_{el}, \quad (4.12)$$

where A_{el} and A_{in} are the areas corrected for dead time and radiative processes for the elastic and inelastic peaks, respectively. It is necessary to account for the isotopes enrichment ϵ , since the elastic cross section contains contributions of the nucleus of interest as well as other stable isotopes like ^{90}Zr for the case of ^{92}Zr . The area of the inelastic peak corresponds only to the nucleus of interest. The elastic cross section were calculated using the phase shift code PHASHI [Bähr]. The charge density of the ground state was approximated by a three-parameter Fermi distribution. The parameters were taken from Ref. [Jag74].

4.2.3 Error estimate

Since, the absolute cross sections of the inelastic transitions were calculated relative to the elastic peak one avoids contributions of systematic errors in the determination of the solid angle and the accumulated charge in the Faraday cup as well as target inhomogeneities. The total uncertainty of the cross section includes

- statistical uncertainties in the peak area determination 2-4%
- error in the dead-time correction $\sim 1\%$
- inaccuracy in the calculation of the elastic cross section $\sim 2\%$

The errors were treated as independent from each other and taken to be the square root of the sum of the squared systematic and statistical errors.

4.2.4 Form factor results

The measured absolute cross sections of the excited states can be converted into form factors by calculating the ratio with the cross section for Mott scattering. The final results for the symmetric and mixed-symmetric states are given in Tab. 4.6. The parameter q stands for the momentum transfer, E_0 is the beam energy and θ gives the scattering angle.

q (fm^{-1})	E_0 (MeV)	θ (deg)	$ F(2_{is}^+) ^2 \times 10^{-4}$	$ F(2_{ms}^+) ^2 \times 10^{-4}$
0.35	63.5	69	3.98 ± 0.07	2.02 ± 0.04
0.41	63.5	81	5.19 ± 0.11	2.67 ± 0.08
0.46	63.5	93	5.39 ± 0.11	2.95 ± 0.08
0.54	63.5	117	7.94 ± 0.23	4.23 ± 0.17

Table 4.6: Transition form factors for the symmetric and mixed-symmetric states of ^{92}Zr . The errors include only the uncertainties in the peak area determination.

5 An alternative view on one-phonon quadrupole mixed-symmetry states

The main experimental signature for assigning a mixed-symmetric character to a 2^+ state is a strong M1 transition to the 2_1^+ state as discussed in section 2.1.2. This thesis presents for the first time an additional signature which manifests the different isospin character of the 2_1^+ (FSS) and 2_{ms}^+ (MSS) by a comparison of their charge and matter transition radii. Electron and proton scattering cross sections are analysed to obtain experimental informations about these quantities.

This chapter is organized as follows. First, the results of a QPM calculation for ^{92}Zr are presented and compared to various experimental observables. Based on these results, the idea for the new signature is developed in the framework of the QPM. Next - to check its validity - the charge and matter transition radii of the FSS and MSS are measured in ^{92}Zr , where the MSS is already identified based on absolute M1 transition matrix elements. The new signature motivates a novel explanation for the origin of effective forces used in quadrupole collective models and for the general formation mechanism of mixed-symmetry states. This is presented in section 5.3. Finally, some semi-quantitative considerations on the evolution of mixed-symmetry states in the N=50 region are discussed, based on a QRPA calculation [Pon10].

5.1 QPM results for ^{92}Zr

Since the IBM-2 does not work very well near closed shells and considers spin contributions to M1 transitions only in an average way [Hey10], microscopic approaches are needed to investigate the properties of mixed-symmetry states in ^{92}Zr . The shell model is the superior model for describing low-energy excitations near closed shells. However, since the aim of this work is to describe proton and electron scattering cross sections and to study - as will become clear in section 5.3 - the role of the Giant Quadrupole Resonance (GQR) on the formation of MSS, a QRPA based approach is favourable. The first point would in principle be possible in the shell model, but requires extensive theoretical calculations following the procedure of Ref. [Sag87]. The latter point is prohibited, due to the limited model space of the shell model. The QPM is a very suitable QRPA approach for these purposes, since it includes the coupling of one-phonon to two- and three-phonon states, which are known to be very important for the description of low-energy excitations.

The QPM calculations were performed following the procedure of section 2.2. The parameters of the Woods-Saxon potential used to obtain the single-particle basis were fixed to the properties of neighbouring nuclei and are given in Tab. 2.1. The strength of the pairing force was fitted to odd-even mass differences and the strength of the residual interaction was determined to describe the B(E2) value and the excitation energy of the 2_1^+ state. No additional parameters are needed to include the coupling to multi-phonon states. Since the QPM uses in contrast to the shell model a single-particle basis being sufficiently large to fulfill the energy weighted sum rules, no effective charges are necessary to describe the experimental B(E2) values. Magnetic transitions are calculated assuming a spin quenching factor of $g_s = 0.6$.

state	E (keV)		structure
	Exp	QPM	
2_1^+	934	1025	91% $[2_1^+]_{[RPA]}$
2_2^+	1847	1983	91% $[2_2^+]_{[RPA]}$
2_3^+	2066	2043	17% $[2_4^+]_{[RPA]}$ + 13% $[2_5^+]_{[RPA]}$ + 54% $[2_1^+ \otimes 2_1^+]_{[RPA]}$

Table 5.1: The structure of the three lowest 2^+ states in ^{92}Zr in terms of QRPA phonons. The 2_1^+ and 2_2^+ states are nearly pure one-phonon states, while the 2_3^+ is dominantly a two-phonon state with noticeable one-phonon contributions.

The wave functions of the three lowest 2^+ states are shown in Tab. 5.1 and Tab. 5.2. The 2_1^+ and 2_2^+ states are dominated by the first and second RPA phonons, respectively. The contributions of other one-phonon, two-phonon and three-phonon states are less than 10%. The first and second RPA-phonons are mainly formed by the same two two-quasiparticle components $(2d_{5/2} \otimes 2d_{5/2})_n$ and $(1g_{9/2} \otimes 1g_{9/2})_p$. In case of the $[2_1^+]_{[RPA]}$ both components are in-phase and for the $[2_2^+]_{[RPA]}$ out-of-phase forming the microscopic analogue of the symmetric and mixed-symmetric one-quadrupole phonon states defined in the framework of the IBM-2.

Indeed, as shown in Tab. 5.3, both states are connected by a strong M1 transition. Besides the two dominant two-quasiparticle components, both RPA phonons contain many two-quasiparticle components (not shown in this table), which contribute with small amplitudes to the wave function, but are large in number and all in-phase. They are mainly $2\hbar\omega$ -excitations and belong to the

GQR as will be discussed in the next sections. Surprisingly, the GQR admixture in the wave function is mainly responsible for the enhanced $B(E2)$ values of the 2_1^+ and 2_2^+ states in ^{92}Zr .

$q_1 \otimes q_2$	$[2_1^+]_{[RPA]}$			$[2_2^+]_{[RPA]}$		
	ψ	ϕ	%	ψ	ϕ	%
$(2d_{5/2} \otimes 2d_{5/2})_n$	1.20	0.16	70.98	-0.76	0.11	28.30
$(2d_{5/2} \otimes 3s_{1/2})_n$	0.19	0.07	2.91	0.37	0.05	13.09
$(2d_{5/2} \otimes 1g_{9/2})_n$	0.20	0.11	2.65	0.23	0.08	4.76
...
$(1g_{9/2} \otimes 1g_{9/2})_p$	0.51	0.19	11.03	0.8008	0.0892	31.66
$(1f_{5/2} \otimes 2p_{1/2})_p$	0.23	0.10	4.47	0.2866	0.0464	8.00
$(2p_{3/2} \otimes 2p_{1/2})_p$	0.23	0.09	4.47	0.3059	0.0442	9.16
...

Table 5.2: Wave functions of the $[2_1^+]_{[RPA]}$ and $[2_2^+]_{[RPA]}$ -phonons in ^{92}Zr . ϕ and ψ are the forward and backward amplitudes defined in Eq. 2.49. The numbers in percentage label the contribution of each two-quasiparticle state to the norm of Eq. 2.51. Both states are dominated by two two-quasiparticle components which are in-phase for the $[2_1^+]_{[RPA]}$ forming a symmetric state and out-of-phase for the $[2_2^+]_{[RPA]}$ forming a mixed-symmetric state.

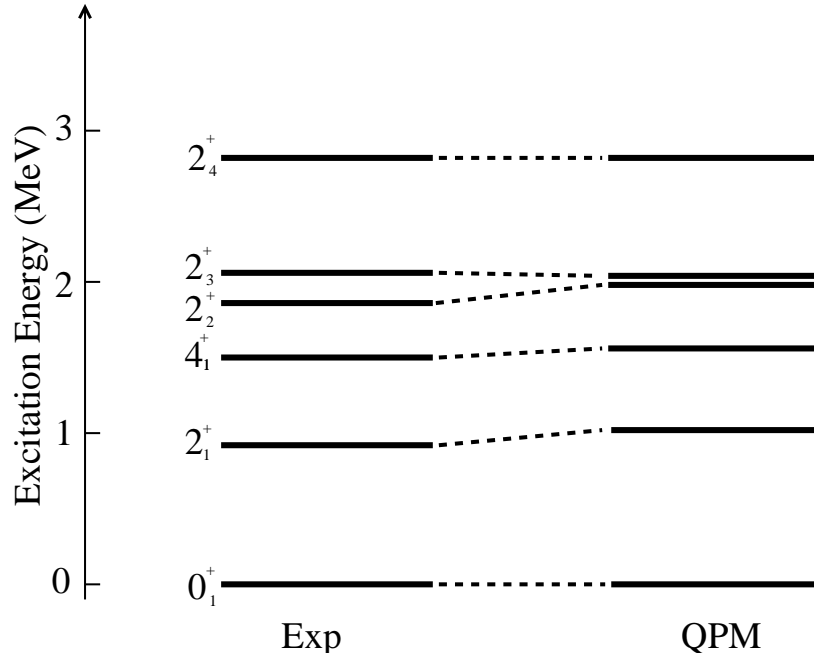


Figure 5.1: Comparison of the calculated and measured excitation energies of the low-lying states in ^{92}Zr . The QPM provides an excellent description of the excitation energies.

The 2_3^+ state has a different structure. Its main amplitude is a two-phonon component formed by the first RPA-phonon. However, the contributions of the $[2_4^+]_{[RPA]}$ - and $[2_5^+]_{[RPA]}$ -phonons are appreciable and indicate deviations from a harmonic phonon picture.

The validity of the QPM predictions and the wave functions in Tab. 5.1 and Tab. 5.2 can only be tested by a comparison to experimental data. Since in ^{92}Zr a large amount of complementary experimental observables - being sensitive to different parts of the wave functions - is available, a detailed test can be performed.

Figure 5.1 presents a comparison between measured and calculated excitation energies of the five lowest states. The QPM reproduces the experimental energies with an accuracy of ~ 100 keV. The comparison between experimental and calculated E2 and M1 transition strengths is shown in Tab. 5.3. Again the QPM accounts well for the decay properties of the symmetric and mixed-symmetric 2^+ states.

Finally, Tab. 5.4 proves, that the QPM is also able to account for the g factors of the FSS and MSS [Wer08]. This quantity gives valuable informations about the main components in the wave function. The negative g factor of the FSS indicates an appreciable contribution of the $(2d_{5/2} \otimes 2d_{5/2})_n$ two-quasiparticle component to its wave function. This feature is nicely reproduced by the wavefunctions of Tab. 5.2.

$J_i \rightarrow J_f$	B(E2)(W.u.)		B(M1)(μ_N^2)	
	Exp	QPM	Exp	QPM
$2_1^+ \rightarrow 0_1^+$	6.4(6)	5.9		
$2_2^+ \rightarrow 0_1^+$	3.4(4)	2.6		
$2_3^+ \rightarrow 0_1^+$	<0.005	0.1		
$2_2^+ \rightarrow 2_1^+$			0.37(4)	0.64

Table 5.3: Comparison of the calculated and measured transition strengths in ^{92}Zr . The symmetric and mixed-symmetric states are connected by a strong M1-transition.

$g(J^\pi)(\mu_n)$	Exp	QPM
$g(2_1^+)$	-0.18(1)	-0.09
$g(2_2^+)$	0.76(50)	0.31

Table 5.4: Comparison of the calculated and measured g-factors in ^{92}Zr [Wer08].

In summary the QPM accounts very well for the properties of the lowest states in ^{92}Zr and describes with a reasonable accuracy a large body of complementary experimental data. This gives strong evidence for the validity of the wave functions given in Tab.5.1 and Tab. 5.2. Based on these successful calculations one can try a further analysis of the properties of the FSS and MSS in ^{92}Zr .

5.2 One-phonon mixed-symmetry states in electron and proton scattering

In order to find a new experimental signature for proving the different isospin character of the FSS and MSS, the transition densities of the 2_{fs}^+ (upper part) and 2_{ms}^+ (lower part) in ^{92}Zr are examined in Fig. 5.2. The transition densities are calculated using the wavefunctions of Tab. 5.1 and Tab. 5.2 which account - as proven in the previous section - for a large amount of experimental data. The proton and neutron transition densities are shown separately. For both states the maximum of the neutron transition density (~ 6 fm) is displaced to the exterior compared to the maximum of the proton transition density (~ 5 fm).

The corresponding one-body operator allows a decomposition of each full transition density (solid lines) in two pieces: A collective part stemming mainly from the GQR (dotted lines) and the contribution of the largest valence two-quasiparticle components (dashed lines), *i.e.* $(2d_{5/2} \otimes 2d_{5/2})$ in case of neutrons and $(1g_{9/2} \otimes 1g_{9/2})$ in case of protons. The key point is the different radial behaviour of each transition density. An out-of-phase coupling of the neutron valence contribution to the GQR - as for the MSS - will cause two effects:

- (i) first a reduction of the full neutron transition density with respect to the FSS, due to the negative sign of this dominant neutron component. As a consequence the matter transition density ($\rho_{\text{matter}} = \rho_n + \rho_p$), will be shifted to the interior,
- (ii) and second a shift of the full neutron density to the nuclear interior due to the subtraction of the specific shape of the $(2d_{5/2} \otimes 2d_{5/2})_n$ -part having a maximum at a *larger* radius than the GQR.

For the FSS this effect is reversed and the transition density is shifted to the exterior. Both effects contribute coherently to a *reduction* of the *matter* transition radius when going from the FSS to the MSS. By contrast the *charge* transition radii will essentially be *the same*, since in both states the $(1g_{9/2} \otimes 1g_{9/2})_p$ -part couples in-phase to the GQR. The maxima of the GQR, full and valence transition densities are marked with vertical lines in Fig. 5.2 to highlight this effect. Figure 5.3 displays the matter transition densities for both states. The matter transition density of the MSS is displaced to the interior compared to the FSS, as expected from the considerations made above. To quantify these conclusions, Tab. 5.5 shows the transition radii of the charge, neutron and matter transition densities defined as

$$R_{\text{tr}} = \sqrt{\frac{\int \rho(r) \cdot r^4 \cdot dr}{\int \rho(r) \cdot r^2 \cdot dr}}, \quad (5.1)$$

where $\rho(r)$ is the corresponding density. As expected, the charge transition radii are nearly the same, while the neutron and matter transition radii differ by 0.207 fm and 0.152 fm, respectively.

In summary the different coupling of the $(2d_{5/2} \otimes 2d_{5/2})_n$ -configuration to the GQR causes a *sensitivity of the matter transition radii to the different isospin character* of the FSS and MSS. This can be considered as an alternative way to prove the mixed-symmetric character of the MSS, independently of M1 transition matrix elements.

How can these model dependent predictions be verified experimentally? Obviously, the matter transition radii of the FSS and MSS has to be measured, but in addition it is necessary to test if the charge transition radii are really the same. Otherwise one can

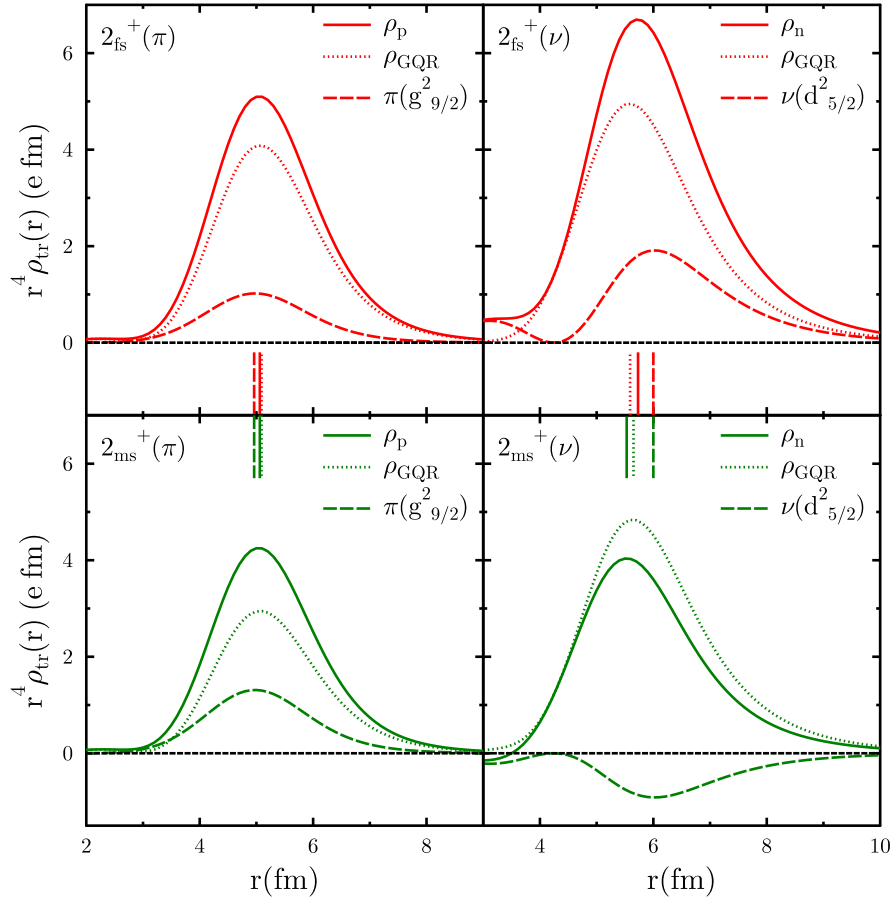


Figure 5.2: The proton and neutron transition densities weighted with r^4 for the symmetric (top) and mixed-symmetric state (bottom). Every full transition density (solid lines) is decomposed in two parts: The contribution of the largest configuration of Tab.5.2 (dashed lines) and the remaining parts stemming mainly from the GQR (dotted lines). The proton transition densities are very similar for both states and differ only in magnitude. The full neutron transition density for the MSS is shifted to the interior in comparison to the FSS, due to the out-of-phase coupling of the $(2d_{5/2} \otimes 2d_{5/2})$ -configuration to the GQR. The vertical lines mark the positions of the maxima.

	R_π (fm)	R_ν (fm)	R_{matter} (fm)
2_{fs}^+	4.762	5.162	4.992
2_{ms}^+	4.688	4.955	4.841
ΔR	0.074	0.207	0.152

Table 5.5: The charge, neutron, and matter transition radii of the FSS and MSS in ^{92}Zr and their differences ΔR .

not be sure, if the displacement of the matter transition radii is due to a change in the neutron transition densities - as predicted - or if maybe a change in the proton transition densities of both states is responsible for this effect.

Apparently two probes with a different sensitivity to protons and neutrons are needed to study this. Electron scattering at low momentum transfers is known to be very sensitive to the charge transition radius [Hei83]. Therefore, the data from section 4.2 is compared in Fig. 5.4 (lhs) to DWBA form factors calculated using the charge transition densities of Fig. 5.2 with the code of Ref. [Hei83]. The QPM achieves an excellent description of the electron scattering data points concerning magnitude and momentum transfer dependence showing the validity of the charge transition radii in Tab. 5.5.

To illustrate the sensitivity of the electron scattering data to the charge transition radius at least qualitatively, one can form the ratio of both form factors using the expansion given in Ref. [Hei83]

$$\frac{F(2_{ms}^+, q)}{F(2_{fs}^+, q)} = \frac{\sqrt{B(E2_{ms}^+)} \cdot (1 - (q^2/14)R_{ms}^2 + \dots)}{\sqrt{B(E2_{fs}^+)} \cdot (1 - (q^2/14)R_{fs}^2 + \dots)}, \quad (5.2)$$

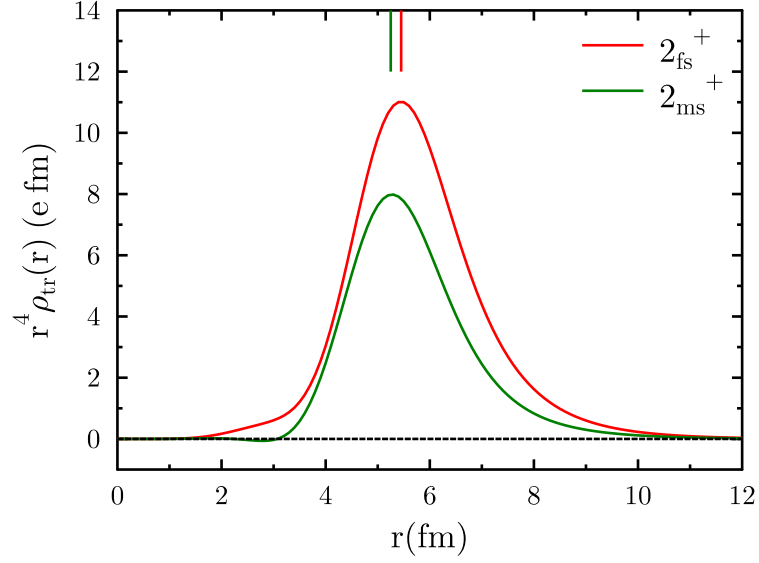


Figure 5.3: The matter transition densities (sum of proton and neutron transition densities) of the symmetric and mixed-symmetric states. Since 800 MeV protons interact dominantly isoscalar with the target nuclei, these densities are 'seen' by the proton. The transition density of the mixed-symmetric state is shifted to the interior in comparison to the symmetric state.

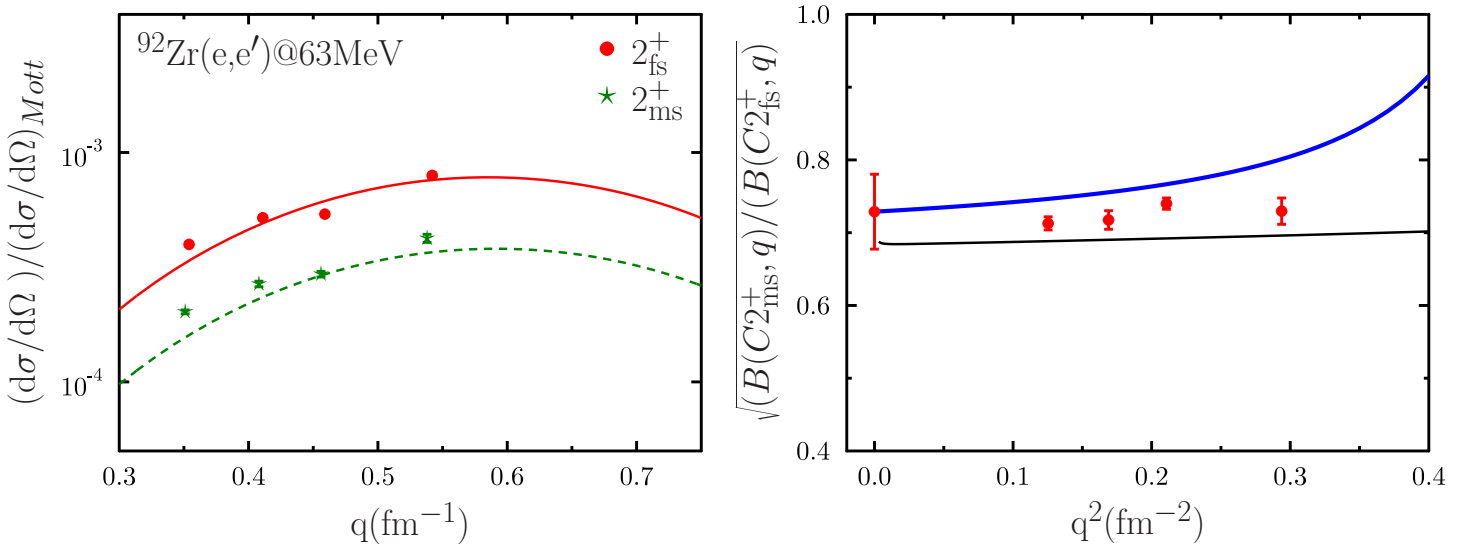


Figure 5.4: The formfactors of the symmetric and the mixed-symmetric states compared to DWBA calculations employing the QPM transition densities (lhs). Both formfactors have very similar shapes indicating approximately the same transition radii. On the right hand side is shown the square root of the ratio of both formfactors.

where R_{fs} and R_{ms} are the charge transition radii of the symmetric and mixed-symmetric state, respectively. The expansion is only meaningful for light nuclei, due to the uncertainties in the Coulomb correction factors caused by the strong Coulomb field of heavy nuclei. However, forming the ratio offers the possibility to become approximately independent of both Coulomb correction factors, since they should cancel to some degree [Hei83]. In case of equal transition radii, the ratio of Eq. 5.2 would be *independent* of q . Indeed, the five data points shown in Fig. 5.4 exhibit a nearly constant value over the measured q range (note that the value at $q = 0$ is given by the ratios of the $B(E2)$ values according to Eq. 5.2). The solid black line shows the ratio of the QPM form factors being nearly constant. The solid blue line is calculated with Eq. 5.2 using the experimental transition strengths and assuming arbitrary values of $R_{fs} = 5.2$ fm and $R_{ms} = 5.0$ fm. Clearly, the sharp slope does not match the experimental data. Therefore, the electron scattering results point to very similar charge transition radii in agreement with the values given in Tab. 5.5.

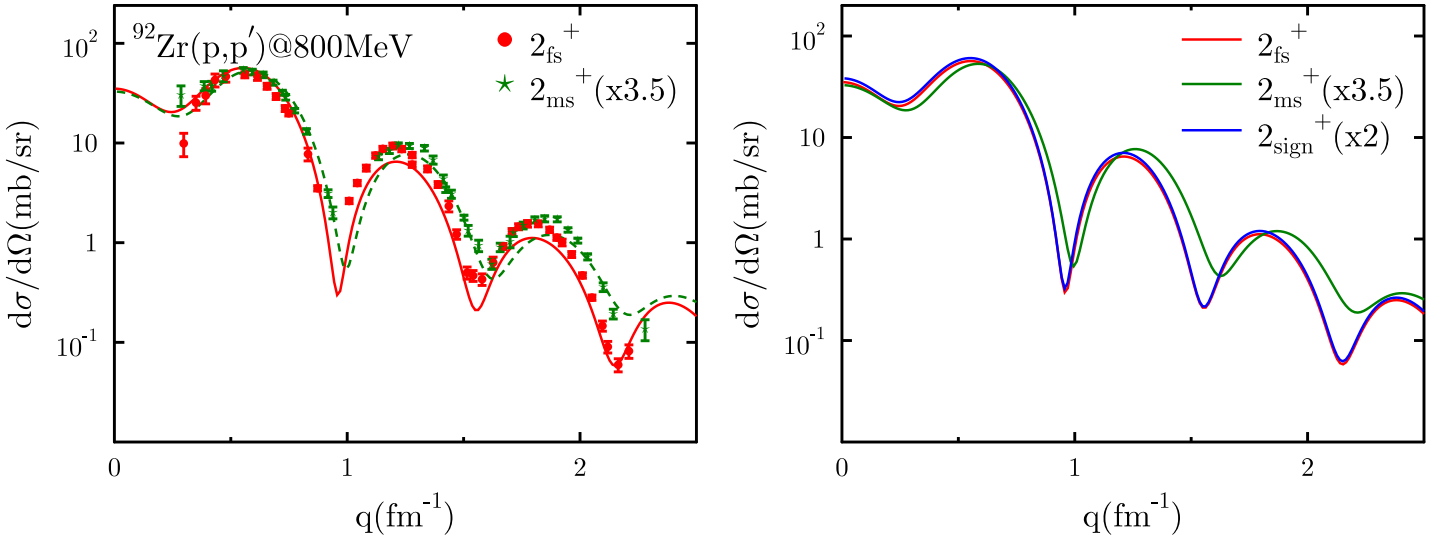


Figure 5.5: The cross sections of 800 MeV proton scattering for the symmetric (filled red circles) and mixed symmetric 2^+ states (green stars) taken from Ref. [Bak75]. The cross sections calculated within the QPM using the effective interaction of Ref. [Fra85] achieve a good description of the experimental data and reproduce the crucial shift, which is due to the isovector nature of the mixed symmetric state. The figure on the right hand side illustrates the dependence of the cross sections on the sign of the $(2d_{5/2} \otimes 2d_{5/2})_n$ configuration. For a detailed explanation see text.

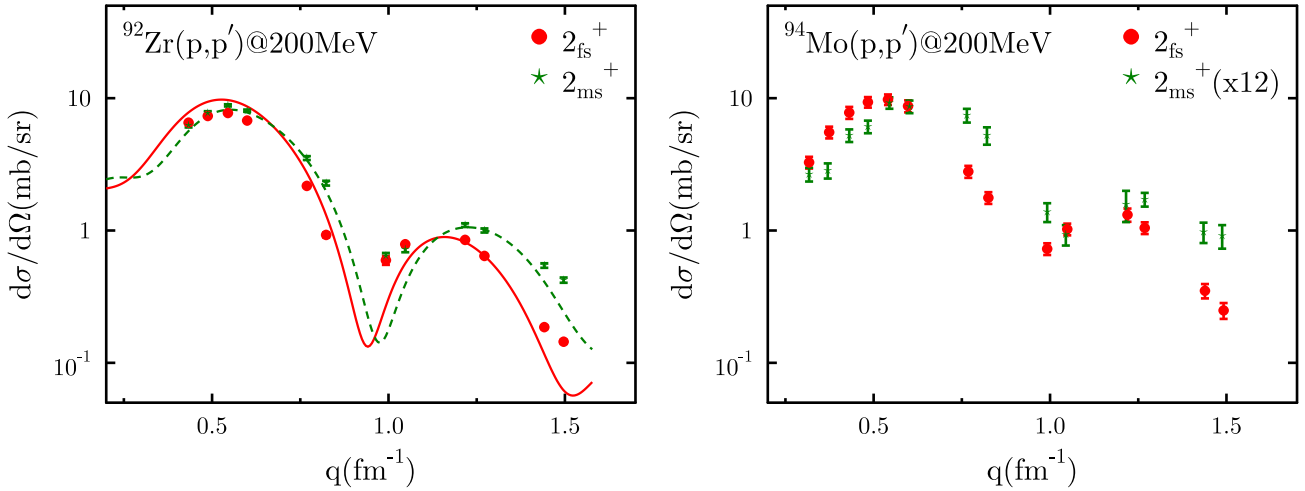


Figure 5.6: The shift in the cross sections can also be found in the 200 MeV proton scattering data analyzed in this thesis. On the left hand side are shown the cross section for ^{92}Zr and on the right hand side for ^{94}Mo . Even only a few data points are available, the shift can clearly be seen in both cases. In ^{94}Mo it is much stronger which can be attributed to the lower collectivity of the MSS compared to ^{92}Zr .

The left hand side of Figure 5.5 displays the proton scattering cross sections measured at 800 MeV which are taken from Ref. [Bak75]. Due to the strong nuclear force the interaction between the incident proton and the nucleus takes mainly place at the surface, consequently proton scattering is highly sensitive to the size of the matter transition radius [Wam10]. Protons interact dominantly through the isoscalar central channel of the effective nucleon-nucleus force at an incident energy of 800 MeV [Fra85]. Hence, the sum of the neutron and proton transition density is the important quantity. Clearly, as expected, the features of the (p,p') cross sections of the MSS are shifted to higher q values as compared to those of the FSS indicating a larger matter transition radius of the symmetric state. The QPM describes both cross sections reasonably well pointing to the validity of the matter transition radii given in Tab. 5.5. For calculating the cross sections the code DWBA07 [Ray07] has been used taking the widely used t-matrix parametrization of Franey-Love [Fra85] as an effective projectile target interaction.

The right hand side of Fig. 5.6 illustrates the sensitivity of the proton scattering cross section to the sign of the $(2d_{5/2} \otimes 2d_{5/2})_n$ configuration. Besides the cross sections of the FSS (red line) and MSS (green line), Fig. 5.6 shows the cross section (blue line) for the transition density of the MSS where the sign of the $(2d_{5/2} \otimes 2d_{5/2})_n$ configuration has been artificially switched from minus to plus forming a 'symmetric state'. As a result the cross section is displaced to smaller q-values and nearly coincides with the cross section of the FSS. Hence, in the framework of the QPM the observed shift can be clearly attributed to the isovector nature of the 2_{ms}^+ state.

In conclusion the electron and proton scattering data support the QPM values of the matter and charge transition radii given in Tab. 5.5. Since, the difference in the matter transition radii is due to the different isospin character of both states, this is an alternative way for identifying the 2_2^+ in ^{92}Zr as the MSS.

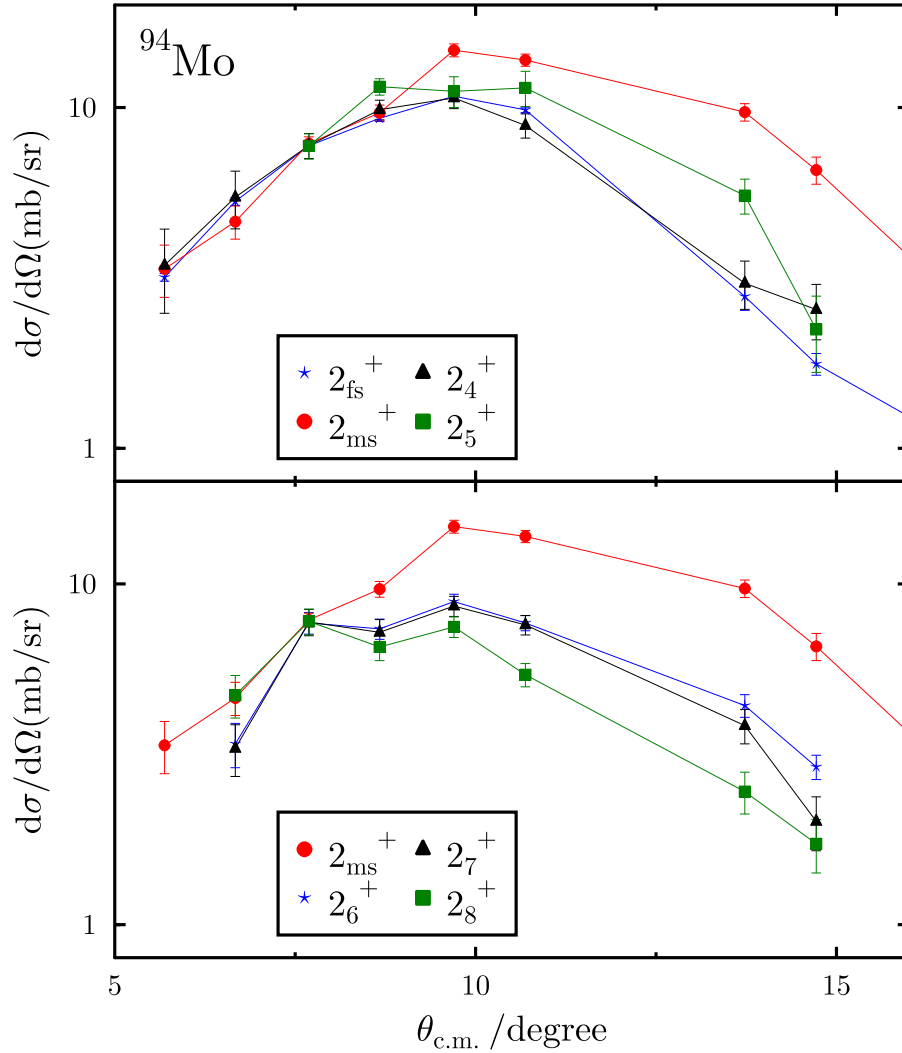


Figure 5.7: Comparison between the cross section of the MSS and all other quadrupole states in ^{94}Mo . The solid lines are drawn to guide the eyes. The cross section are scaled to the data point at $\theta_{c.m.} = 7.69^\circ$ of the 2_{fs}^+ .

Can this shift be found in other proton scattering data and nuclei as well? On the left hand side of Figure 5.6 is presented the proton scattering data of chapter 4 measured at 200 MeV. Despite the limited data points the shift in the cross sections can clearly be identified. In addition on the right hand side one can see the cross section of the FSS and MSS in ^{94}Mo . Also in this case the shift is clearly visible being even stronger than in ^{92}Zr . These additional examples point to a very robust nature of the new signature for a mixed-symmetry state. In addition the observed shift allows to measure for the first time the *relative signs* between the GQR and the two large valence two-quasiparticle components, since a change of sign of the proton component would cause different charge transition radii and a shift of the matter transition density to the exterior. This is an observable not accessible in gamma spectroscopy. It is very interesting that such an observable can really be measured directly, although other observables like the B(M1)-strength are insensitive to this quantity.

The most interesting and promising consequence of the observed shift in the matter transition radii is displayed in Fig. 5.7. The proton scattering data of the MSS in ^{94}Mo are compared to all other 2^+ states measured in the experiment of section 4.1.6. A total

number of eight quadrupole states has been identified. The 2_2^+ is a two-phonon state with a very different cross section shape due to two-step processes, hence it is not included in the discussion. For a better illustration the MSS is compared to states below 3 MeV (upper part) and above 3 MeV, separately. Figure 5.7 is restricted to the first maximum, since not for all 2^+ states proton scattering data are available at larger scattering angles. *Without any exception the cross section of the MSS is shifted strongest to larger scattering angles indicating a smaller matter transition radius compared to all other 2^+ states in ^{94}Mo .* This is a surprise, because most of the 2^+ states are non-collective having B(E2) values which are up to two orders of magnitude smaller than the ground state transition of the 2_1^+ , *i.e.* the admixture of the GQR is small. Therefore, the matter transition radii of these non-collective states depend on their single-particle components which might cause very different transition radii. However, the shift of the matter transition radius of the MSS due to its isovector nature is so strong that it dominates all other effects. This is a very important observation. *It will allow to identify the MSS solely by measuring proton scattering cross section, although absolute M1 transition strength are not known.* Remembering the results of ^{92}Zr , the shift can be expected to increase at larger scattering angles making this effect even more apparent than in Fig. 5.7.

It would be very interesting to study the properties of the shift along an isotopic chain. The Mo-chain is a promising candidate. The next heavier nucleus is ^{96}Mo . Here, a MSS is already identified from M1 matrix elements. The B(E2) value of the MSS decreases from 1.6 W.u. in ^{94}Mo to 0.08 W.u. in ^{96}Mo , *i.e.* the shift can be expected to be even stronger than in ^{94}Mo (clearly, the shift becomes stronger with decreasing collectivity of the MSS). In ^{98}Mo no MSS is known so far and the shift offers the possibility to identify for the first time a MSS in this nucleus. One may even think of investigating the deformed nucleus ^{100}Mo and try to study the evolution of the MSS from nearly spherical to deformed nuclei. It should be noted that the $(n,n'\gamma)$ -reaction - one of the main experimental methods to obtain information about B(M1) values between two excited states - becomes uncertain when the level density is high (because of its non-selective excitation mechanism at low neutron energies). Measuring proton scattering cross section with a high energy resolution up to the second minimum with a sufficient number of data points might be an alternative to study the properties of MSS in heavier nuclei away from closed shells.

In addition it is questionable if the $B(\text{M1}:2_{\text{ms}}^+ \rightarrow 2_{\text{ms}}^+)$ strength is a unique experimental observable to identify a MSS in deformed nuclei, since it is decreasing with increasing square of the deformation parameter (see Fig. 5.12). It is not clear whether this decrease can be attributed to a 'washing out' of the MSS or maybe a structural change in the 2_1^+ state is the reason. The B(M1) strength depends on the structure of both states and cannot answer this question. In contrast the proton and electron scattering cross section depend only on the structure of a single excited state. This is an important advantage. Whether the idea of the shift really works in more deformed nuclei, can only be decided by experiment.

So far three things could be learned from the observed shift in proton scattering: First, the different isospin character of the FSS and MSS in ^{92}Zr has been proven in an alternative way independent from electromagnetic transition matrix elements. Second, the relative signs between the valence components and the GQR has been measured for the first time. Finally, Fig. 5.7 proves that the small matter transition radius is a unique feature of the MSS which no other 2^+ state shares, hence it can be used to identify a MSS, without knowledge of the $B(M1: 2_{\text{ms}}^+ \rightarrow 2_1^+)$ strength.

Besides these pleasant points, the shift gives experimental evidence for having three main building blocks contributing to the wave functions of the FSS and MSS: The GQR, a main proton and a main neutron two-quasiparticle component. In addition, the strong $B(M1)$ strength between the FSS and MSS proves the strong mixing between the two latter components. In collective valence space models like the IBM-2 this mixing is caused by an effective proton-neutron interaction. This force is a key ingredient for the IBM-2 and is responsible for many nuclear structure phenomena resulting from configuration mixing like deformation and phase shape transitions. However, in the IBM-2 a microscopic justification for this effective force between bosons is still missing. The new experimental results obtained in the last section motivates a simple picture for the 'microscopic' origin of this force. Our aim is not to calculate the various parameters of the IBM-2 Hamiltonian, but to give a qualitative understanding of the origin of this effective force.

As already mentioned in the latter section the GQR contributes strongly to the transition densities shown in Fig. 5.2. This surprising feature is examined in detail in this section. First, Fig. 5.8 delivers a proof for the admixture of the GQR in the wave function and sheds light on the consequences for the absolute $B(E2)$ values. Subfigures (I) and (II) display a decomposition of the $B(E2)$ values of the FSS and MSS in the contributions of the various proton two-quasiparticle components. Starting at the lowest two-quasiparticle configuration the contribution of each is summed up. The full $B(E2)$ values are reached at ~ 23 MeV. Two-quasiparticle components at higher energies contribute negligibly. (The transition strengths of Tab. 5.3 differ from the values in Fig. 5.8, since here are shown the corresponding values for the one-phonon states, *i.e.* the coupling to multi-phonon states is neglected.) The $B(E2)$ values are essentially composed from two sources, the valence space part which is located at low energies and a higher lying part located between 17 - 23 MeV. This higher lying part is formed by $2\hbar\omega$ two-quasiparticle states and belongs to the GQR [Pon10]. The admixture of the GQR exceeds $\sim 80\%$ of the $B(E2)$ value of the FSS and $\sim 65\%$ in case of the MSS, while its contributions to the wave functions is less than 2%. Hence, the dominating part of the collectivity (collectivity is used here in the sense of large $B(E2)$ values) arise from a coupling to the GQR making both states to one-phonon states (in the IBM-2 sense). For the $B(M1)$ value the situation is different. Here, the valence space is entirely responsible for the large $B(M1)$ value of $0.63 \mu_N^2$.

Due to the limited size of the model space, the GQR is not included in valence space approaches like the shell model and the IBM-2. These models can account for the $B(E2)$ strength stemming from the low-energy parts in Fig. 5.8. The parts of the high-energy mode are included effectively by using effective charges, which are typically fitted to the experimental $B(E2)$ strengths. On the contrary the QPM - covering a model space being large enough to fulfill the energy-weighted sum rules - can account for the valence part as well as the contribution of the GQR. As a consequence the QPM does not need any effective charges.

The presence of the GQR in the wave functions of quadrupole collective states raises the question about its *general role for effective forces used in nuclear structure models describing low-lying collective states such as the IBM-2*. This topic will be addressed qualitatively in the spirit of an effective field theory (EFT). EFTs are a concept of fundamental importance in physics with broad applications in many different areas such as Fermi theory and Chiral Perturbation theory in elementary particle physics [Wei79, Gas85], the BCS theory of superconductivity in solid states physics [Sha94] or in the construction of an effective nucleon-nucleon potential as a low-energy phenomenon of QCD in nuclear physics [Kol99]. The basic idea is to 'integrate out' the high energy sector and take its contributions approximately into account by a few parameters in the effective theory at lower energies. These parameters are usually determined from experiment. Therefore each EFT is only able to describe phenomenon at a specific and sufficiently low energy scale. This procedure can be formally carried out by the use of the renormalization group. The decoupling of physics at both energies is a necessary requirement, *i.e.* a clean separation of energy scales must be given.

The proton-neutron interaction is believed to be responsible for the development of configuration mixing, collectivity and finally for the formation of the FSS and MSS. In a phenomenological valence space approach like the IBM-2, which describes low-lying collective excitations, a simplified Hamiltonian can be written as:

$$\mathbf{H}_{IBM2} = \epsilon_\pi \mathbf{n}_{d\pi} + \epsilon_\mu \mathbf{n}_{d\mu} + 2\kappa \mathbf{Q}_\pi^{\chi\pi} \cdot \mathbf{Q}_\mu^{\chi\mu} \quad (5.3)$$

where ϵ_ρ and $\mathbf{n}_{d\rho}$ ($\rho = \pi$ or μ) are the d -boson energies and numbers. The crucial proton-neutron interaction is codified in the third term with $\mathbf{Q}_\rho^{\chi\rho}$ being boson quadrupole operators. An increase of the interaction strength κ will start to mix the unperturbed proton and neutron boson states and will finally cause the collective FSS and MSS connected by a strong $M1$ -transition as seen in experiment. This parameter is usually fixed empirically to experimental data without considering its microscopic origin which determines its strength.

To shed light on the 'microscopic' origin of this effective interaction we consider a different theoretical approach, namely the QPM. In the spirit of EFTs, the QPM can be viewed as the 'complete theory' including the 'high-lying' degrees of freedom. In contrast the IBM-2 is the effective theory valid at low-energies, where the correlations outside the IBM-2 model space are effectively taken into account.

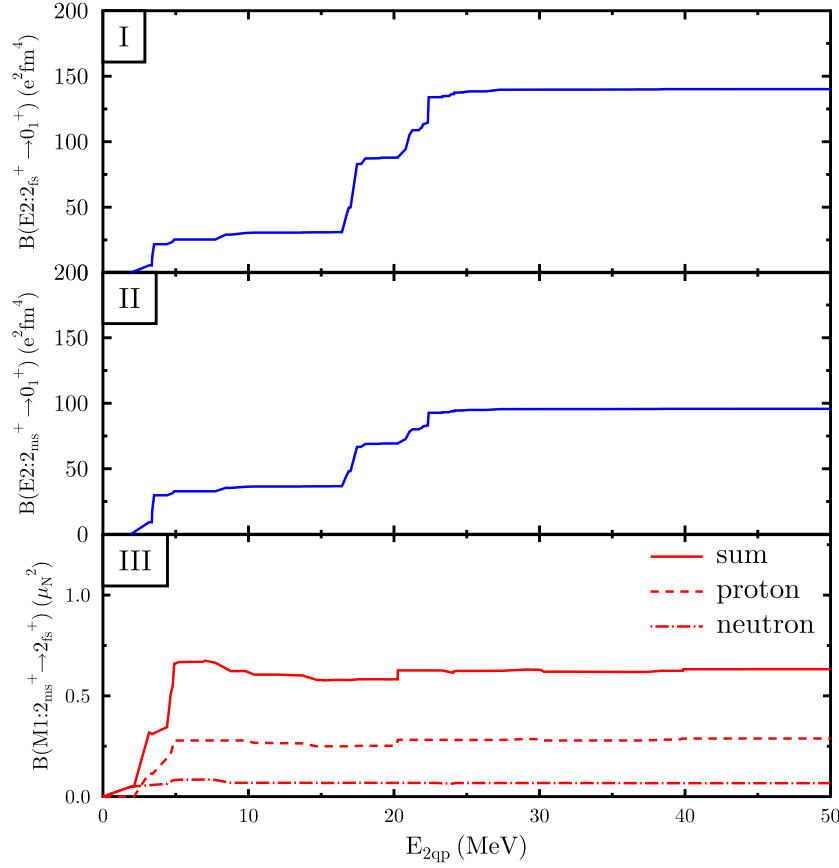


Figure 5.8: The decomposition of the absolute B(E2)- and B(M1)-values in the contributions of the various two-quasiparticle states. The B(E2)-values of the FSS (I) and MSS (II) are mainly formed by two-quasiparticle configurations in the energy range 17 - 23 MeV. This part of the wave function belongs to the GQR. In contrast the B(M1)-value is exclusively formed by the two large two-quasiparticle configurations $(2d_{5/2} \otimes 2d_{5/2})_n$ and $(1g_{9/2} \otimes 1g_{9/2})_p$ being low in energy.

In order to obtain a deeper understanding of the mechanism causing the formation of both states within a full space model like the QPM we introduce a simple '3-state model'. As a starting point we take the lowest proton and neutron two-quasiparticle BCS states at energies of 1.917 and 3.172 MeV respectively as in the full QPM calculation for ^{92}Zr and *in addition* the Giant Quadrupole Resonance (GQR) at 11.8 MeV. As in Landau-Migdal theory [Mig67] the interaction between the GQR and the two-quasiparticle states is given by a simple δ function:

$$\begin{aligned}
 V_\alpha &= g \cdot \langle \alpha | \delta(\vec{r} - \vec{r}') | GQR \rangle \\
 &= g \cdot \int dr \cdot r^2 \cdot \rho_\alpha(r) \cdot \rho_{GQR}(r)
 \end{aligned} \tag{5.4}$$

where α refers to the proton (p) or neutron (n) two-quasiparticle state. The parameter g is the interaction strength and ρ_α, ρ_{GQR} stand for the transition densities. The equation points to a direct relation between the collectivity of the GQR and the absolute value of the matrix element. Finally, the following Hamiltonian is diagonalized:

$$H_{3st} = \begin{pmatrix} GQR & -V_p & -V_n \\ -V_p & \epsilon_p & 0 \\ -V_n & 0 & \epsilon_n \end{pmatrix} \tag{5.5}$$

ϵ_{GQR} , ϵ_n and ϵ_p stand for the unperturbed energies. The results of this simple scheme are confronted with the full QRPA calculation in Table 5.6. The main properties *i.e.* formation of symmetric and mixed-symmetric states, neutron dominance of the FSS, B(E2)- and B(M1)-values are reproduced in this simple approach. The 3-state model accounts for the essential physics.

The crucial result is that the two collective states FSS and MSS are formed in the '3-state model' solely by a coupling to the GQR. The contribution of the GQR to the wave functions is small, but since the matrix element $\langle 0_1^+ || E2 || GQR \rangle$ is ~ 6 times larger than the one of the main proton two-quasiparticle state, the B(E2) value is mainly produced by the GQR as already discussed. This effect

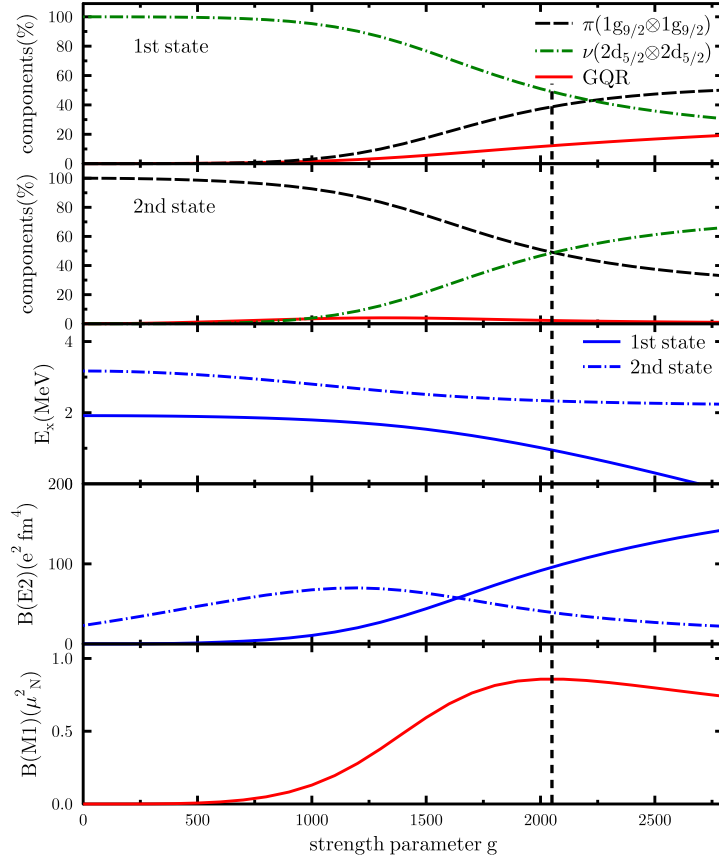


Figure 5.9: Shown are the results of the '3-state model' described in the text as a function of the coupling strength g . The dotted vertical line marks the coupling strength which describes the data most suitably.

observable	full QRPA		3-state		3-state QRPA	
	2_{fs}^+	2_{ms}^+	2_{fs}^+	2_{ms}^+	2_{fs}^+	2_{ms}^+
$(2d_{5/2} \otimes 2d_{5/2})_n$	71 %	28 %	50 %	50 %	76 %	22 %
$(1g_{9/2} \otimes 1g_{9/2})_p$	11 %	32 %	40%	50 %	24 %	74 %
$E(2_{fs}^+)$	1457 keV		1081 keV		1421 keV	
$E(2_{ms}^+)$	2536 keV		2485 keV		2498 keV	
$B(E2:2_{fs}^+ \rightarrow 0_1^+)$	166 e ² fm ⁴		181 e ² fm ⁴		259 e ² fm ⁴	
$B(E2:2_{ms}^+ \rightarrow 0_1^+)$	84 e ² fm ⁴		60 e ² fm ⁴		170 e ² fm ⁴	
$B(M1:2_{ms}^+ \rightarrow 2_1^+)$	0.63 μ_N^2		0.86 μ_N^2		0.87 μ_N^2	
ΔR_{charge}	0.07 fm		0.00 fm		-	
ΔR_{matter}	0.21 fm		0.22 fm		-	

Table 5.6: Comparison of wave functions (top) and selected observables calculated in the full QRPA to the 3-state model and the 3-state QRPA model discussed in the text for ^{92}Zr . The two simple models reproduce the essential features of the full QRPA calculation. The sign of the main neutron component of the MSS is in all three cases negative.

has been recognised previously by [Sag87]. The GQR not only brings the collectivity in the states but also causes a *mixing of the two dominant two-quasiparticle states*. In a valence-space approach like the IBM-2 this is achieved by the effective proton-neutron interaction codified in the third term of Eq.5.3. An enhancement of the interaction strength κ is equivalent to an increased coupling strength g to the GQR. The dependence of different observables on the coupling strength g is shown in Fig.5.9. In effective field theory language the proton-neutron quadrupole interaction in the IBM-2 can be thought of being dominantly mediated by the high energy mode GQR. Since the energy scale of low-lying collective structure is ~ 1 MeV and the isoscalar GQR is typically at ~ 10 MeV a clean separation of scales is given justifying this viewpoint.

Although the '3-state model' is successful in reproducing the main features of the full QRPA calculation, it cannot be expected to be valid at larger coupling strength g , since ground state correlations become important here. In order to include them, the QRPA equations have been solved, using the same ansatz as in the '3-state model', *i.e.* the GQR at higher energies and one proton and one neutron two-quasiparticle state. This model is labeled '3-state QRPA' in the following. The nuclei ^{92}Zr (Tab. 5.6), ^{94}Mo (Tab. 5.7) and ^{96}Mo (Tab. 5.8) are calculated within this approach and compared to full QRPA calculations. The unperturbed energy of the GQR in all three nuclei is the same at 11.8 MeV. The unperturbed two-quasiparticle energies - taken from a BCS calculation - are in ^{92}Zr $\epsilon_n = 1.917$ MeV and $\epsilon_p = 3.172$ MeV, in ^{94}Mo $\epsilon_n = 1.917$ MeV and $\epsilon_p = 2.698$ MeV and in ^{96}Mo $\epsilon_n = 2.194$ MeV and $\epsilon_p = 2.698$ MeV. The coupling strength to the GQR g was fixed to the value which describes the full QRPA results best. The coupling strength increases slightly from $g = 1082$ in ^{92}Zr to 1120 in ^{94}Mo and 1168 in ^{96}Mo . In all three nuclei the essential features of the

observable	full QRPA		3-state QRPA	
	2_{fs}^+	2_{ms}^+	2_{fs}^+	2_{ms}^+
$(2d_{5/2} \otimes 2d_{5/2})_n$	43 %	56 %	49 %	50 %
$(1g_{9/2} \otimes 1g_{9/2})_p$	39 %	36 %	48 %	49 %
$E(2_{fs}^+)$	938 keV		1099 keV	
$E(2_{ms}^+)$	2252 keV		2172 keV	
$B(E2:2_1^+ \rightarrow 0_1^+)$	407 e ² fm ⁴		483 e ² fm ⁴	
$B(E2:2_{ms}^+ \rightarrow 0_1^+)$	52 e ² fm ⁴		79 e ² fm ⁴	
$B(M1:2_{ms}^+ \rightarrow 2_1^+)$	$0.92\mu_N^2$		$1.27\mu_N^2$	

Table 5.7: Comparison of the full QRPA calculation to the 3-state QRPA model described in the text for ^{94}Mo . The simple model achieves a reasonable description of the QRPA results.

full QRPA calculation are well described. First, FSS and MSS phonons are formed with very similar amplitudes compared to the full QRPA results. Very interesting is the predicted proton dominance of the FSS and the neutron dominance of the MSS in ^{96}Mo . This is discussed in the next section. The energies of the symmetric and mixed-symmetric RPA-phonons are in reasonable agreement and especially the behaviour of the energy shifts when going from nuclei to nuclei are similar to the QRPA results. However, in ^{92}Zr both B(E2)-values are a factor ~ 2 larger than the full QRPA results.

observable	full QRPA		3-state QRPA	
	2_{fs}^+	2_{ms}^+	2_{fs}^+	2_{ms}^+
$(2d_{5/2} \otimes 2d_{5/2})_n$	31 %	67 %	34 %	65 %
$(1g_{9/2} \otimes 1g_{9/2})_p$	67 %	23 %	62 %	34 %
$E(2_{fs}^+)$	810 keV		1057 keV	
$E(2_{ms}^+)$	2426 keV		2326 keV	
$B(E2:2_1^+ \rightarrow 0_1^+)$	542 e ² fm ⁴		631 e ² fm ⁴	
$B(E2:2_{ms}^+ \rightarrow 0_1^+)$	23 e ² fm ⁴		35 e ² fm ⁴	
$B(M1:2_{ms}^+ \rightarrow 2_1^+)$	$0.67\mu_N^2$		$1.17\mu_N^2$	

Table 5.8: Comparison of the full QRPA calculation to the 3-state QRPA model described in the text for ^{96}Mo . Again, the simple model achieves a reasonable description of the QRPA results.

This discrepancy maybe attributed to the importance of other two-quasiparticle components in the wave functions, not included in the very small model space used here. Indeed, the wave function of the MSS in Tab. 5.2 exhibits contributions of $\sim 40\%$ from two-quasiparticle configurations, which are not included in the $(2d_{5/2} \otimes 2d_{5/2})_n$, $(1g_{9/2} \otimes 1g_{9/2})_p$ - modelspace. Therefore one cannot expect to describe these states correctly. In order to achieve better results of the '3-state QRPA' model, the model space must be enlarged to include the configurations known to be important in the wave functions of Tab. 5.2. These refinements of the '3-state QRPA' model are currently on their way. Surprisingly, the '3-state model' - which uses the same small model space - exhibits better agreement with the QRPA results. This behaviour is not understood and is probably accidental. For ^{94}Mo and ^{96}Mo the description of the B(E2) values is much better and close to the full QRPA results. This is remarkable for such a simple model approach. Indeed, here the contribution of the $(2d_{5/2} \otimes 2d_{5/2})_n$ - and $(1g_{9/2} \otimes 1g_{9/2})_p$ - configurations is larger than in ^{92}Zr . Very interesting is the behaviour of the '3-state QRPA' model at low coupling strength g (see Fig. 5.10). The B(E2) value of the MSS is larger than the one of the FSS. This matches the situation in ^{94}Zr where the B(E2)-value of the MSS is indeed a factor ~ 2 larger than the one of the FSS. It is very promising that such an uncommon feature is describable in this simple approach.

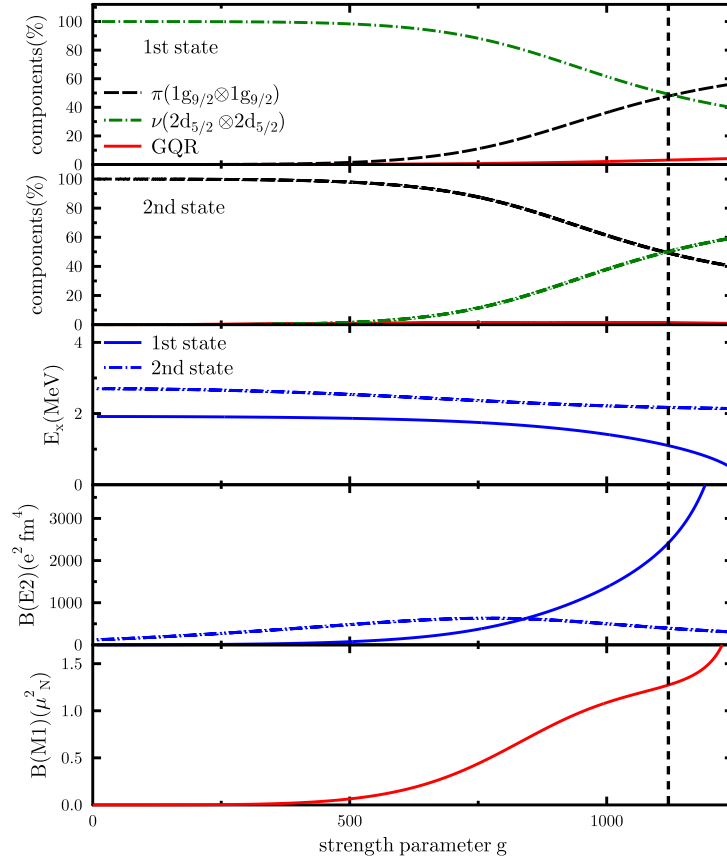


Figure 5.10: Shown are the results of the '3-state QRPA' model mentioned in the text as a function of the coupling strength g for ^{94}Mo . The dotted vertical line marks the coupling strength which describes the full QRPA results at best.

5.4 The evolution of one-phonon quadrupole mixed-symmetry states

The '3-state QRPA' model allows a simple explanation for the evolution of the MSS in ^{92}Zr , ^{94}Mo and ^{96}Mo . The experimental $B(\text{M}1)$ value increases from $0.37(4) \mu_N^2$ in ^{92}Zr [Fra05] to $0.56(5) \mu_N^2$ in ^{94}Mo [Fra03] and finally decreases to $0.17(2) \mu_N^2$ in ^{96}Mo [Les07]. What is the mechanism behind these sharp changes in the $B(\text{M}1)$ strengths? The behaviour is surprising, because the MSS are expected to be collective excitations and typically one assumes a very smooth change of the properties of collective states when going through the nuclear chart. However, in Fig. 5.8 it was shown that the $B(\text{M}1)$ strength is mainly determined by the two main two-quasiparticle components and hence has a single-particle nature. Clearly, changes in the $B(\text{M}1)$ strength must be guided by an interplay between these two main components.

The full QRPA calculation as well as the '3-state QRPA' model reproduce the variation in the $B(\text{M}1)$ values qualitatively (see Tabs. [6-8]), although both overpredict the experimental $B(\text{M}1)$ value. The $B(\text{M}1)$ strength has its largest value when the main proton and neutron amplitudes are balanced and as large as possible in the MSS and FSS states. So the wavefunctions for this 'optimal case' would be

$$\begin{aligned}
 |2_{\text{FSS}}^+\rangle &= 1/\sqrt{2} \left((1g_{9/2} \otimes 1g_{9/2})_p + (2d_{5/2} \otimes 2d_{5/2})_n \right) \\
 |2_{\text{MSS}}^+\rangle &= 1/\sqrt{2} \left((1g_{9/2} \otimes 1g_{9/2})_p - (2d_{5/2} \otimes 2d_{5/2})_n \right).
 \end{aligned}
 \tag{5.6}$$

Apparently, the wave functions of ^{94}Mo are closest to this case explaining its large $B(\text{M}1)$ value. In ^{92}Zr and ^{96}Mo either the neutron or proton two-quasiparticle component dominates the wave function of the 2_{FS}^+ . This unbalance reduces the $B(\text{M}1)$ value in comparison to ^{94}Mo . The '3-state QRPA' model offers a simple explanation for this behaviour. Figure 5.11 displays the contribution of the proton and neutron configurations to the wave functions of the FSS and MSS as functions of the *difference of the two-quasiparticle energies* $\Delta E = E_{2qp}((2d_{5/2} \otimes 2d_{5/2})_n) - E_{2qp}((1g_{9/2} \otimes 1g_{9/2})_p)$. The value $g = 1120$ obtained for ^{94}Mo was used as coupling strength.

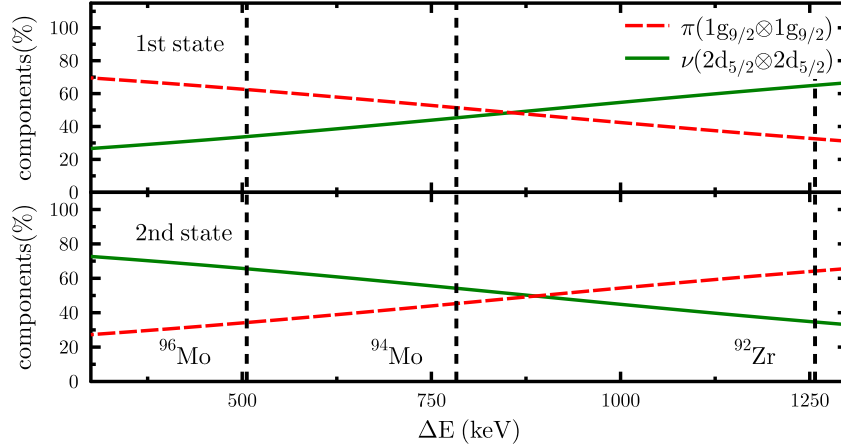


Figure 5.11: The two main components calculated in the '3-state QRPA' model as a function of the energy difference of the neutron and proton two-quasiparticle energy. The proton two-quasiparticle energy has been fixed to the value in the Mo chain at 2698 keV. The coupling strength is kept constant to the value of $g=1120$.

At a large energy difference the proton-neutron interaction mediated by the GQR is not strong enough to fully mix both states, hence the FSS is neutron and the MSS is proton dominated. Consequently the $B(M1)$ value is relatively small. This changes when the energy difference decreases. The proton-neutron interaction (which is kept constant here) is now strong enough to mix the two unperturbed states almost completely and at ~ 900 keV the optimal case of Eq. 5.6 is reached (of course, the GQR also contributes to the wavefunctions, but its amplitude is always smaller than 4%). If ΔE continues to decrease the effect of avoided level crossing takes place and the FSS becomes proton and the MSS neutron dominated. Due to the unbalance in the proton and neutron components the $B(M1)$ -value decreases again.

The vertical lines mark the energy differences ΔE in ^{92}Zr , ^{94}Mo and ^{96}Mo . The slightly different values of g which were used in the calculations of Tabs. 6-8 have only minor effects on the amplitudes, *e.g.* changing the value of g from 1120 to 1168 changes the amplitudes by less than 4%. Therefore Fig. 5.11 offers a qualitative understanding of the different $B(M1)$ strengths in the three nuclei. Due to the proton subshell at $Z=40$ the proton two-quasiparticle configuration is high in energy causing a large energy difference ΔE in ^{92}Zr . Consequently the $B(M1)$ value is small. The neutron dominance of the FSS is experimentally confirmed by the negative g -factor of $-0.18(1)$ as well as the proton dominance of the MSS with a positive g factor of $0.76(50)$. The energy difference in ^{94}Mo has nearly the optimal value resulting in a large $B(M1)$ strength. The increased importance of the proton two-quasiparticle configuration in the FSS is in agreement with the much larger g -factor of $0.274(75)$. Unfortunately no g factor of the MSS in ^{94}Mo is known. The nucleus ^{96}Mo is already beyond the optimal mixing point and the FSS is strongly proton dominated here, while the MSS is predicted to be neutron dominated. This decreases the $B(M1)$ -value again. Indeed, the experimental g factor of the FSS increases to $0.419(38)$ proving the increased importance of the proton configuration. Table 5.9 summarizes the g factor results. It would be of utmost importance to obtain information about the g factor of the MSS in ^{96}Mo which is not known so far to really check its neutron dominance. This could be done at the 'Rutgers/Yale g factor setup' at the university of Yale.

	$g(2_1^+)(\mu_N)$		$g(2_2^+)(\mu_N)$		$B(M1)(\mu_N^2)$	
	Exp	full QRPA	Exp	full QRPA	Exp	full QRPA
^{92}Zr	-0.18(1)	-0.09	0.76(50)	0.31	0.37(4)	0.64
^{94}Mo	0.274(75)	-	-	-	0.56(5)	0.92
^{96}Mo	0.419(38)	-	-	-	0.17(2)	0.67

Table 5.9: Comparison of calculated and measured g factors and $B(M1:2_{\text{ms}}^+ \rightarrow 2_1^+)$ strengths in ^{92}Zr , ^{94}Mo and ^{96}Mo .

Starting at the beginning of an isotopic chain, the increase of the neutron two-quasiparticle state from nucleus to nucleus (caused by an increase of the neutron pairing gap) coming closer to the lowest proton two-quasiparticle state seems to be a very common feature not limited to the Mo-chain. Hence, the simple picture of avoided level crossing seems to be a very general feature of MSSs and points to a 'washing out' of MSSs and a decrease of the corresponding $B(M1)$ strength when approaching more collective nuclei. In the Cd-chain a decrease of the $B(M1)$ -strength is also predicted in a large-scale shell-model calculation [Boe07]. However, experimental data is still missing at the beginning of the chain. At midshell in ^{112}Cd and ^{114}Cd experimental data is available and the $B(M1)$ strength amounts to $0.099(7)\mu_N^2$ and $0.089(9)\mu_N^2$, respectively. These are much smaller values than observed in the $N=52$ chain. If one accepts that the $B(M1)$ value of ^{102}Cd has a similar magnitude as in ^{92}Zr , ^{94}Mo and ^{96}Ru , the decrease of the

B(M1) strength is also present in the Cd-chain. Very interestingly, the proton and neutron amplitudes of the MSS in ^{112}Cd has been extracted from inelastic hadron scattering by Pignanelli *et al.* [Pig88]. The neutron amplitude dominates which is in agreement with the expectations from the avoided level crossing.

Of course, the picture of the avoided level crossing is only meaningful when the $(1g_{9/2} \otimes 1g_{9/2})_p$ - and $(2d_{5/2} \otimes 2d_{5/2})_n$ - configurations are dominating in the wavefunctions. This is the case for ^{94}Mo , ^{96}Mo and partly for ^{92}Zr , but for more collective nuclei like ^{98}Mo other two-quasiparticle states should play an important role. Hence, one better takes the avoided level crossing as the 'driving force' behind the decrease of the B(M1) strength in the N=50 region, but there might be other effects which also play an important role.

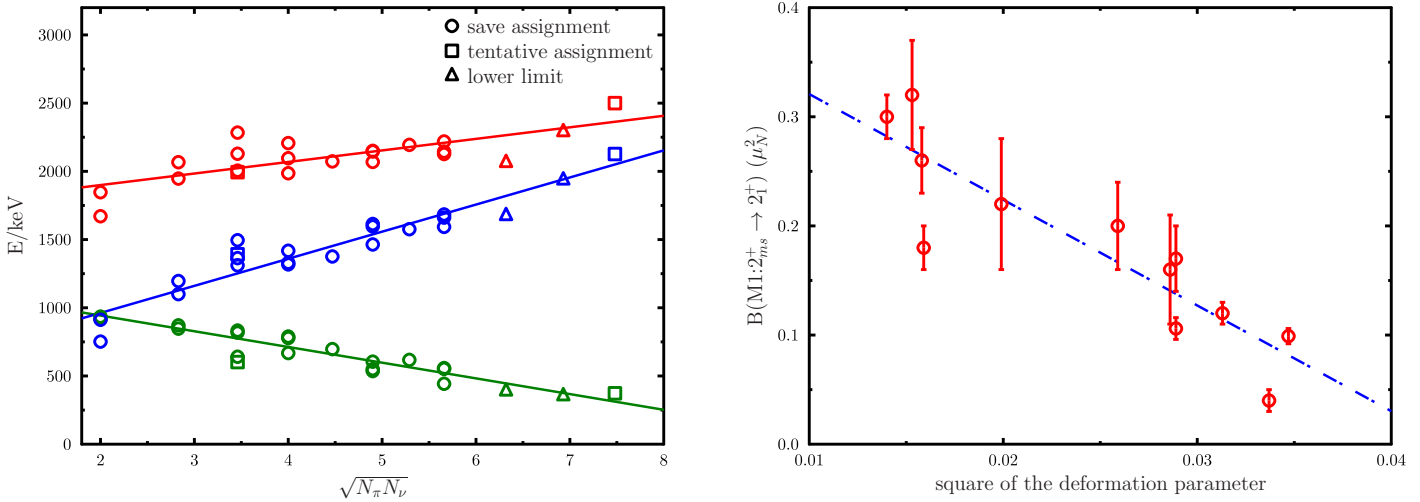


Figure 5.12: The excitation energies of the FSS (green), MSS (red) and their energy difference (blue) over $\sqrt{N_\pi N_\nu}$ (lhs). N_π and N_ν are the valence proton and neutron numbers counted to the nearest closed shell. On the right hand side is shown the dependence of the B(M1)-value on the square of the deformation parameter. The dashed blue line is drawn to guide the eyes.

A very common case in nuclear structure physics is the fragmentation of a specific state (*e.g.* the scissors mode). In experiment one possibly observes only one fragment and misses another. This would also 'decrease' the observed transition strength. However, it is worth mentioning that ^{94}Mo , ^{96}Mo , ^{92}Zr as well as ^{112}Cd and ^{114}Cd are measured using the $(n, n'\gamma)$ -reaction. This method gives rather complete information about the M1-transitions to the FSS up to ~ 3.5 MeV. Hence, the decrease of the B(M1)-strength in ^{96}Mo , ^{112}Cd and ^{114}Cd is really a nuclear structure effect and can not be attributed to fragmentation.

The simple picture of the avoided level crossing in the '3-state QRPA' model is confirmed by the full QRPA calculation (so even when the '3-state QRPA' model is not valid, the avoided level crossing is still a feature of the full QRPA calculation). It would be very useful to have a shell-model calculation - the superior model for these low-lying states - for the nuclei in the N=50 region to confirm this picture. Unfortunately, in the shell-model calculation of the Cd-chain [Boe07] no information about the wavefunctions is given. It would be very helpful to redo these calculations (maybe in a J-scheme code) in order to analyse them. These efforts are justified, since the question if the MSS is 'washed out' when approaching more collective nuclei is of course at the heart of MSS investigations. It is also in strong contrast to the IBM-2 which predicts a nearly constant B(M1) value (at least in the three analytically solvable limits). Probably, the assumption of equal proton and neutron boson energies is a problem. Then one always obtains perfect mixing of the proton and neutron components.

It is not clear yet if the effect of avoided level crossing can really be applied to explain the behaviour of the MSS in other regions of the nuclear chart. But a decrease of the M1 strength has been also observed in the Xe chain in Ref. [Coq10]. Unfortunately these measurements were done using the method of Coulomb excitation which does not allow to detect all 2^+ states up to ~ 3 MeV. Hence, one can not be sure if one misses fragments at higher energies.

The sensitivity of MSS to the two-quasiparticle energies offers the possibility to fit pairing matrix-elements used in the shell-model to the properties of MSS. This was recognized in Ref. [Sie09] where the pairing matrix elements were fine-tuned using the properties of MSS. Hence, MSS can be expected to improve the development of effective interactions in the future.

Finally, Fig. 5.12 displays some systematics of the properties of MSS and FSS. On the left-hand side is shown the energy of the 2^+_{fs} (green line), the energy of the 2^+_{ms} (red line) and their energy difference (blue line) in dependence of the square root of the valence proton times the valence neutron numbers (taking care of subshells). This is motivated by the results of Ref. [Hey86], which argues that the properties of MSS depend on this quantity. All MSS of Tab. 5.10 are included. The smooth dependence on this quantity is surprising and not understood. On the right-hand side is shown the B(M1) strength in dependence on the square of the deformation parameter. Again all MSS of Tab. 5.10 are included except for the MSS in the Mo, Ru and Zr chains. Their properties are maybe

different due to the subshell closure. One finds a linear behaviour on the deformation parameter which is not understood and in contrast to the findings for the scissors mode [Hey10]. Another interesting feature of MSS - not shown here - is the simultaneous decrease of the $B(M1)$ and $B(E2)$ values of the MSS. This is also predicted by the '3-state QRPA' model and is probably connected to the predicted neutron dominance.

$\sqrt{N_{\pi}N_{\nu}}$	Nucleus	$E(2_1^+)$ (keV)	$E(2_{ms}^+)$ (keV)	$E(2_{ms}^+) - E(2_1^+)$ (keV)	$B(M1:2_{ms}^+ \rightarrow 2_1^+)$ (μ_N^2)	$B(E2:2_1^+ \rightarrow 0_1^+)$ (W.u.)	$B(E2:2_{ms}^+ \rightarrow 0_1^+)$ (W.u.)
2	^{92}Zr	935	1847	912	0.37(4)	6.4(6)	3.4(4)
2	^{94}Zr	919	1671	752	0.31(3)	4.9(3)	7.8(7)
2.83	^{94}Mo	871	2067	1196	0.56(5)	16(1)	1.8(2)
2.83	^{134}Xe	847	1947	1100	0.30(2)	15.3(11)	0.72(7)
3.46	^{96}Ru	833	2284	1495	0.78(23)	18.1(5)	1.6(3)
3.46	^{136}Ba	818	2129	1311	0.26(3)	19.21(14)	2.1(2)
3.46	^{140}Ba	602	1994	1392	-	17.14(509)	-
4	^{96}Mo	778	2096	1330	0.17(3)	20.7(3)	0.08(2)
4	^{138}Ce	789	2207	1418	0.18(2)	21.2(14)	2.43(16)
4	^{132}Xe	668	1986	1318	0.22(6)	23.0(15)	0.67(18)
4.47	^{144}Nd	697	2073	1376	0.14(3)	24.53(134)	1.7(4)
4.90	^{148}Sm	550	2146	1596	0.147(45)	30.9(13)	0.68(18)
4.90	^{134}Ba	605	2069	1464	0.20(4)	33.39(58)	2.0(2)
4.90	^{130}Xe	536	2150	1614	0.16(5)	33.2(26)	0.25(7)
5.29	^{112}Cd	618	2194	1576	0.099(7)	30.2(3)	-
5.66	^{128}Xe	443	2127	1684	0.04(1)	42.6(64)	0.21(7)
5.66	^{136}Ce	552	2145	1593	0.17(3)	39(4)	0.52(3)
5.66	^{114}Cd	558	2219	1661	0.089(9)	31.07(182)	0.107(17)
6.32	^{126}Xe	389	>2064	>1675	-	41.0(13)	-
6.93	^{124}Xe	354	>2300	>1946	-	57.7(15)	-
7.48	^{110}Pd	373	~2500	2127	-	57.49(383)	-

Table 5.10: Summary of experimental properties of mixed-symmetry states [Pie08, Coq10]

6 Summary and outlook

This work contains one main results. A new signature was found for identifying the quadrupole one-phonon mixed-symmetry state (MSS) independently of M1 transition matrix elements. The new signature is based on a strong reduction of the matter transition radius of the MSS compared to other 2^+ states. This reduction is directly connected to its isovector nature. Proton scattering data have been analysed to obtain experimental informations about this quantity. Using the new method the quadrupole MSS in ^{92}Zr and ^{94}Mo have been unambiguously identified.

In addition the new signature allows to measure for the first time the relative signs between the two main proton and neutron two-quasiparticle components and the GQR. To obtain this experimental observable it was necessary to measure - besides the matter transition radii - the difference of the charge transition radii of the fully-symmetric state (FSS) and MSS. This was done using electron scattering data measured at S-DALINAC and evaluated in the framework of this thesis. The results show that in ^{92}Zr and ^{94}Mo the main neutron components is out-of-phase to the GQR, while the main proton component is in-phase. It is remarkable that such a quantity can really be measured, since other observables like the B(M1) strength are insensitive to this quantity. It would be interesting to investigate a nucleus where the main proton component can be expected to be out-of-phase to the GQR and the main neutron components in-phase. This would cause an enlarged matter transition radius of the MSS and a difference in the charge transition radii, *i.e.* the situation is the opposite compared to ^{92}Zr and ^{94}Mo . Promising candidates can be found in the Zn-chain.

Finally, the experimental results obtained from proton and electron scattering prove that the FSS and MSS are formed by three main building blocs: The GQR, a large proton and a large neutron two-quasiparticle component. This observation motivates a simple picture on the microscopic origin of the effective proton-neutron interaction used in quadrupole collective models like the IBM-2 - a question which has not been answered so far. From an effective field theory viewpoint the GQR can be believed to mediate this force by coupling to the valence-space components. A simple '3-state model' using this idea gives surprisingly good agreement with full QRPA calculations. However, the validity of this idea must be further tested. The next obvious step is to enlarge the model space and to include more than just two two-quasiparticle components in the valence space. These refinements are currently under way. The newly developed 'three state model' predicts the properties of FSS and MSS in the N=50 region to depend crucially on the energy difference of the lowest proton and the lowest neutron two-quasiparticle state. This results in a neutron dominance of the MSS when going from ^{94}Mo to ^{96}Mo which is in agreement with the predictions of the full QRPA calculations. It would be of utmost importance to verify these predictions experimentally and to measure the g-factors of the MSS in ^{94}Mo and ^{96}Mo (at least the sign). This could be done *e.g.* with the 'Rutgers/Yale g-factor setup' at the university of Yale.

An other interesting feature of MSS observed in this thesis is the deformation dependence of the B(M1) strength. The B(M1) strength decreases linearly with increasing square of the deformation parameter. The behaviour is opposite to the scissors mode where B(M1) strength increases linearly with increasing square of the deformation parameter. The underlying reason is not understood yet.

References

- [Ari75] A. Arima and F. Iachello, *Phys. Rev. Lett.* 35, 1069 (1975).
- [Ari77] A. Arima, T. Otsuka, F. Iachello and I. Talmi, *Phys. Lett. B* 66, 205 (1977).
- [Ari78] A. Arima and F. Iachello, *Phys. Rev. Lett.* 40, 385 (1978).
- [Bak75] F. T. Baker, A. Scott, M. A. Grimm, W. G. Love, V. Penumetcha, C. Glashauser, G.S. Adams, G. Igo, G. W. Hoffmann, J. M. Moss, W. Swenson and B. E. Wood, *Nucl. Phys. A* 393, 283 (1983).
- [Bähr] C. Bähr, code PHASHI, TU Darmstadt, unpublished
- [Ber99] C. A. Bertulani and V. Yu. Ponomarev, *Phys. Rep.* 321, 139 (1999).
- [Bog03] S. K. Bogner, T. T. S. Kuo and A. Schwenk, *Phys. Rep.* 386, 1 (2003).
- [Boh75] A. Bohr and B. Mottelson, *Nuclear Structure II*, Benjamin Reading (1975).
- [Boh84] D. Bohle, A. Richter, W. Steffen, A. E. L. Dieperink, N. Lo Iudice, F. Palumbo and O. Scholten, *Phys. Lett. B* 137, 27 (1984).
- [Boe07] N. Boelaert, N. Smirnova, K. Heyde and J. Jolie, *Phys. Rev. C* 75, 014316 (2007).
- [Bre85] P. von Brentano, A. Gelberg, H. Harter and P. Sala, *J. Phys. G: Nucl. Phys.* 11, (1985) L85?L89.
- [Bur75] S. J. Burger and G. Heymann, *Nucl. Phys. A* 243, 461 (1975).
- [Bur07] O. Burda, N. Botha, J. Carter, R. W. Fearick, S. V. Förtsch, C. Fransen, H. Fujita, J. D. Holt, M. Kuhar, A. Lenhardt, P. von Neumann-Cosel, R. Neveling, N. Pietralla, V. Yu. Ponomarev, A. Richter, O. Scholten, E. Sideras-Haddad, F. D. Smit and J. Wambach, *Phys. Rev. Lett.* 99, 092503 (2007).
- [Cas85] R. F. Casten, *Phys. Rev. Lett.* 54, 1991 (1985).
- [Cas87] R. F. Casten, D. S. Brenner and P. E. Haustein, *Phys. Rev. Lett.* 58, 658 (1987).
- [Coq10] L. Coquard, N. Pietralla, G. Rainovski, T. Ahn, L. Bettermann, M.P. Carpenter, R.V.F. Janssens, J. Leske, C.J. Lister, O. Möller, W. Rother, V. Werner and S. Zhu, *Phys. Rev. C* 82, 024317 (2010).
- [Day67] B. D. Day *Rev. Mod. Phys.* 39, 719 (1967).
- [Epl09] E. Epelbaum, H.-W. Hammer and Ulf-G. Meißner, *Rev. Mod. Phys.* 81, 1773 (2009).
- [Faz92] B. Fazekas, T. Belgya, G. Molnar, R. A. Gatenby, S. W. Yates and T. Otsuka, *Nucl. Phys. A* 548, 249 (1992).
- [Fed78] P. Federman and S. Pittel, *Phys. Lett. B* 77, 29 (1978).
- [Fel98] H. Feldmeier, T. Neff, R. Roth and J. Schnack, *Nucl. Phys. A* 632, 61 (1998).
- [Fra85] M. A. Franey and W. G. Love, *Phys. Rev. C* 31, 488 (1985).
- [Fra03] C. Fransen, N. Pietralla, Z. Ammar, D. Bandyopadhyay, N. Boukharouba, P. von Brentano, A. Dewald, J. Gableske, A. Gade, J. Jolie, U. Kneissl, S. R. Leshner, A. F. Lisetskiy, M. T. McEllistrem, M. Merrick, H. H. Pitz, N. Warr, V. Werner and S. W. Yates, *Phys. Rev. C* 67, 024307 (2003).
- [Fra05] C. Fransen, V. Werner, D. Bandyopadhyay, N. Boukharouba, S. R. Leshner, M. T. McEllistrem, J. Jolie, N. Pietralla, P. von Brentano and S. W. Yates, *Phys. Rev. C* 71, 054304 (2005).
- [Fuji] H. Fujita Computer program SFit, unpublished.
- [Gar96] P. E. Garrett, H. Lehmann, C. A. McGrath, Minfang Yeh and S. W. Yates, *Phys. Rev. C* 54, 2259 (1996).

-
- [Gas85] J. Gasser and H. Leutwyler, Nucl. Phys. B 250, 465 (1985).
- [Gue99] D. Guéry-Odelin and S. Stringari, Phys. Rev. Lett. 83, 4452 (1999).
- [Ham84] W. D. Hamilton, A. Irbäck and J. P. Elliott, Phys. Rev. Lett. 53, 2469 (1984).
- [Hey86] K. Heyde and J. Sau, Phys. Rev. C 33, 1050 (1986).
- [Hei83] J. Heisenberg and H. P. Blok, Annual Review of Nuclear and Particle Science 33, 569 (1983).
- [Hey10] K. Heyde and P. von Neumann-Cosel and A. Richter, arXiv.org:1004.3429 (2010).
- [Iac84] F. Iachello, Phys. Rev. Lett. 53, 1427 (1984).
- [Iac87] F. Iachello and A. Arima, Cambridge University Press, Cambridge (1987).
- [Iac98] F. Iachello, N. V. Zamfir and R. F. Casten, Phys. Rev. Lett. 81, 1191 (1998).
- [Iac00] F. Iachello, Phys. Rev. Lett. 85, 3580 (2000).
- [Iac06] F. Iachello, Phys. Rev. C 73, 037305 (2006).
- [Iud02] N. Lo Iudice and Ch. Stoyanov, Phys. Rev. C 65, 064304 (2002).
- [Iud08] N. Lo Iudice, Ch. Stoyanov and D. Tarpanov, Phys. Rev. C 77, 044310 (2008).
- [Jak99] G. Jakob, N. Benczer-Koller, J. Holden, G. Kumbartzki, T. J. Mertzimekis, K. -H. Speidel, C. W. Beausang and R. Kruecken, Phys. Lett. B 468, 13 (1999).
- [Jag74] C. W. Jager, H. de Vries and C. de Vries, At. Data Nucl. Data Tables 14, 479 (1974).
- [Kim96] K. Kim, A. Gelberg, T. Mizusaki, T. Otsuka and P. von Brentano, Nucl. Phys. A 604, 163 (1996).
- [Knu76] W. Knüpfner and M. G. Huber, Phys. Rev. C 14, 2254 (1976).
- [Kol99] U. Van Kolck, Progr. Part. Nucl. Phys. 43, 337 (1999).
- [Kow04] K. Kowalski, D. J. Dean, M. Hjorth-Jensen, T. Papenbrock and P. Piecuch, Phys. Rev. Lett. 92, 132501 (2004).
- [Kuh05] M. Kuhar, Diplomarbeit, TU Darmstadt (2005).
- [Kunz] P. D. Kunz, computer code CHUCK3 (unpublished).
- [Len06] A. W. Lenhardt, U. Bonnes, O. Burda, P. von Neumann-Cosel, M. Platz, A. Richter and S. Watzlawik, Nucl. Instrum. Meth. A 562, 320 (2006).
- [Les07] S. R. Leshner, C. J. McKay, M. Mynk, D. Bandyopadhyay, N. Boukharouba, C. Fransen, J. N. Orce, M. T. McEllistrem and S. W. Yates, Phys. Rev. C 75, 034318 (2007).
- [Leu94] H. Leutwyler, Annals Phys. 235, 165 (1994).
- [Lie88] K. P. Lieb, H. G. Börner, M. S. Dewey, J. Jolie, S. J. Robinson, S. Ulbig and Ch. Winter, Physics Letters B 215, 50 (1988).
- [Lis00] A. F. Lisetskiy, N. Pietralla, C. Fransen, R. V. Jolos and P. von Brentano, Nucl. Phys. A 677, 100 (2000).
- [Lüt95] C. Lüttge, C. Hofmann, J. Horn, F. Neumeyer, A. Richter, G. Schrieder, E. Spamer, A. Stiller, D. I. Sober, S. K. Matthews and L. W. Fagg, Nucl. Instr. Meth. A 366, 325 (1995).
- [Mac01] R. Machleidt, Phys. Rev. C 63, 024001 (2001).
- [Mar00] O. M. Maragò, S. A. Hopkins, J. Arlt, E. Hodby, G. Hechenblaikner and C. J. Foot, Phys. Rev. Lett. 84, 2056 (2000).
- [Mig67] A. B. Migdal, Interscience Publishers (1967).
- [Moh99] P. Mohr, J. Enders, T. Hartmann, H. Kaiser, D. Schiesser, S. Schmitt, S. Volz, F. Wissel and A. Zilges, Phys. Rev. Lett. 423, 480 (1999).

-
- [Muk08] S. Mukhopadhyay, M. Scheck, B. Crider, S. N. Choudry, E. Elhami, E. Peters, M. T. McEllistrem, J. N. Orce, and S. W. Yates, *Phys. Rev. C* 78, 034317 (2008).
- [Nav03] P. Navrátil and W. Erich, *Phys. Rev. C* 68, 034305 (2003).
- [Nef03] T. Neff and H. Feldmeier, *Nucl. Phys. A* 713, 311 (2003).
- [New96] R. T. Newman, Single proton transfer on ^{55}Mn , Doctoral thesis, University of Cape Town (1996).
- [Nes99] V. O. Nesterenko, W. Kleinig, F. F. de Souza Cruz and N. Lo Iudice, *Phys. Rev. Lett.* 83, 57 (1999).
- [NuP04] NuPECC Long Range Plan, (2004).
- [Ots78] T. Otsuka, A. Arima and F. Iachello, *Nucl. Phys. A* 309, 1 (1978).
- [Ots01] T. Otsuka, R. Fujimoto, Y. Utsuno, B. A. Brown, M. Honma and T. Mizusaki, *Phys. Rev. Lett.* 87, 082502 (2001).
- [Pie03] S. C. Pieper, *Nucl. Phys. A* 751, 516 (2003).
- [Pie94] N. Pietralla, P. von Brentano, R. F. Casten, T. Otsuka and N. V. Zamfir, *Phys. Rev. Lett.* 73, 2962 (1994).
- [Pie98a] N. Pietralla, D. Belic, P. von Brentano, C. Fransen, R.-D. Herzberg, U. Kneissl, H. Maser, P. Matschinsky, A. Nord, T. Otsuka, H. H. Pitz, V. Werner and I. Wiedenhöver, *Phys. Rev. C* 58, 796 (1998).
- [Pie98b] N. Pietralla, T. Mizusaki, P. von Brentano, R. V. Jolos, T. Otsuka and V. Werner, *Phys. Rev. C* 57, 150 (1998).
- [Pie99] N. Pietralla, C. Fransen, D. Belic, P. von Brentano, C. Frießner, U. Kneissl, A. Linnemann, A. Nord, H. H. Pitz, T. Otsuka, I. Schneider, V. Werner and I. Wiedenhöver, *Phys. Rev. Lett.* 83, 1303 (1999).
- [Pie20] N. Pietralla, C. Fransen, P. von Brentano, A. Dewald, A. Fitzler, C. Frießner and J. Gableske, *Phys. Rev. Lett.* 84, 3775 (2000).
- [Pie08] N. Pietralla, P. von Brentano and A.F. Lisetskiy, *Prog. Part. Nucl. Phys.* 60, 225 (2008).
- [Pig88] M. Pignanelli, S. Micheletti, N. Blasi, R. De Leo, W. T. A. Borghols, J. M. Schippers, S. Y. Van Der Werf and M. N. Harakeh, *Phys. Lett. B* 202, 470 (1988).
- [Pig92] M. Pignanelli, N. Blasi, S. Micheletti and *et al.* *Nucl. Phys. A* 540, 27 (1992).
- [Pon99] V. Yu. Ponomarev and P. von Neumann-Cosel, *Phys. Rev. Lett.* 82, 501 (1999).
- [Pon10] V. Ponomarev, private communication (2010).
- [Ray07] J. Raynal, code DWBA07, NEA data bank NEA-1209 (2007).
- [Rot07] R. Roth, P. Navrátil, *Phys. Rev. Lett.* 99, 092501 (2007).
- [Sag87] H. Sagawa, O. Scholten, B. A. Brown and B. H. Wildenthal, *Nucl. Phys. A* 462, 1 (1987).
- [Sav10] D. Savran, K. Lindenberg, J. Glorius, B. Löher, S. Müller, N. Pietralla, L. Schnorrenberger, V. Simon, K. Sonnabend, C. W"lzlein, M. Elvers, J. Endres, J. Hasper and A. Zilges, *Nucl. Instr. Meth A* 613, 2 (2010).
- [Sch82] P. Schwandt, H. O. Meyer, W. W. Jacobs, A. D. Bacher, S. E. Vigdor, M. D. Kaitchuck and T. R. Donoghue, *Phys. Rev. C* 26, 55 (1982).
- [Sch10] M. Scheck, P. A. Butler, C. Fransen, V. Werner and S. W. Yates, *Phys. Rev. C* 81, 064305 (2010).
- [Sev08] A. P. Severyukhin, V. V. Voronov and N. Van Giai *Phys. Rev. C* 77, 024322 (2008).
- [Sha53] A. de-Shalit and M. Goldhaber, *Phys. Rev.* 92, 1211 (1953).
- [Sha94] R. Shankar, *Rev. Mod. Phys.* 66, 129 (1994).
- [Shu07] J. Suhonen, *From Nucleons to Nucleus: Concepts of Microscopic Nuclear Theory*, Springer Verlag, Berlin (2007).
- [Sie09] K. Sieja, G. Martínez-Pinedo, L. Coquard and N. Pietralla, *Phys. Rev. C* 80, 054311 (2009).

-
- [Sin09] P. Singh, D. Rychel, R. Gyufko, M. Lahanas and C. A. Wiedner, Nuclear Physics A 458, 1 (2009).
- [Sol92] V.G. Soloviev, Theory of Atomic Nuclei: Quasiparticles and Phonons, Institute of Physics Publishing, Bristol (1992)
- [Tal62] I. Talmi, Rev. Mod. Phys. 34, 704 (1962).
- [Tan85] I. Tanihata, H. Hamagaki, O. Hashimoto, Y. Shida, N. Yoshikawa, K. Sugimoto, O. Yamakawa, T. Kobayashi and N. Takahashi, Phys. Rev. Lett. 55, 2676 (1985).
- [Van95] J. R. Vanhoy, J. M. Anthony, B. M. Haas, B. H. Benedict, B. T. Meehan, S.F. Hicks, C. M. Davoren and C. L. Lundstedt, Phys. Rev. C 52, 2387 (1995).
- [Ver88] W. J. Vermeer, C. S. Lim and R. H. Spear, Phys. Rev. C 38, 2982 (1988).
- [Vet98] K. Vetter *et al.*, Phys. Rev. C 58, R2631 (1998).
- [Wal78] Th. Walcher, R. Frey, H.-D. Gräf, E. Spamer and H. Theissen, Nuclear Instruments and Methods 153, 17 (1978).
- [Wam10] J. Wambach, private communication (2010).
- [Wei79] S. Weinberg, Physica 96A, 327 (1979).
- [Wer08] V. Werner *et al.*, Phys. Rev. C 78, 031301 (2008).
- [Wie97] I. Wiedenhöver, A. Gelberg, T. Otsuka, N. Pietralla, J. Gableske, A. Dewald and P. von Brentano, Phys. Rev. C 56, R2354 (1997).
- [Wir98] R. B. Wiringa, V. G. J. Stoks and R. Schiavilla, Phys. Rev. C 51, 38 (1995).
- [Wou87] A. Van Der Woude, Progr. Part. Nucl. Phys. 18, 217 (1987).
- [Yev10] O. Yevetska, S. Watzlawik, J. Ahrens, G.D. Alkhazov, V.P. Chizhov, E.M. Maev, P. von Neumann-Cosel, E.M. Orischin, G.E. Petrov, J.-M. Porte, A. Richter, V.V. Sarantsev, G. Schrieder and Yu.V. Smirenin Nucl. Instr. Meth. A 618, 160 (2010).

Erklärung zum Project-Proposal

Hiermit versichere ich das vorliegende Project-Proposal ohne Hilfe Dritter nur mit den angegebenen Quellen und Hilfsmitteln angefertigt zu haben. Alle Stellen, die aus Quellen entnommen wurden, sind als solche kenntlich gemacht. Diese Arbeit hat in gleicher oder ähnlicher Form noch keiner Prüfungsbehörde vorgelegen.

Darmstadt, den 27.09.2010

(Christopher Walz)